The Dissertation Committee for Kaushik Comandoor Alayavalli
certifies that this is the approved version of the following dissertation:

DESIGN, FABRICATION AND TESTING OF GRAPHITE BIPOLAR PLATES FOR DIRECT METHANOL FUEL CELLS BY INDIRECT LASER SINTERING

Committee:

David L. Bourell, Supervisor

Arumugam Manthiram

Jeremy Meyers

Maria G. Juenger

Robert Moser

DESIGN, FABRICATION AND TESTING OF GRAPHITE BIPOLAR PLATES FOR DIRECT METHANOL FUEL CELLS BY INDIRECT LASER SINTERING

by

Kaushik Comandoor Alayavalli, B.E., M.S.

Dissertation

Presented to the Faculty of the Graduate School of

The University of Texas at Austin

in Partial Fulfillment

of the Requirements

for the Degree of

Doctor of Philosophy

The University of Texas at Austin

August 2011

Dedication

To my parents.

Acknowledgements

Through the course of this Ph.D., I have realized that I could never have done any of this, particularly the research and writing that went into this dissertation, without the support and encouragement of a lot of people.

First and foremost I would like to thank my advisor, Dr. David L. Bourell without whom none of this work would have been possible. I could not have hoped for a better advisor to support and guide me through this Ph.D. I would also like to express my gratitude to Dr. Arumugam Manthiram for providing me with the opportunity to learn and grow in this field. I thank Dr. Jeremy Meyers for all the input and suggestions that have helped in this research and Dr. Maria Juenger and Dr. Robert Moser for their invaluable comments and suggestions. I would like to thank Mark Phillips, Fred Rotthauser, Rosalie Foster and all the other staff members who, in the course of my research, have provided incredible assistance and spent hours helping me with my work.

I gratefully acknowledge the funding sources that made my Ph.D. work possible. My work was supported by the Office of Naval Research grant No. N00014-07-1-0758. I would like to express my thanks to everyone involved, particularly Dr. Khershed Cooper for all the comments and suggestions that have guided this work.

I would also like to express my thanks to my group mates, Arindam Sarkar, Kim Jung Hyun, Kumaran Chakravarthy, Abhishek Goel and Phani Vallabhajosyula for all the stimulating conversations. I sincerely thank Dr. Vadivel Murugan for being a great mentor, sounding board and for helping me develop as a researcher. This work would not have been possible without the moral support of my friends Kullamani, Praveen

Pasupathy, Arjun Seshadri and Aditya Sankaran who provided the necessary distractions to get through this period of my life.

Most of all, I would like to express my love and gratitude to my wife, Sulakshana, who has borne the brunt of the inevitable pressures and has provided unflinching support through it all.

Finally, I dedicate this work to my family whose undying love and support has helped me achieve everything in my life.

DESIGN, FABRICATION AND TESTING OF GRAPHITE BIPOLAR PLATES FOR DIRECT METHANOL FUEL CELLS BY INDIRECT LASER SINTERING

Kaushik Comandoor Alayavalli, Ph.D.
The University of Texas at Austin, 2011

Supervisor: David Bourell

Direct Methanol Fuel Cells (DMFCs) are electrochemical energy conversion devices that convert chemical energy into electrical energy. The bipolar plate component of the DMFC is required to be fluid impermeable to prevent fuel leakage and electrically conductive to collect the electrons produced within the cell. Graphite possesses the properties of high electrical conductivity, low weight and resistance to corrosion that make it an attractive material for bipolar plates. However, the poor mechanical properties of graphite lead to prohibitive machining costs and increased production times. The objective of this research is to develop an indirect laser sintering (LS) process, involving the laser sintering of graphite powders mixed with a phenolic resin binder which offers the advantage of complex part production and testing of prototype bipolar plates in short times. Due to the nature of the indirect LS process, the as-produced (green part) plates are porous and possess low electrical conductivities (< 0.1 S.cm^{-1}).

This research describes a viable method to rapidly fabricate and test multiple graphite bipolar plate designs using indirect LS. This process involved identifying and selecting suitable graphite powder and binder systems based on their thermal and electrical properties and developing a post process heat treatment method for achieving electrical conductivity of 250 S/cm for LS graphite parts which exceeds the DOE target of 100 S/cm for bipolar plate materials. The post processing also covered a method of infiltration using cyanoacrylate which was capable of rendering porous brown parts fluid impermeable and suitable for use in DMFCs. The cyanoacrylate infiltrated LS graphite parts were characterized for flexural strength and electrical and thermal conductivities and bipolar plates were made and evaluated in a DMFC test stand.

Various flow field designs including plates with varying channel and rib widths and triangular, elliptical and rectangular flow field cross sections were fabricated using indirect LS and their respective polarization curves were compared to commercially machined graphite plates. The fuel cell tests show the improvement in mass transport performance could be due to improved methanol distribution and water removal characteristics of triangular and elliptical cross sectional channels over rectangular channels of equivalent dimensions.

Table of Contents

LIST OF TABLES 14

LIST OF FIGURES 15

CHAPTER 1. INTRODUCTION 1

1.1FUEL CELLS 2

1.1.1 Types of Fuel Cells 2

1.1.2 Polymer Electrolyte Membrane Fuel Cell (PEMFC) 4

1.1.3 Direct Methanol Fuel Cells 5

1.1.4 Bipolar Plates 7

1.1.5 Key Challenges For Fuel Cell Technologies 7

1.2 LASER SINTERING (LS) 8

1.2.1 Indirect Laser Sintering Process 9

1.3 LASER SINTERING OF GRAPHITE BIPOLAR PLATES 10

1.3.1 Research Objectives 10

CHAPTER 2. BACKGROUND 11

2.1 LASER SINTERING 11

2.1.1 Direct Laser Sintering 12

2.1.2 Indirect Laser Sintering 13

2.1.3 Graphite Parts By Indirect Laser Sintering 14

2.2 BIPOLAR PLATES 15

    2.2.1 Materials For Bipolar Plates 15

    2.2.2 Manufacturing of Bipolar Plates 19

    2.2.3 Fuel Cell Testing 21

    2.2.4 Flow Field Designs 22

CHAPTER 3. MATERIALS CHARACTERIZATION AND PROCESSING EXPERIMENTS 28

3.1 INTRODUCTION 28

3.2 FABRICATION OF GRAPHITE PARTS BY INDIRECT LASER SINTERING 29

    3.2.1 CAD Modeling 29

    3.2.2 Indirect Laser Sintering Process Optimization 30

    3.2.3 Binder Carbonization 33

    3.2.4 Infiltration 35

        3.2.4.1 Conductive Epoxy 37

        3.2.4.2 Electroless Nickel Deposition 39

        3.2.4.3 Electrically Conductive Polymers 39

            3.2.4.3.1 Chemical Synthesis 40

            3.2.4.3.2 Electrochemical Polymerization 40

        3.2.4.4 Ethyl Cyanoacrylate 41

3.3 FINISHING 43

3.4 MATERIALS PROPERTY CHARACTERIZATION 44

    3.4.1 Electrical Conductivity 44

    3.4.2 Mechanical Strength 46

3.4.3 Thermal Conductivity 48

3.5 CARBON FIBER ADDITION 48

3.5.1 Materials and Powder Mixing 49

3.5.2 Laser Sintering and Post-Processing 49

3.5.3 Part Characterization 50

3.6 LASER SINTERED GRAPHITE BIPOLAR PLATES 51

3.6.1 Process Validation 51

3.6.2 Testing Novel Bipolar Plate Designs 53

3.6.2.1 Manifolded Bipolar Plates 54

3.6.2.2 Methanol Crossover Measurements 55

CHAPTER 4. RESULTS 60

4.1 INTRODUCTION 60

4.2 INFILTRATION 60

4.2.1 Conductive Epoxy 60

4.2.2 Electroless Nickel Deposition 61

4.2.3 Electrically Conductive Polymers 62

4.2.4 Ethyl Cyanoacrylate 64

4.3 FINISHING 65

4.4 MATERIAL PROPERTY CHARACTERIZATION 66

4.4.1 Electrical Conductivity 66

4.4.2 Mechanical Strength 69

4.4.3 Thermal Conductivity 70

4.5 CARBON FIBER ADDITION 71

4.5.1 Microstructure 71

4.5.2 Flexural Strength 71

4.5.3 Electrical Conductivity 74

4.6 PROCESS VALIDATION 76

4.6.1 Testing Novel Bipolar Plate Designs 77

4.6.2 Comparing Triangular Versus Rectangular Channel Cross Sections 81

4.6.3 Manifolded Bipolar Plates 86

4.7 METHANOL CROSSOVER 87

CHAPTER 5. DISCUSSION 90

5.1 INTRODUCTION 90

5.2 INFILTRATION 90

5.2.1 Metal Based Infiltrants 90

5.2.2 Electrically Conductive Polymers 91

5.2.3 Ethyl Cyanoacrylate 92

5.3 ELECTRICAL CONDUCTIVITY 93

5.4 CARBON FIBER ADDITION 96

5.4.1 Strength and Conductivity of Graphite and Carbon Fibers 96

5.4.2 LS Green Parts 96

5.4.3 LS Brown Parts 97

5.4.4 LS Finished Parts 98

5.5 LS GRAPHITE BIPOLAR PLATES 99

5.5.1 Effect Of Channel/Rib Length, Width And Flow Field Area 100

5.5.2 Comparing Triangular Versus Rectangular Channel Cross Sections ..101

5.5.3 Manifolded Bipolar Plates 105

5.6 DISTRIBUTION OF METHANOL TO THE CATALYST LAYER AS ASSESSED BY METHANOL CROSSOVER 106

CHAPTER 6. CONCLUSIONS AND FUTURE WORK 108

6.1 CONCLUSIONS 108

6.2 FUTURE WORK 111

BIBLIOGRAPHY 113

VITA 122

List of Tables

Table 1.1 Types of fuel cells and key differences [5]. 3

Table 2.1. Key SLS advantages and challenges in the manufacturing process [13]. 11

Table 3.1 DOE targets for bipolar plate properties 28

Table 3.2 Key parameters for laser sintered bipolar plates [22] 31

Table 3.3 Surface energies of infiltrants and substrates adapted from [2] 38

Table 4.1 EDS results of electroless Ni plating on external surface of graphite sample. ..61

Table 4.2 Pycnometer results measuring porosity of graphite infiltration samples. 64

Table 4.3 Electrical conductivity of brown parts with respect to burnout temperature. 67

Table 4.4 Thermal properties of cyanoacrylate infiltrated graphite parts. 70

Table 5.1 Flow field parameters of laser sintered bipolar plates. 99

List of Figures

Figure 1.1 World market energy consumption, 1990 to 2035 (quadrillion Btu) [3]. 1

Figure 1.2(a) Schematic of DMFC working principle, (b) Exploded view of a DMFC stack..........6

Figure 1.3 Schematic of the laser sintering process..........9

Figure 2.1 Classification of bipolar plate materials..........18

Figure 2.2 Classification of bipolar plate fabrication processes..........20

Figure 2.3 a) Serpentine flow field, b) Multi-serpentine flow field, c) Parallel flow field, d) Interdigitated flow field..........24

Figure 2.4 CO_2 gas bubble behavior in a single serpentine flow field and a parallel flow field with 1.0 M methanol fed at 2.0 ml min^{-1} and at 60 °C..........26

Figure 3.1 Laser sintering process for fabrication of graphite bipolar plates..........29

Figure 3.2 Geometric shapes built using single layer scans..........30

Figure 3.3 Differential Scanning Calorimetry of phenolic resin..........32

Figure 3.4 TGA curve of phenolic resin in nitrogen gas atmosphere..........32

Figure 3.5 Relationship between flexural strength and curing temperature for phenolic resins..........33

Figure 3.6 Temperature profile for brown part formation..........35

Figure 3.7 Polymerisation of cyanoacrylate adhesive..........42

Figure 3.8 Relation between curing time of cyanoacrylate and relative humidity 42

Figure 3.9 Setup to measure electrical conductivity using four point probe method 45

Figure 3.10 Three point bend test setup for measuring flexural strength 47

Figure 3.11 a) SSFF 9 passes uniform, b) SSFF 11 passes uniform, c) SSFF 11 passes variable..52

Figure 3.12 a) SSFF 5 cm^2, triangular cross section, 15 passes, b) SSFF 5 cm^2, elliptical cross section, 15 passes c) SSFF 5 cm^2, rectangular cross section, 15 passes ..56

Figure 3.12 d) SSFF 5 cm^2, triangular cross section, 10 passes, e) SSFF 5 cm^2, elliptical cross section, 10 passes f) SSFF 5 cm^2, rectangular cross section, 10 passes ..57

Figure 3.12 g) SSFF 10 cm^2, triangular cross section, 13 passes, h) SSFF 10 cm^2, elliptical cross section, 13 passes i) SSFF 10 cm^2, rectangular cross section, 13 passes 58

Figure 3.13 a) SSFF Manifolded plate, 25 cm^2, b) Cross sectional view of internal channels...59

Figure 4.1 a) EDS linescan of silver epoxy infiltrated graphite sample, b) EDS linescan superimposed on graphite sample 60

Figure 4.2 EDS spectrum of Ni plated graphite sample. 61

Figure 4.3 a) Uncoated exterior of graphite sample, b) Polyaniline coating on sample exterior, c) Interior of sample before deposition, d) Interior after deposition, e) Polythiophene coating on sample exterior, f) Higher magnification of polythiophene surface coating, g) Interior of sample after deposition of polythiophene..63

Figure 4.4 a) Charging observed under the SEM on the external surface of the cyanoacrylate infiltrated graphite samples, b) charging across the interior of cyanoacrylate infiltrated graphite plate, c) brown part before infiltration, d) cyanoacrylate infiltrated bipolar plate (with blooming) 65

Figure 4.5 a) Infiltrated bipolar plate before polishing, b) Infiltrated graphite plate after polishing 66

Figure 4.6 Electrical conductivity as a function of burnout temperature 67

Figure 4.7 XRD patterns of phenolic resin pyrolyzed at different temperatures 68

Figure 4.8a Flexural stress versus flexural strain obtained from three point bending test 69

Figure 4.8b Flexural strengths of samples infiltrated with ethyl cyanoacrylate 70

Figure 4.9 SEM micrograph of an indirect LS brown part containing 26% carbon fiber. Natural graphite and carbon fiber are morphologically distinguished. Dissociated phenolic is clearly present (arrows) and binds graphite and the carbon fiber. 71

Figure 4.10 Flexural strength of green parts after laser sintering. Carbon fiber additions to 26% result in doubling of green part strength. 72

Figure 4.11 Effect of phenolic dissociation temperature and carbon fiber addition on flexural strength of indirect LS brown parts. 73

Figure 4.12 Effect of carbon fiber addition on the flexural strength of final indirect LS parts. 74

Figure 4.13 Effect of phenolic dissociation temperature and carbon fiber addition on the electrical conductivity of laser sintered brown parts. 75

Figure 4.14 Effect of carbon fiber addition on the electrical conductivity of final LS parts (closed symbols). 76

Figure 4.15 Polarization curves of initial plates tested for process validation. 77

Figure 4.16 Polarization curves of plates with 5cm^2 flow field of 10 channel passes.......78

Figure 4.17 Polarization curves of plates with 10 cm^2 flow field of 13 channel passes with the same aspect ratio and channel/rib width as the 5 cm^2, 10 pass plates.........79

Figure 4.18 Polarization curves of plates with 5 cm^2 flow field of 15 channel passes with the same aspect ratio and channel/rib width as the commercial plates. 80

Figure 4.19 Polarization curves of plates with 5 cm^2 flow field of 15 channel passes tested with H_2 and O_2 as the anode and cathode fuels, respectively. 81

Figure 4.20 Polarization curves using a) 1M methanol solution and anode flow rate 6 ml/min, b) 2M methanol solution and anode flow rate of 3 ml/min 82

Figure 4.21 Constant current curves at a) 1.5 A, b) 1.75 A, c) 1.875 A 84

Figure 4.22 Polarization curves obtained by varying cathode flow rates. 85

Figure 4.23 Polarization curves of manifolded plates at varying anode flow rates and fuel inlet configurations...86

Figure 4.24 Methanol crossover comparisons of a) plates made for process validation, b) SSFF 5 cm^2, 10 passes, c) SSFF 10 cm^2, 13 passes, d) SSFF 5 cm^2, 15 passes89

Figure 5.1 Electrochemical stability Pourbaix diagrams for a) Silver, b) Nickel.............91

Figure 5.2 a) Variation of bulk density, kerosene density and open porosity as a function of pyrolysis temperature, b) Electrical resistivity of phenolic resin as a function of pyrolysis temperature...94

Figure 5.3 XRD patterns of phenolic resin after pyrolysis at different temperatures........95

Figure 5.4 Effect of channel shape on the pressure drop in the channels 102

Figure 5.5 Measured water mass profiles for channel property study............................104

Figure 5.6 Enlarged view of slug formation in rectangular (top) and triangular (bottom) channels..105

Figure 5.7 Novel flow field design with single inlet and four outlets 106

Figure 6.1 Corrugated bipolar plates made by indirect laser sintering 112

Chapter 1. Introduction

The rapid development of industrial technologies in the last 100 years has been fueled by a tremendous increase in the demand and supply of energy. This has resulted in an extreme dependence on shrinking fossil fuel reserves that has prompted interest in the field of alternative energy technologies such as wind, solar and fuel cells. As shown in Figure 1.1, the need for energy is steadily rising over the next couple of decades. Though fuel cell technology has existed since the 1800s [1], there has been renewed interest leading to more advancement in the last 20 years than at any other time since its discovery in 1839. This interest has arisen as a direct consequence of increasing public awareness of the limitations of fossil fuels, namely their scarcity and the environmental damage resulting from their production and use [2].

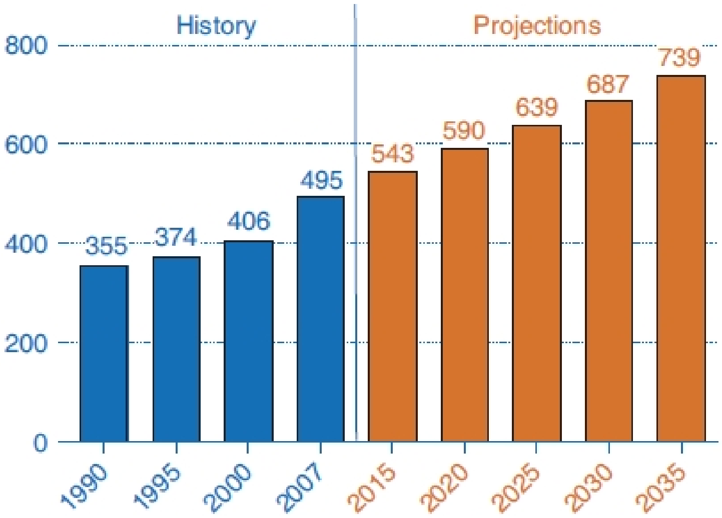

Figure 1.1 World market energy consumption, 1990 to 2035 (quadrillion Btu) [3].

1.1 FUEL CELLS

Fuel cells are electrochemical energy devices that convert the chemical energy (oxidation potential) of reactant fuels (H_2, CH_3OH, CH_4) into electrical energy. They are similar in terms of components to batteries but unlike batteries which are energy storage devices, fuel cells are energy conversion devices. Therefore in fuel cells, as long as fuel is supplied, electrical energy will be produced, whereas batteries will cease to function once the chemical energy is consumed. Fuel cells have distinct advantages when compared to the currently prevalent technologies of the internal combustion engine (ICE) and batteries. Unlike ICEs, fuel cells convert the fuel directly into electricity at efficiencies as high as 84% while not being limited by the Carnot cycle [4]. Also, fuel cells possess no moving parts in regular operation (discounting pumps and compressors in some fuel cell subsystems) which in contrast to ICEs amounts to less wear and tear and therefore maintenance. Most importantly, fuel cells running on H_2 like the polymer electrolyte membrane fuel cell (PEMFC) are clean energy systems that produce nearly zero toxic emissions with the major byproduct of most cell reactions being water, while direct methanol fuel cells (DMFCs) in particular produce CO_2 in addition to the water but are relatively less polluting when compared to combustion engines.

1.1.1 TYPES OF FUEL CELLS

There are several types of fuel cells, including polymer electrolyte membrane fuel cell (PEMFC), alkaline fuel cell (AFC), phosphoric acid fuel cell (PAFC), solid oxide fuel cell (SOFC), and molten carbonate fuel cell (MCFC) that find use in applications varying in operating conditions such as temperature and mobility among others. Table 1.1 describes different types of fuel cells and their primary features.

Table 1.1 Types of fuel cells and key differences [5].

	PEMFC	**AFC**	**PAFC**	**MCFC**	**SOFC**
Electrolyte	Hydrated Polymeric Ion Exchange Membranes	Mobilized or Immobilized Potassium Hydroxide in asbestos matrix	Immobilized Liquid Phosphoric Acid in SiC	Immobilized Liquid Molten Carbonate in LiAlO2	Perovskites (Ceramics)
Electrodes	Carbon	Transition Metals	Carbon	Nickel and Nickel Oxide	Perovskite and perovskite / metal cermet
Catalyst	Platinum	Platinum	Platinum	Electrode Material	Electrode Material
Interconnect	Carbon or metal	Metal	Graphite	Stainless steel or Nickel	Nickel, ceramic or steel
Operating Temperature	40 – 80 °C	65°C – 220 °C	205 °C	650 °C	600-1000 °C
Charge Carrier	H^+	OH^-	H^+	CO3=	O^{2-}
External Reformer for Hydrocarbon fuels	Yes	Yes	Yes	No, for some Fuels	No, for some fuels and cell designs
External shift conversion of CO to hydrogen	Yes, plus purification to remove trace CO	Yes, plus purification to remove CO and CO2	Yes	No	No
Prime Cell Components	Carbon-based	Carbon-based	Graphite-based	Stainless-based	Ceramic
Product Water Management	Evaporative	Evaporative	Evaporative	Gaseous Product	Gaseous Product
Product Heat Management Process	Gas + Liquid Cooling Medium	Process Gas + Electrolyte Circulation	Process Gas + Liquid cooling medium or steam generation	Internal Reforming + Process Gas	Internal Reforming + Process Gas

1.1.2 POLYMER ELECTROLYTE MEMBRANE FUEL CELL (PEMFC)

The PEMFC is a low temperature fuel cell (< 100 °C) that is of high interest in automotive applications and mobile electronics due to its responsiveness to changes in power demand and the portability that is afforded by its low operating temperature. The PEMFC consists of a proton exchange membrane (polymer electrolyte) which is sandwiched between anode and cathode electrodes. Protons and electrons are generated at the anode by the oxidation of the fuel supplied, while oxygen (in some cases from air) is reduced at the cathode. The protons generated at the anode move across the electrolyte membrane to form water and the electrons move through the external circuit generating electricity. The electrochemical processes can be summarized as follows:

Anode: $H_2 \longrightarrow 2H^+ + 2e^-$ $E^o = 0.0$ V (1.1)

Cathode: $\frac{1}{2}O_2 + 2H^+ + 2e^- \longrightarrow H_2O$ $E^o = 1.229$ V (1.2)

Overall: $H_2 + \frac{1}{2}O_2 \longrightarrow H_2O$ $E^o = 1.229$ V (1.3)

The ideal performance of the fuel cell is defined by the Nernst equation which relates the ideal standard potential (E^o) and the ideal equilibrium potential (E) for different temperatures and partial pressures of the reactants and products. The Nernst equation for the above PEMFC overall reaction (1.3) is given as

$$E = E^\circ + \frac{RT}{nF}\ln\left(\frac{P_{H_2} \cdot P_{O_2}^{1/2}}{P_{H_2O}}\right) \tag{1.4}$$

where R is the universal gas constant, F is Faraday's constant, n is the moles of electrons released for every mole of hydrogen reacted (2 mol e^-/ 1 mol H_2), P_x is the partial pressure of species x and T is the temperature.

1.1.3 DIRECT METHANOL FUEL CELLS

The term polymer electrolyte membrane (also known as proton exchange membrane or PEM) fuel cell typically refers to fuel cells operating with hydrogen as the anode fuel. The direct methanol fuel cell (DMFC) uses the same polymer electrolyte membrane as the PEMFCs but with methanol as the anode fuel instead of hydrogen. The DMFC technology is an attractive option as an alternative power source due to the theoretical energy density of methanol which is higher than current Li ion battery technologies and also hydrogen fuel cells. Moreover, methanol fuel is easy to handle and transport, making it a safe and viable means for portable energy solutions. However, issues such as methanol crossover [6] from the anode to the cathode side of the fuel cell and unstable electrocatalysts [7] hamper this technology from achieving widespread use.

A DMFC functions by supplying a methanol aqueous solution directly to the anode of the fuel cell where it is oxidized to CO_2 (Figure 1.2). The H^+ ions are transported across a polymer electrolyte membrane to the cathode where they react with oxygen to form water. A typical DMFC stack is comprised of repeating units of a membrane electrode assembly (catalyst coated electrodes on either side of a polymer electrolyte membrane), diffusion layers, sandwiched between bipolar plates that supply and distribute the fuel, methanol at the anode and oxygen/air at the cathode. The reactions that take place in the DMFC are

$$\text{Anode:} \quad CH_3OH\ (l) + H_2O\ (l) \longrightarrow CO_2 + 6H^+ + 6e^- \quad (1.5)$$

$$\text{Cathode:} \quad 6H^+ + {}^3/_2O_2 + 6e^- \longrightarrow 3H_2O\ (l) \quad (1.6)$$

$$\text{Overall:} \quad CH_3OH\ (l) + {}^3/_2O_2\ (g) \longrightarrow CO_2\ (g) + 2H_2O\ (l) \quad (1.7)$$

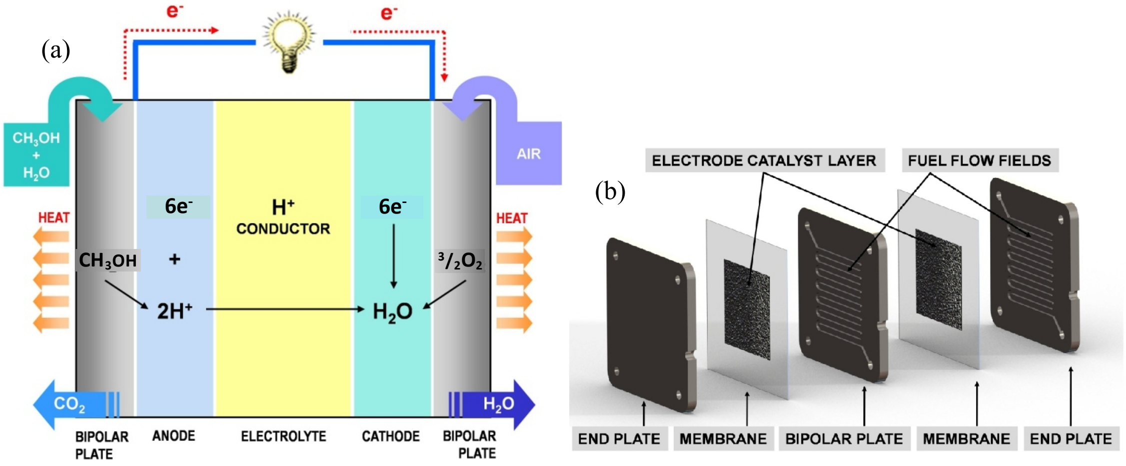

Figure 1.2(a) Schematic of DMFC working principle, (b) Exploded view of a DMFC stack.

The primary advantages of the DMFC are that methanol is a low cost, readily available liquid fuel with high energy density. As seen in equation (1.5), every mole of methanol releases 6 electrons compared to 2 electrons transferred in the hydrogen run PEMFC (1.1). This, coupled with the ease of storage of methanol, makes DMFC technology a viable option in certain applications when compared with hydrogen PEMFCs. As mentioned earlier, one of the most pressing issues with the DMFC is the crossover of methanol from the anode to the cathode side. This happens readily as methanol in water is carried across the electrolyte membrane to the cathode side. Not only is this crossover a loss of fuel, the catalysis of the methanol at the cathode side manifests as a reduced open circuit voltage (OCV) and also degrades the platinum catalyst thereby affecting the oxygen reduction reaction. The current methods of alleviating methanol crossover include, diluting the anode methanol concentration (~1M for optimum performance and reduced crossover [8] and increasing the thickness of the electrolyte membrane which consequently increases the interfacial resistance of the cell.

Another problem with the DMFC is that the methanol oxidation reaction at the anode is sluggish due to poor activation kinetics which results in much lower power when compared to hydrogen cells. This makes the DMFC unsuitable in applications requiring high power densities such automobiles and stationary power but suitable in cases where low power (a few watts to 1 kW) is needed for extended periods such as laptops, mobile phones, digital cameras etc.

1.1.4 BIPOLAR PLATES

Bipolar plates are one of the most significant components in a fuel cell in terms of function and have been estimated to represent 15 – 29% of the overall cost [9]. They account for more than 80% of the total weight [10]. They perform the functions of providing structural support, supplying fuel to the cell and serving heat and water management roles within the cell. Conventionally, bipolar plates are made of graphite due it being lightweight, corrosion resistant and possessing thermal and electrical conductivity. However due to the prohibitive costs of machining the flow fields on the plates and the poor mechanical properties of graphite, alternative materials and manufacturing processes are being actively researched.

1.1.5 KEY CHALLENGES FOR FUEL CELL TECHNOLOGIES

Lack of familiarity and infrastructure, insufficient longevity and reliability, and high cost have curtailed wider commercialization of fuel cell technologies [11]. There are several economical and technological challenges. Some of the primary economical hurdles affecting fuel cell technology in general include, cost of the fuel cell system, competing alternative energy technologies and the cost of setting up the infrastructure for the production and distribution of the fuel. The technical challenges include developing effective and low cost catalysts, reducing system operating costs and improving cell life and durability. Advancements over the last decade have enabled a reduction of ~80 % in the cost of the fuel cell stack from around $275/kW in 2002 to around $51/kW in 2010, slightly higher than the original DOE target of $45/kW by 2010 [12]**.** The major costs in the fuel cell can be ascribed to the precious metal catalysts, the bipolar plates and the electrolyte membrane.

1.2 LASER SINTERING (LS)

Freeform fabrication is a collection of technologies also known as rapid prototyping, rapid manufacturing and solid freeform fabrication, and more broadly as a subset of additive manufacturing [13]. A common characteristic of these technologies is the application of additive, layer-wise method in the fabrication process [14]. Many manufacturing scientists and engineers consider rapid prototyping to be the ultimate solution to manufacturing whereby complex and near-impossible shapes can be modeled and developed within a very short period. There are about 25 varied rapid prototyping methods available today, of which about 70% are based on laser application [13]. Indirect Laser Sintering (LS) is a rapid manufacturing process in which a three dimensional object can be built using a wide variety of materials from a Computer Aided Design (CAD) model and through an additive fabrication method. The LS process was developed by the University of Texas in Austin in the 1980s and then commercialized by DTM Corporation with support from B. F. Goodrich. The first LS machine was shipped in 1992 [14].

1.2.1 INDIRECT LASER SINTERING PROCESS

At the beginning of the indirect Laser Sintering (LS) approach, a three dimensional CAD model representing the part is decomposed into two dimensional thin layers called sintering planes which are stored as an STL file and subsequently transferred to the LS machine. The LS process begins with depositing a powdered material to form a uniform powder bed in the working space. A CO_2 laser beam then selectively raster scans the first layer to form an area or contour defined by the geometry of the two dimensional cross-section.

After the first layer is sintered, the build chamber platform moves down with a specified layer thickness, and a new powder layer is spread out and leveled over it via a roller mechanism. The laser scans the new layer to fuse the previous layers together through a variety of fusing mechanisms including surface bonding and melting. The procedure is repeated until the shape is completely built up. During the sintering process, the un-fused loose powder remains in place and serves as the support for the next layer of powder and part under fabrication. No additional support structure is required. The loose powder may be sifted in a sifter for reuse. Figure 1.3 shows a schematic of the LS process.

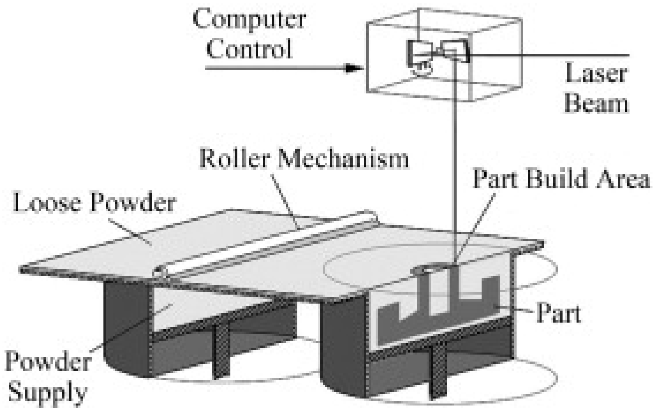

Figure 1.3 Schematic of the laser sintering process

1.3 LASER SINTERING OF GRAPHITE BIPOLAR PLATES

1.3.1 RESEARCH OBJECTIVES

The primary goal of this dissertation research is to develop a novel manufacturing process for DMFC bipolar plates using indirect LS. The research will focus on the fabrication of viable prototypes for testing DMFCs. As an extension of work done at The University of Texas at Austin, the project aims to achieve the following targets:

1) Electrical conductivity of the indirect LS graphite plates to exceed 100 S/cm.
2) Infiltration of the porous preforms so as to achieve impermeability of the bipolar plates to prevent fuel leakage during fuel cell operation.
3) The improvement of DMFC performance by designing and testing bipolar plates with novel flow fields.

The establishment of this process is expected to significantly benefit fuel cell bipolar plate designers since prototype bipolar plates can thus be constructed and tested in a short period of time and at low cost.

This dissertation is organized as follows. In Chapter 2 are reviewed the related research for this work with the motivation for the current research. Chapter 3 describes the experiments conducted in the course of this work towards producing graphite bipolar plates that meet materials property requirements set by the DOE. Chapter 4 presents the results of the experiments conducted. In Chapter 5, the results of the experiments are analyzed and discussed. The conclusion of the research and possibilities for future work are presented in Chapter 6.

Chapter 2. Background

2.1 LASER SINTERING

Laser sintering (LS) affords building of complex designs and shapes in a single step, where complexity of a build is not a limiting factor. Reducing production costs, testing complex designs and achieving a repeatable production process are the primary motivation for pursuing LS as a manufacturing technique in this application. An overview of key advantages of LS and challenges accounted for are provided in Table 2.1

Table 2.1. Key SLS advantages and challenges in the manufacturing process [13].

Advantages of SLS	**Challenges with SLS**
Any powder that can be sintered or that will bond without melting can be used	Large flat sheets need tie-down supports to avoid curling
The materials are non-toxic	Part accuracy depends on size and complexity
SLS does not usually require support structures	The surface finish is rough; the article is porous and hence of poor mechanical strength
Accuracy in the range of ±0.05 - 0.25 mm	The equipment is expensive. However cost savings as compared to conventional methods outweigh this consideration
Fairly good speed. Reduces lead time from design to product from several months to weeks or days when compared to conventional manufacturing	Cavities are difficult to clean since the powder tends to cling and bead blasting is difficult in confined regions
The finished parts can be functional and testable prototypes as well as conceptual models	Shrinkage can create residual stresses which can cause distortion or cracking
Fully automatic process. No tooling or human intervention needed.	Temperature control is critical

The Laser Sintering process can be classified into two groups, direct LS and indirect LS. These are discussed in further detail in the following sections.

2.1.1 DIRECT LASER SINTERING

Direct laser sintering produces fully dense final parts directly without the need for any post-processing steps. The materials used in Direct LS processes consist of thermoplastic powders, such as nylon-based materials, metals and ceramics. While thermoplastic materials require fewer than 20 Watts to achieve a fully dense plastic part, metals and ceramics require much higher laser power and atmospheric control in comparison. The most commonly used polymer is polyamide and it has become synonymous with SLS plastics [15, 16, 17, 18]. Research at The University of Texas at Austin has shown that using a mixture of high melting point and low melting point metal powders such as Cu-Pb/Sn [19] and Cu/Sn(Bronze)-Ni [20] can partly overcome the need for higher laser power. However, the surface finish of these parts suffers due to the balling effect that occurs during processing. With the introduction of powerful high quality lasers, the partial melting of LS has been taken over by complete melting giving rise a new development of Selective Laser Melting (SLM). Needless to say, SLM is LS done at high laser powers with an aim to achieve complete melting of powders.

The solid-liquid ratio of powder is an important feature in successful direct SLS metal parts. Liquid phase viscosity and solid phase wetting behavior also play a role in the process. Insufficient atmosphere control can result in poor wetting between the molten liquid phase and solid phase of metal powder that normally has an oxide layer in its as-received form [7].

2.1.2 INDIRECT LASER SINTERING

Indirect LS involves the use of a polymer binder to produce a green part. The process enables the production of solid parts from high melting material systems that a 50 W CO_2 laser would normally not be able to fuse. High melting ceramics and inter-metallics can be mixed with a thermosetting polymer which acts as a sacrificial binder to form a 'green' part. The mechanical and electrical properties of the green part may be improved upon burnout of the binder to form a 'brown' part. The ideal binder should have a low melting point and high bond strength to produce parts that can maintain geometric integrity through post-processing. It is also possible to create a fully dense part to improve mechanical strength upon the completion of post-processing treatment. Currently, two of the most widely used post-processing steps are conventional pressureless sintering and an infiltration process.

Another post-processing step called Hot Isostatic Pressing (HIP) has also been investigated at The University of Texas at Austin to produce fully dense parts by compaction under an external pressure from a compressed argon gas at elevated temperature [21]. Because of the source of the applied pressure, a uniform force can normally be exerted on the part being compacted. Ideally, this can result in uniform shrinkage of the part without any distortion if the initial porosity is uniformly distributed. One of the advantages of the HIPping process is that full densification of the part can be accomplished in a relative short period of time compared to conventional furnace sintering techniques while the primary disadvantage of HIPping process is its high cost.

2.1.3 GRAPHITE PARTS BY INDIRECT LASER SINTERING

Graphite is well-known for its high thermal stability and chemical inertness, which makes it a good candidate for electrochemical system parts and refractory products. The theoretical density of graphite is 2.25 g/cm^3, which is relatively low compared to most metals. Its light weight further makes it an attractive material for bipolar plate fabrication. Graphite possesses a layered structure where each plane is linked to adjacent planes by weak Van der Waals forces that allow them to slide over one another easily, making graphite an ideal lubricant. The electrical conductivity of graphite mainly comes from delocalized electrons across the hexagonal atomic sheets of carbon, and the conductivity in the plane of the sheets is greater than that perpendicular to the sheets.

Prior work at The University of Texas at Austin has shown processes developed for the production of parts made from graphite and silicon carbide by indirect laser sintering [22, 23]. They involve the mixing of the high melting matrix constituents, graphite or silicon carbide with a suitable thermosetting binder such as phenolic resin, wax or nylon to serve as the connecting media in the green part to maintain geometric integrity for subsequent post processing. The graphite parts obtained by laser sintering were subjected to high temperature heat treatment to remove the binder and improve the mechanical strength of the part. Full densification of the porous brown part was achieved by infiltrating with a suitable polymer infiltrant such as epoxy resin or in the case of silicon carbide, molten silicon.

Shrinkage of the brown parts due to the mass loss of the phenolic resin binder during carbonization was observed by Chen et al [22]. It was quantified to be about 4 % in both x and y directions and about 15 % in the z direction. This shrinkage if not accounted for would result in large inaccuracies in final part dimensions. This can be remedied by scaling up the CAD models by the anticipated amount.

2.2 BIPOLAR PLATES

Bipolar plates separate the individual cells in a fuel cell stack with end plates as the final components on the outside. Flow fields are present on both sides of a bipolar plate and on only one side of end plates. Regardless, bipolar plates and end plates have similar materials, functions and design requirements within a fuel cell stack. Some of the important functions of a bipolar plate within a fuel cell include:

1) Distributing the reactants (gas and liquid phases) uniformly to the membrane electrode assembly (MEA) and removing the reaction products at the same time.
2) Providing an electrical connection across the series of cells within the fuel cell stack.
3) Providing the mechanical rigidity to support the load of the fuel cell stack.
4) Aiding in thermal management by removing heat produced at the active area.

The above functions of bipolar plates are facilitated by the materials used in the fabrication and the design of the plates themselves. The following sections review the various aspects of bipolar plate design and fabrication.

2.2.1 MATERIALS FOR BIPOLAR PLATES

The most commonly used material for bipolar plates is currently graphite. There are a range of materials that have been researched and are currently being evaluated for suitability as bipolar plates [24, 25, 26, 27]. Since the performance of the fuel cell is highly dependent on the performance of the bipolar plates, the properties of the materials selected is highly critical and has therefore been required by the DOE to meet target values for performance critical characteristics. The DOE targets include cost (< \$10/kW), corrosion resistance (< 16 $\mu A/cm^2$), electrical conductivity (> 100 S/cm), and ease of manufacture to name a few [28]. With these factors in mind, it is important to note that not all materials will meet the requirements and that to attain the desired properties, additional processing such as surface modifications (corrosion resistant coatings), thermal treatments, alloying etc. may be required.

Conventionally, bipolar plates are made out of POCO^{TM} graphite due to its superior corrosion resistance, low specific density and its ability to maintain low electrical contact resistance with the backing materials [29]. The fabrication of these plates is by first molding a blank plate using a flat graphite and resin composite upon which the flow field is machined. Due to the poor machinability and low strength of the graphite, this process suffers from high machining costs, low production rates and high material loss. Furthermore, bipolar plates made this way cannot be formed into thin configurations and thick sheets of graphite are required, increasing the weight and volume of the stack. The other materials that have been developed for bipolar plate fabrication are predominantly carbon-polymer composites and metallic materials. Most of the interest is currently focused on the processing of carbon- polymer composite material as well as developing new manufacturing techniques to meet the requirements.

The benefits of using metallic bipolar plates are reduced plate thickness, improved electrical conductivity and good mechanical strength, which translate to reduced stack weight and manufacturing costs. Some of the commonly researched metallic materials for bipolar plates are aluminum, titanium, stainless steel and nickel alloys [30, 31, 32, 33]. Stainless steel with a variety of alloying elements including, chromium, nickel, molybdenum and manganese is a low cost material that is widely used to make bipolar plates. It is easy to easy to shape and can be stamped into sheets as thin as 0.5 mm, reducing the net volume of the fuel cell stack. The capability of being made thin also helps to compensate for the higher density compared to graphite. Its mechanical properties also enable other deforming processes such as machining, forging and casting. However, the primary drawback of using stainless steel bipolar plates is that it is highly susceptible to corrosion, which can lead to the dissolution of the metal as well as the releasing of multivalent cations into the MEA, thereby poisoning the electrode catalysts and contaminating the electrolyte. Stainless steel forms a passive film on its surface which has been identified to comprise of chromium oxides such as Cr_2O_3 along with small amounts of iron oxide. Although the surface passive film protects stainless steel plates from corrosion attack, it also increases the contact resistance thus reducing the fuel cell performance [34].

Titanium and aluminum are also popular choices as bipolar plate materials due to their light weight compared to stainless steel plates [32, 35]. Like stainless steel, titanium and aluminum are both electrically conductive and ductile, making for easy machining. Titanium is, however, too expensive to be used extensively. It also forms a passivating layer on the surface that increases the contact resistance and deteriorates the fuel cell performance. Similar strategies such as surface coating (gold, nitride) could be implemented to prevent corrosion attack, but adds to the already prohibitive material costs. Currently, titanium plates are being researched more for aerospace applications than for automotive uses where cost is a major factor. Aluminum, though lightweight and inexpensive compared to titanium and stainless steel, is more susceptible to corrosion attack since no passive film is formed on its surface.

Corrosion in most metallic plates is handled by applying surface coatings. Application of low resistance thin surface coating (e.g. gold, nitride) [32], reduces the contact resistance between the bipolar plate and the MEA. It also lessens the degree of contamination in the membrane. However, the coating process is usually very costly which often outweighs its benefits. It is thus more favorable to develop uncoated stainless steel plates that are free from degradation due to corrosion in the fuel cell environment.

Carbon based composites are another group of materials that have shown promise as materials for bipolar plates [36]. Standard composite mixture consists of either thermoplastic or thermoset binders mixed with carbon-based compounds. Figure 2.1 summarizes the classification of materials [37] that have been investigated for the fabrication of PEMFC bipolar plates. Additional fiber additives may also be added to increase the final strengths and conductivity. Most of the composite material systems are well-suited for bipolar plate fabrication using alternate techniques such as molding, thus significantly reducing the fabrication cost.

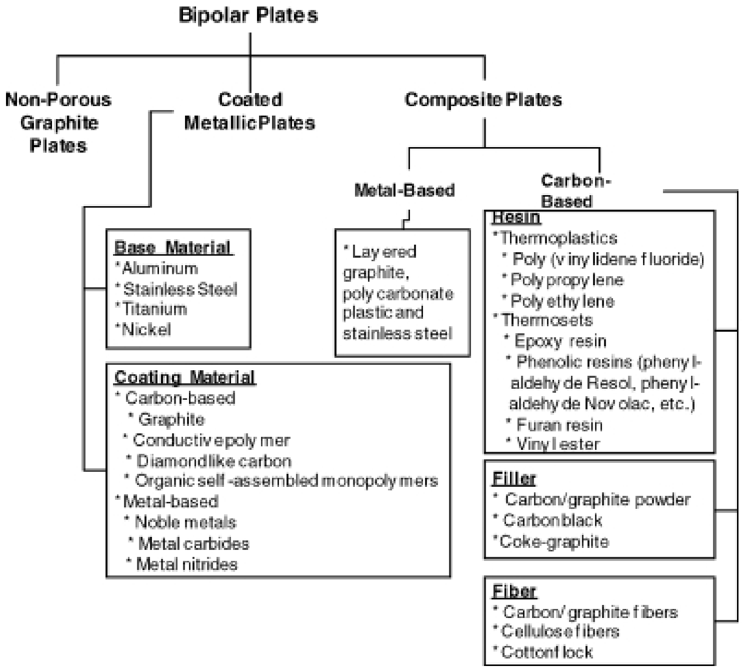

Figure 2.1 Classification of bipolar plate materials [37].

2.2.2 MANUFACTURING OF BIPOLAR PLATES

The fabrication process for the manufacturing of bipolar plates should be able to meet cost and volume requirements. Pure graphite bipolar plates are traditionally manufactured by machining which is a costly and time consuming process due to the brittleness of graphite combined with the fineness of the flow field features. Compression molding and injection molding are two alternative high volume manufacturing methods that have been investigated for manufacturing bipolar plates [38, 39, 40]. In compression molding, a graphite mixture composed of crystalline graphite powder and binders such as thermosetting vinyl resin and reinforcing fibers like carbon, glass cotton, etc. are molded at temperatures ranging from 10 ºC to 100 ºC with compression forces varying from 5 to 100 kN. Bipolar plates have been successfully compression molded with cure times less than 30 seconds with reported electrical conductivities of the graphite composite bipolar plates around 50 S/m.

Injection molding involves extruding a mixture of carbon powder and thermoplastic resins which are then heated and reshaped by the injection molding process into bipolar plates. Injection molding has the advantage of reducing cycle times to fulfill mass volume production demands. Cycle times as low as 30 to 60 seconds to fabricate a plate have been reported [40]. Figure 2.2 shows the classification of fuel cell bipolar plate fabrication techniques [37].

Metallic foams are one of the more novel materials used as bipolar plates [41, 26]. The foam is essentially a sponge made from different metals including Ni-Cr and 316 stainless steels that uniformly distributes the reactants in the cell. Due to their high stiffness and low specific weights, these foams reduce the weight of the fuel cell stack and simplify the stack design as the metal foam would act as the gas flow field, electrode and catalyst support. Moreover, it was found that metal foams exhibit better polarization performance than conventional multi-parallel flow field designs. However, metal foams are susceptible to corrosion common in most metallic bipolar plates.

At this point, both injection molding and compression molding are considered two of the most promising methods for mass volume production of bipolar plates [42]. Currently, there is no clear consensus as to which combination of material and fabrication technique is the best, since they all have their own advantages and disadvantages. One thing generally agreed on is that an alternative manufacturing process to the machining of graphite is required for the commercialization of fuel cell technology.

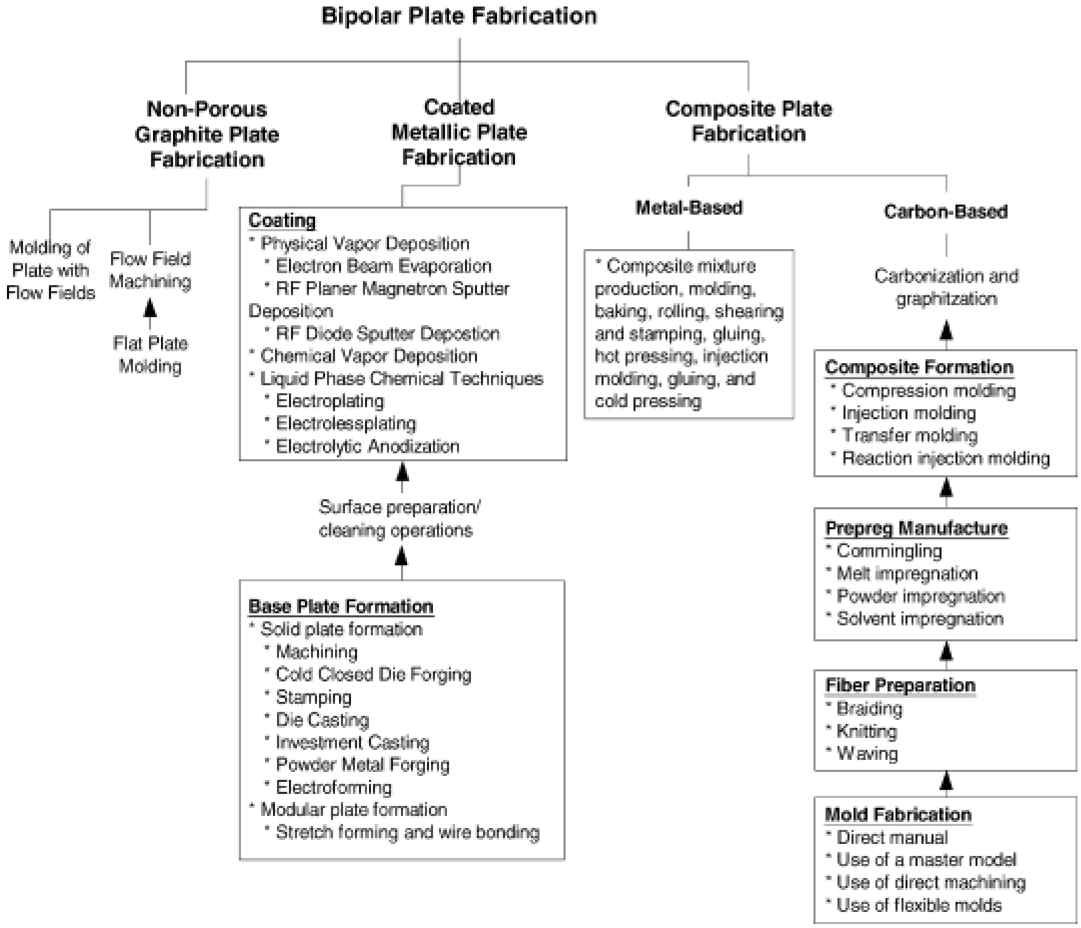

Figure 2.2 Classification of bipolar plate fabrication processes [37].

2.2.3 FUEL CELL TESTING

Ideally, a fuel cell should function at the theoretical optimum cell voltage of 1.2 V at all operating currents. In reality however, fuel cells achieve the highest output voltage, which is typically lower than 1.2 V, at open circuit (no load) conditions and the voltage drops off as the current draw increases. This is known as polarization and is represented by a polarization curve as shown in Figure 2.5. Additionally, Figure 2.5 also depicts a power density curve. The polarization curve characterizes the cell voltage as a function of current and the current, in turn, depends on the size of the electrical load placed across the fuel cell. The polarization curve shows the electrochemical efficiency of the fuel cell at any operating current since the efficiency is the ratio of the actual cell voltage divided by the theoretical maximum of 1.2 V.

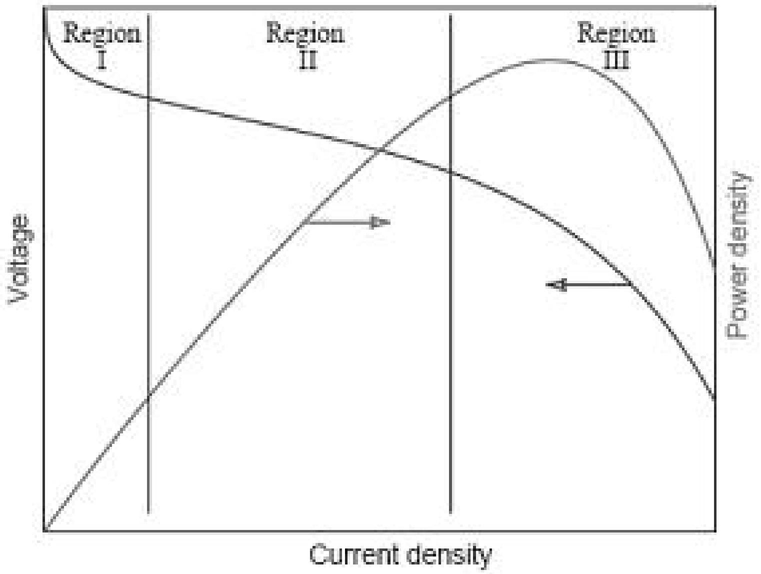

Figure 2.5 Polarization curve used in characterizing fuel cell performance [43].

Region I shows the low current density portion of the polarization curve where the shape of the curve is governed by the activation overpotential. This arises from the kinetics of the charge transfer reactions taking place in the cell and is dependent on factors such as the type of reactions, catalyst used, temperature, the electrolyte material etc. Region II represents the linear portion of the curve following the rapid drop due to the activation polarization. In this region, the shape of the curve is governed by the ohmic losses experienced in the cell which arise from the resistance of the various components of the fuel cell. Region III represents the high current density portion of the curve where the shape of the curve is determined by the mass transfer overpotential. At high current densities, the sluggishness of mass transfer limits the amount of reactants reaching the catalyst layer and therefore the cell voltage rapidly decreases with increasing load.

2.2.4 FLOW FIELD DESIGNS

The efficiency of a fuel cell depends on the kinetics of the electrochemical reactions that take place within the cell. The design of the flow field is critical in improving and ensuring efficient operation of the fuel cell. Though there are a variety of flow field designs that are currently used in bipolar plates, the serpentine design and its variations are the most commonly used patterns. Figure 2.3 shows some of the more popular flow field patterns [44].

The single serpentine flow field is essentially a single path that weaves multiple passes from inlet to outlet. This reduces the chance of water accumulating in the channels thereby improving performance. A disadvantage of this design is that since the reactant is depleted through the length of the channel, sufficient amounts of fuel must be supplied to prevent excessive polarization losses. A multi-serpentine flow field possesses several parallel serpentine channels that flow fluids from inlet to outlet. The advantage of this channel type is that the reactant pressure drop is lower than in the single serpentine channel and water stagnation at the cathode is significantly reduced. In the parallel flow field design, there is less mass flow per channel and more uniform reactant distribution with a reduced pressure drop. However, water accumulation at high current densities is inevitable which can lead to an uneven flow distribution between parallel channels over time resulting in dead zones. Interdigitated or discontinuous flow fields have channels that are dead-ended which increase the gas diffusion into the diffusion layer, thereby enhancing water removal from the electrode structure. This design has been reported in literature [44] to be particularly effective on the cathode side when compared to conventional serpentine channels.

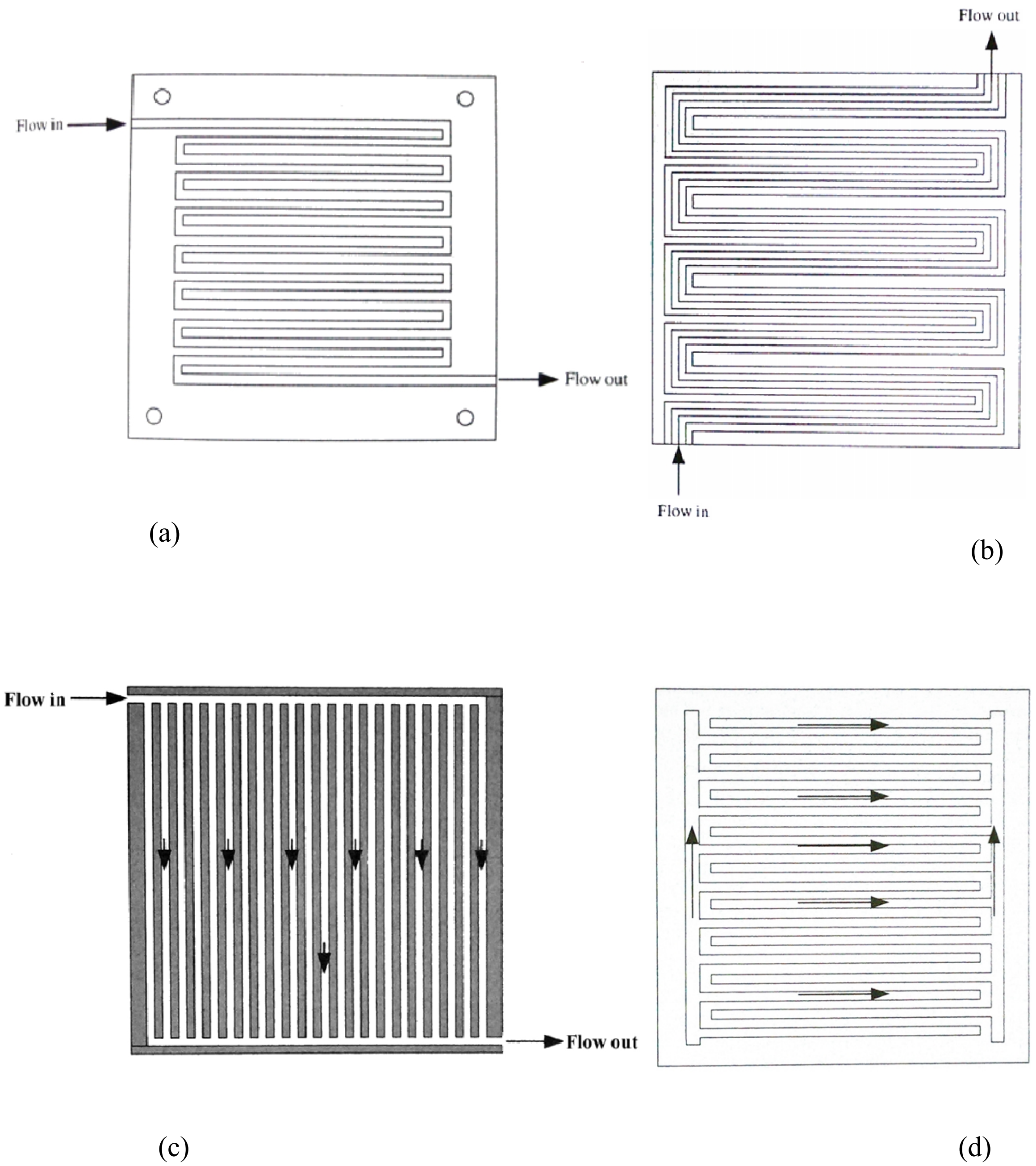

Figure 2.3 a) Serpentine flow field, b) Multi-serpentine flow field, c) Parallel flow field, d) Interdigitated flow field [44].

It is apparent that along with the flow field designs, the size, shape and orientation of the channels in the flow field have a significant effect on the performance of the fuel cell. Recently, there have been numerous studies on the influence of flow field channel parameters on the performance of the fuel cell [45, 46, 47, 48]. The results of these studies have shown that:

1) Decreasing channel cross-section increases gas flow velocity which enhances liquid water removal.
2) Decreasing rib width facilitates the passage of water and gases through the gas diffusion layer. However, this also increases the pressure exerted on the diffusion layer which can have adverse effects such as intrusion of the gas diffusion layer into the channel.
3) Pressure drop across the channels aids in the removal of liquid water. However, it also results in lower system efficiency due to the increase in power consumption of the air supply system.

Research by Yang et al. [49] has shown the behavior of CO_2 within the channels of serpentine and parallel flow fields under varying channel dimensions and current densities. The effects of cell orientation, methanol solution flow rate, and operation temperature were also investigated. Figure 2.4 shows the different two-phase flow patterns observed in parallel and serpentine anode flow fields. It was found that under the same conditions more gas CO_2 bubbles were presented in the parallel flow field as the sweeping rate of the gas bubbles in the parallel flow field was lower than that in the serpentine flow field. Channel-clogging was not seen under all testing conditions in the single serpentine flow field, indicating that the serpentine flow field has superior gas CO_2 removal ability than does the parallel flow field.

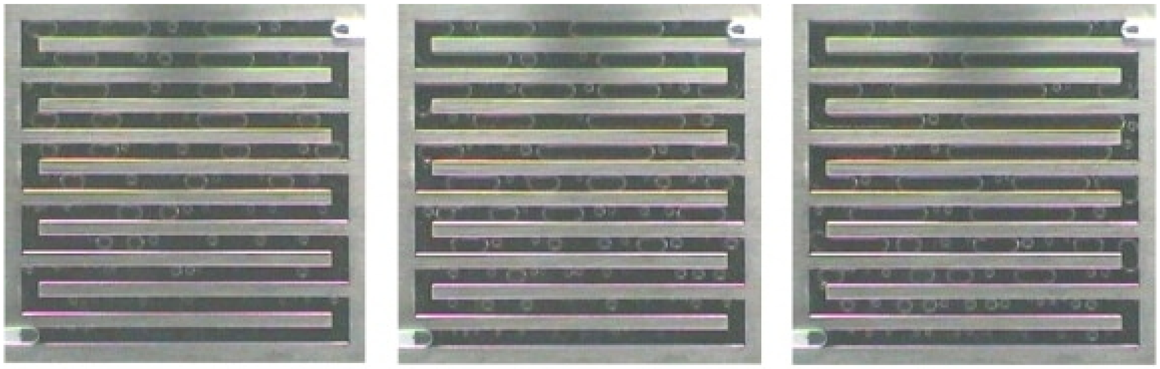

(S-1) 50 mA cm^{-2} (S-2) 100 mA cm^{-2} (S-3) 200 mA cm^{-2}

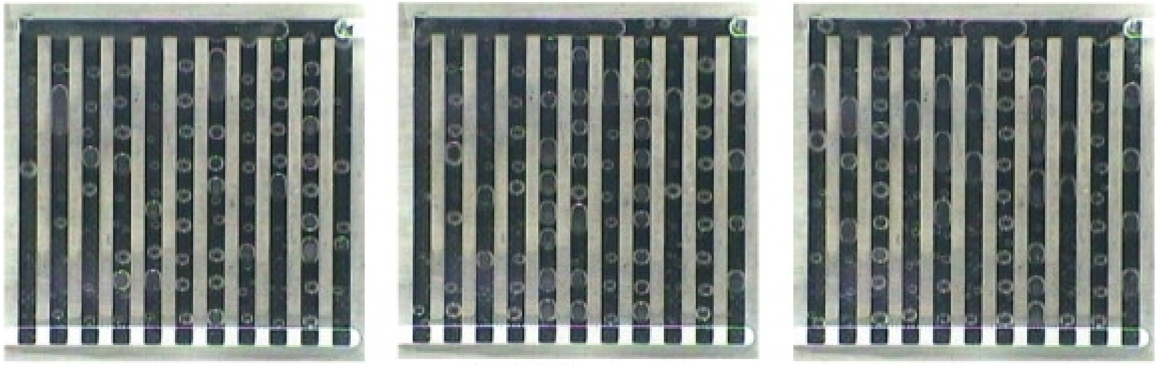

(P-1) 50 mA cm^{-2} (P-2) 100 mA cm^{-2} (P-3) 200 mA cm^{-2}

Figure 2.4 CO_2 gas bubble behavior in a single serpentine flow field and a parallel flow field with 1.0 M methanol fed at 2.0 ml min^{-1} and at 60 °C [49].

Investigation of the effect of channel depth of a micro-scale serpentine flow field, with the channel depth varying from 1 mm to 0.410 mm has shown that reducing the channel depth of the micro-scale channel can lead to two opposite effects on the mass transport [50]. On one hand, the reduction in channel size can lead to a higher liquid flow rate, which will yield a higher mass transfer coefficient at the channel/anode diffusion layer interface and under-rib convection, thus improving the cell performance. On the other hand, the reduction in channel size can also cause serious gas slug blockages, which can hinder the mass transport of methanol, thus degrading cell performance. Therefore to balance these two effects, an optimum channel depth exists for the same channel width at the same methanol flow rate.

As mentioned previously, designing and testing of flow field designs can be simplified by the use of rapid manufacturing methodologies. Indirect LS of graphite bipolar plates would not only help in the rapid testing and analysis of the effects of varying dimensions and shapes of the flow channels, but also in the design and fabrication of entirely new designs of plates that cannot be conventionally produced.

Chapter 3. Materials Characterization and Processing Experiments

3.1 INTRODUCTION

The fabrication of graphite parts by indirect LS, while relatively unconstrained in terms of part geometry or complexity, has two major drawbacks, namely, poor electrical properties and porosity of parts produced. These are serious issues when considering the application of bipolar plates in fuel cells. The primary functions of a bipolar plate is to efficiently supply/distribute the fuel and collect the electrons produced by the electrochemical reaction. To that end, impermeability and conductivity are properties of the plates that are highly critical in minimization of fuel leakage and internal resistances, respectively.

The Department of Energy (DOE) has set minimum targets for properties that bipolar plates need to meet to ensure efficient operation in fuel cells. Table 3.1 summarizes the basic mechanical, electrical and permeability properties that were targeted in this research. This chapter discusses the experiments conducted to produce and test electrically conductive, fluid impermeable graphite bipolar plates using indirect laser sintering.

Table 3.1 DOE targets for bipolar plate properties

Properties	**Department of Energy Targets**
Electrical Conductivity	>100 (S/cm)
Flexural Strength	>600 (psi)
Corrosion Rate	<16 ($\mu A/cm^2$)
Gas Permeability	<16x10^{-6} (cm^3/cm^2-s)

3.2 FABRICATION OF GRAPHITE PARTS BY INDIRECT LASER SINTERING

A process to produce graphite parts by indirect selective laser sintering was developed by Ssuwei Chen and David Bourell, UT Austin [51]. The process as shown in Figure 3.1 involves preparing a mixture of the graphite powder and phenolic resin binder which is loaded into the Sinterstation. The CAD model built is entered into the machine and is subsequently broken down into a number of layers. A CO_2 laser then sinters the powder mixture according to the order of layers in the STL file. This forms a green part which is carbonized at high temperatures in a vacuum furnace to remove the binder and for the brown part. After liquid phenolic is infiltrated into the brown part and re-cured at 800 ºC to improve electrical conductivity, liquid epoxy resin was used to seal the open porosity of the brown part.

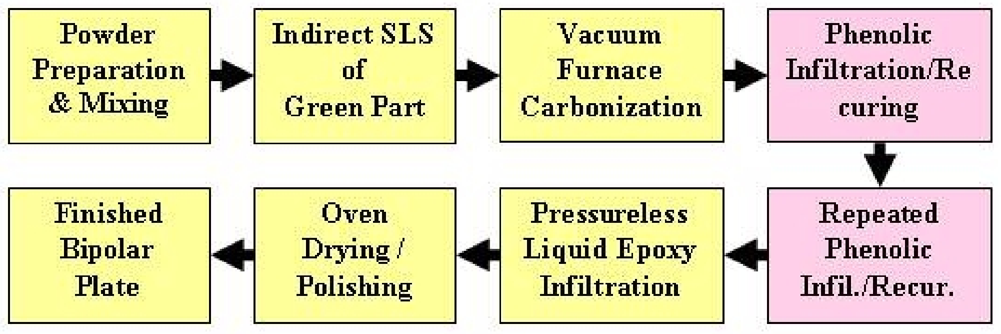

Figure 3.1 Laser sintering process for fabrication of graphite bipolar plates [22].

3.2.1 CAD MODELING

CAD models of the graphite parts to be fabricated were made using SolidWorks and converted to STL format which translates the 3D CAD model into a logical series of triangles. This STL file is inputted to the Sinterstation 2000 where it is sliced into a specified number of layers that when sintered form the whole object.

3.2.2 INDIRECT LASER SINTERING PROCESS OPTIMIZATION

The current research used the process developed by Ssuwei Chen [22] as the basis for indirect laser sintering of graphite powder and further optimized to improve the mechanical and electrical properties of the graphite bipolar plates. The quality of parts was found to be highly dependent on laser sintering parameters of temperature, laser power, feed distance and powder layer thickness. Based on analysis of part and feed bed temperatures in conjunction with single powder layer scans, the optimum part and feed bed temperatures were selected. The purpose of the single layer scans consisted of building simple shapes (Figure 3.2) whose part resolution and ability to maintain shape during handling were used to determine the suitability of the build parameters.

Figure 3.2 Geometric shapes built using single layer scans.

Based on differential scanning calorimetry results of the phenolic powder, the part bed and feed bins were maintained at 65 and 47 ºC, respectively, to ensure that the phenolic powder bed that was not laser sintered remained stable without being thermally affected. The parameters for the indirect LS process were: fill laser power (10-20 W), outline laser power (4 W), powder layer thickness (0.1016 mm), laser scan spacing (0.0762 mm), laser scan speed (1.524 m/s). Table 3.2 summarizes the process settings developed by Chen et al. for the laser sintering of graphite parts. These settings were modified for new batches of powder based on part quality and thermal properties of the powder mixture.

Table 3.2 Key parameters for laser sintered bipolar plates [22]

Powder Constituents	Graphite particle (GrafTech GS150E) and Phenolic resin (Georgia Pacific GP5546)
Composition	70 w% graphite and 30 w% phenolic resin
Particle Size	Graphite: 90% < 100 μm 50% < 55 μm Phenolic resin = 11 μm
Powder Mixing	Roller mixed
SLS Machine	DTM Sinterstation 2000
CO_2 Laser Power	10 ~ 20 Watts
Laser Scan Speed	60 in/s
Laser Scan Spacing	0.003 inch
Powder Layer Thickness	0.004 inch
Andrew Number	6.5 ~ 12.9 J/cm^2
Atmosphere Control	Inert gas, N_2
Powder Bed Preheating Temp.	60 ºC

Since the material system being sintered is high melting point graphite and phenolic resin, one of the most important criteria is that the preheating temperature must not exceed the temperature at which crosslinking of the phenolic binder commences. A Perkin Elmer DSC7 Differential Scanning Calorimeter and Perkin Elmer TGA7 Thermo Gravimetric Analyzer (TGA) equipment were used to analyze the phenolic resin. From Figure 3.3 which shows the DSC curve for phenolic resin, the exothermic peak representing the crosslinking mechanism, occurs at just above 150 ºC. Figure 3.4 shows the TGA curve of phenolic resin from room temperature to 500 ºC [22]. The test was conducted under nitrogen environment with a heating rate 10 ºC/min. No significant weight loss occurs prior to 80 ºC meaning that phenolic remains stable without too much degradation. Based on the DSC and TGA results, a powder bed temperature range of 60 ºC to 80 ºC was used for the material system.

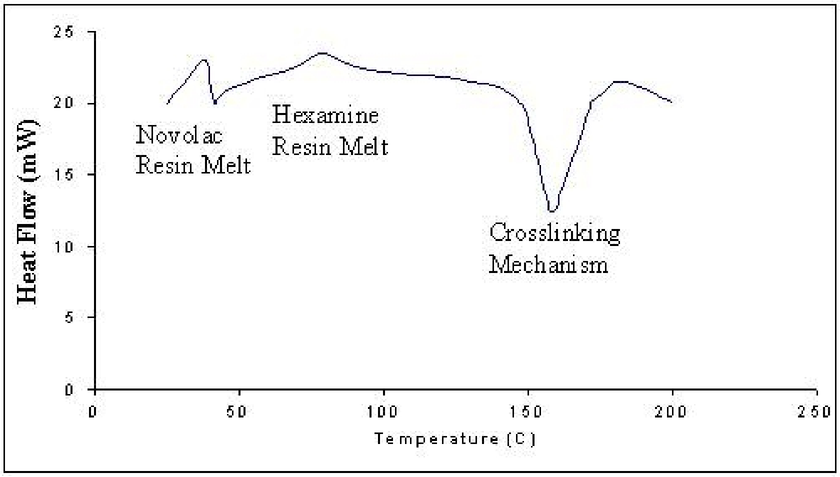

Figure 3.3 Differential Scanning Calorimetry of phenolic resin.

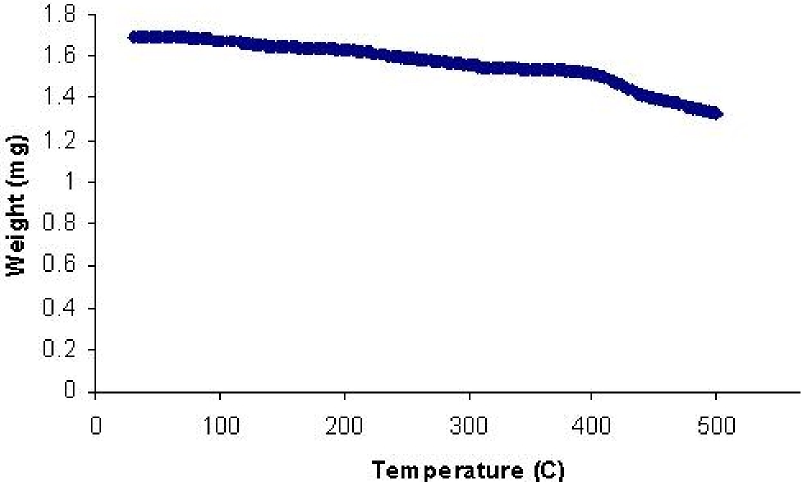

Figure 3.4 TGA curve of phenolic resin in nitrogen gas atmosphere [22].

3.2.3 BINDER CARBONIZATION

Upon successfully building a green part using the selective laser sintering process, a brown part was formed by pyrolyzing the phenolic resin binder to form polymeric carbon. This has been shown [22] to increase the mechanical and electrical properties of the graphite part which is the desired result. During the laser sintering process, phenolic resin melts to bond the graphite particles together. Subjected to high temperatures, phenolic resin undergoes thermal decomposition and re-orientation to form polymeric carbon which forms stronger bonds with the graphite matrix yielding a mechanically stronger part with a homogeneous carbon composition [52].

Previous research on the effects of thermal treatment on phenolic resin [53] has shown that the heat treatment temperature significantly affects the mechanical strength of the carbonized phenolic resin. It is apparent from Figure 3.5 [53] that there is a decrease in flexural strength as curing temperatures increase from 200 ºC to around 500 ºC and then reaches a maximum as the temperature reaches 800 ºC.

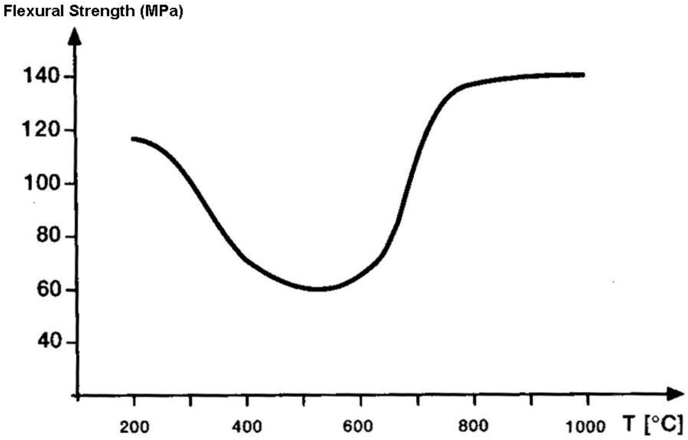

Figure 3.5 Relationship between flexural strength and curing temperature for phenolic resins [53].

It has been postulated that the decrease in flexural strength arises from increased evolution of gaseous products such as hydrogen and carbon dioxide at curing temperatures between 200 ºC and 500 ºC [54] which affect the mechanical strength due to increased porosity. Based on this experimental evidence, the graphite parts were subjected to carbonization in a Yokogawa UP550 programmable high-temperature, vacuum furnace at temperatures above 800 ºC to maximize the strength of the brown parts. The furnace, which can heat up to a maximum temperature of 2000 ºC, uses several graphite heating elements along with a digital controller to precisely supply the required heat into the chamber to maintain uniform temperature. The furnace chamber can be vacuumed and backfilled with various inert gases for atmosphere controls throughout the programmed temperature profile. The carbonization was carried out in a vacuum of 0.01 Torr and research grade argon gas was used as the backfill gas to prevent oxidation of the carbonized phenolic resins during the carbonization process.

To minimize deformation caused by escaping gases during the burnout, a slow heating ramp between 200 and 600 ºC was selected. A slightly higher heating ramp was used from 600 ºC to 800 ºC. For parts heat treated at temperatures above 800 ºC, the heating ramp was increased until the required temperature was reached. Once the peak temperature was reached, the temperature was held constant for 1 hour upon which the part is left to cool to room temperature naturally. A temperature profile for heat treatment at 800 ºC is shown in Figure 3.6. The profile starts at room temperature and heats up to 200 ºC with a heating ramp rate of 60 ºC/hour, followed by a slower ramp rate of 30 ºC/hour to 600 ºC, and then a 50 ºC/hour ramp rate cures the part to 800 ºC. The dwelling time at the peak temperature was 1 hour.

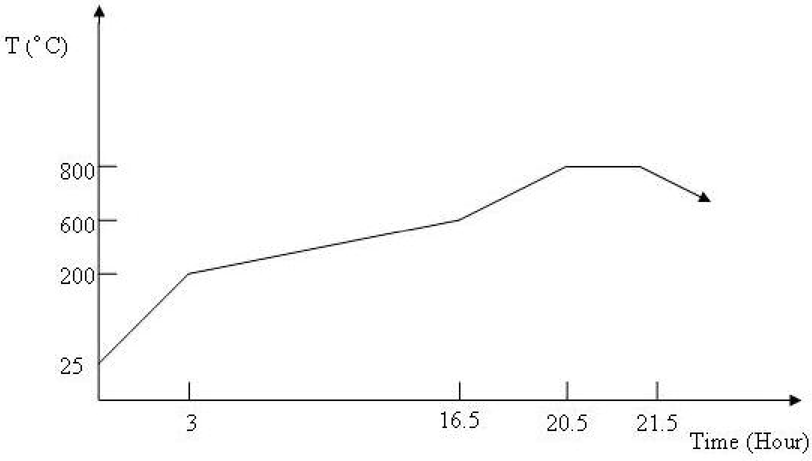

Figure 3.6 Temperature profile for brown part formation.

3.2.4 INFILTRATION

The burnout of the phenolic binder in a vacuum furnace yields a brown part that comprised of the graphite powder bonded by carbon residue from the binder itself. This formed a porous skeletal structure of the final bipolar plate geometry. Even though there was a significant shrinkage of the plate during the carbonization process, the part was still extremely porous and possessed high fluid permeability. This rendered the plate unusable in a fuel cell and therefore was subjected to various infiltration processes to achieve densification and hence fluid impermeability.

Cubes of 15 mm by 15 mm by 15 mm produced by laser sintering were used for porosity measurements. A Quantachrome Corporation Ultrapycnometer-1000 helium pycnometer was used to measure the specific weight and actual volume of the specimens. This technique uses Archimedes' principle of fluid displacement as well as ideal gas law to accurately determine the volume of a test specimen [55]. The test begins with expanding a quantity of helium gas at known pressure into an empty sample cell to establish a baseline. The test specimen is then loaded into the sample cell and the cell is resealed. The same amount of helium gas at the same pressure is again expanded into the sample cell with the test specimen in it, and the new equilibrium pressure is measured. The difference between these two pressures combined with the volume of the empty sample cell allows us to calculate the volume of test specimen using

$$V_s = V_c + \frac{V_h}{1 - {P_1}/{P_2}} \tag{3.1}$$

where V_s is the volume of test specimen, V_c is the sealed sample cell volume, V_h is the added volume of helium gas, P_1 is the known pressure and P_2 is the new equilibrated pressure. Density of the test specimen can subsequently be calculated once the specimen weight is measured using an electronic balance. By measuring the apparent volume of the part and using the actual volume measured by the pycnometer, the porosity of the specimens can be estimated using equation 3.2.

$$P(\%) = 1 - \frac{V_{act}}{V_{app}} \tag{3.2}$$

where P is the percentage porosity of the sample, V_{act} is the actual volume of the part as measured by the pycnometer and V_{app} is the apparent volume of the part obtained in this case by measuring the sides of the cube. The specific weight, actually volume and percentage porosity where measured at each step of the process; for the green part, brown part and the infiltrated part. The following sections discuss the various infiltration experiments performed to produce fluid impermeable, electrically conductive graphite parts.

3.2.4.1 CONDUCTIVE EPOXY

The chemical stability, mechanical strength and wetting characteristics of epoxy resin make it a suitable candidate for use as an infiltrant. Success of infiltration is primarily governed by the wetting characteristics of liquid and solid materials involved. Young proposed the following relationship [56] between the contact angle θ and the interfacial tension γ at the three phase contact point of a liquid on a solid surface. The subscripts represent the respective phase liquid, solid and vapor.

$$\gamma_{SV} = \gamma_{SL} + \gamma_{LV} cos\theta \tag{3.3}$$

where, γ_{SV} , γ_{SL} and γ_{LV} are the surface free energies between solid-vapor, solid-liquid and liquid-vapor phase, respectively and θ is the contact angle between the solid and liquid. For spontaneous wetting to occur, it is desirable that the liquid-vapor interface energy is less than the solid-vapor interface energy (i.e., $\gamma_{infiltrant} < \gamma_{substrate}$). Table 3.3 lists the surface energies of common infiltrants and substrates at room temperature. It is apparent that spontaneous infiltration of epoxy resin into the graphite substrate will take place. In an effort to improve the conductivity of the brown part by the infiltration process, an electrically conductive epoxy resin was procured from Epoxies Etc. The resin was a single component polymer system infused with silver nanoparticles for increased electrical conductivity sold by Epoxies Etc. as 40-3920.It had a viscosity of 9000 cps at 25 ºC, an electrical conductivity of 5000 S/cm and an operating temperature range of 20 ºC to 140 ºC.

Table 3.3 Surface energies of infiltrants and substrates adapted from [2].

Material	**Surface Energy (dynes/cm=10^{-3} J/m^2)**
Silicone Oil	21
Ethyl Cyanoacrylate	~34
Liquid Epoxy Resin	47
Graphite	~70
Water	73
Mercury	470
Solid Aluminum	~500

An estimate of the time required for complete infiltration can be obtained by using the Washburn equation (3.4) which describes the motion of a liquid front rising in a bundle of parallel capillaries.

$$h^2 = \frac{\gamma D t cos\theta}{4\eta} \tag{3.4}$$

where t is the time taken for a liquid of viscosity η and surface energy γ to rise to a height h into a capillary of diameter D. Therefore, the time taken for the conductive epoxy to completely infiltrate an indirect LS graphite part of thickness 0.5 cm with an estimated pore diameter of 70 μm and a contact angle of 70º with conductive epoxy of 9000 cps can be obtained by rearranging and solving equation 3.4:

$$t = \frac{4\eta h^2}{\gamma D cos\theta} \tag{3.5}$$

$$\boldsymbol{t} = \frac{\left(4\times 90\frac{\boldsymbol{g}}{\boldsymbol{cm.s}}\right)(0.5\ \boldsymbol{cm})^2}{\left(47\frac{\boldsymbol{g}}{\boldsymbol{s}^2}\right)\left(70\times 10^{-4}\ \boldsymbol{cm}\right)\cos 70}$$

t = 799.82 s = 13.33 mins

The infiltration was performed by placing the porous graphite part in a dish containing the conductive epoxy resin. Due to the highly viscous nature of the resin, infiltration was observed to take significantly longer than the estimated time and hence required the thinning of the epoxy using solvents such as methoxy propanol acetate and xylene. The epoxy resin and thinner were mixed in a 1:1 ratio and the diluted epoxy was then used to infiltrate the porous parts. Once complete infiltration was complete which was determined by the cessation of bubbles from within the brown part, the resin was allowed to cure according to the recommended curing schedule of 30 minutes at room temperature.

3.2.4.2 ELECTROLESS NICKEL DEPOSITION

Nickel metal was deposited onto the plate with the aim of infiltration of metal into the porous structure thereby increasing the conductivity of the plate. The electroless reduction was performed by placing indirect LSed graphite bars (brown parts) activated at 400 ºC, into a bath composed of nickel sulfate (source), sodium citrate (complexing agent), ammonium sulfate (buffering agent) and sodium hypophosphite (reducing agent) [57], held at a temperature of 85 ºC. After stirring for an hour, the nickel plated samples were washed in distilled water, dried in an oven at 90 ºC and characterized using Scanning Electron Microscopy (SEM) and Energy Dispersive Spectroscopy (EDS).

3.2.4.3 ELECTRICALLY CONDUCTIVE POLYMERS

Due to the corrosive nature of the fuel cell environment, bipolar plates made from metals and their alloys are highly susceptible to pitting and other modes of failure caused by corrosion. Research into the corrosion resistance of stainless steel plates has shown improved resistance by using polymeric materials that possess high electrical conductivities. Conducting polymers such as polypyrrole, polyaniline and polythiophene have been reported to show high values of conductivity [58, 59] and [60] as well as chemical/thermal stability [61] in the operating conditions of a DMFC. The objective of the experiments was to synthesize the polymers in situ by chemical synthesis and electropolymerization.

3.2.4.3.1 CHEMICAL SYNTHESIS

Conductivity and porosity specimens (brown parts) were soaked in a bath of aniline monomer in 1M dopant acidic solution (for conductivity) overnight so as to achieve complete infiltration. While maintaining the bath at 0 ºC, an oxidizing agent such as ammonium persulfate was then slowly added to the bath to initiate polymerization. Upon oxidation, polyaniline separates from the solution and was found to coat the specimens in the solution. The samples were then removed from the solution, dried in an oven at 100 ºC and then tested for both porosity and conductivity. The aim of the experiment was to polymerize the monomer present within the porous matrix thereby tackling both issues of conductivity and porosity in one step.

3.2.4.3.2 ELECTROCHEMICAL POLYMERIZATION

In this technique, a porous graphite specimen (brown part) was used as the anode in a solution containing the required monomer, suitable solvent (0.5M H_2SO_4 as electrolyte) and a doping salt, with a platinum counter electrode. By maintaining a current density of 250 - 500 mA/cm^2 for times ranging from 1 to 8 hours, electrochemical deposition of polyaniline layers occurred on the porous graphite anode. By initially soaking the graphite plate in the monomer solution, it was hoped to initiate polymerization of the conductive polymer (polyaniline, polythiophene) within the pores.

3.2.4.4 ETHYL CYANOACRYLATE

Cyanoacrylate (ethyl-2-cyanoacrylate) is a colorless liquid with low viscosity and is the main component of cyanoacrylate glue. It is soluble in methyl ethyl ketone, toluene, acetone, N,N-dimethylformamide and nitromethane. It was selected due to its availability in low viscosities (< 10 cps) to facilitate complete infiltration of the preforms. It possesses a large operating temperature range (-54 ºC to 121 ºC) and is stable in methanol. It is usually prepared by the condensation of ethyl cyanoacetate with formaldehyde followed by thermal cracking to obtain the reactive monomer [62]. The chemical reaction is as follows:

$$CH_2(CN)CO_2C_2H_5 + CH_2O \rightarrow CH_2{=}C(CN)CO_2C_2H_5 + H_2O$$

The ethyl cyanoacrylate monomer undergoes rapid anionic polymerization as shown in Figure 3.7 in the presence of a weak base such as water and forms a solid within a few seconds of starting to cure and achieves full bond strength in 24 hours [62]. Ambient humidity is sufficient to initiate this curing process and the rapidness of the reaction can therefore be controlled by controlling the humidity (Figure 3.8) and also by using stabilizers (weak acids) that lengthen the curing time.

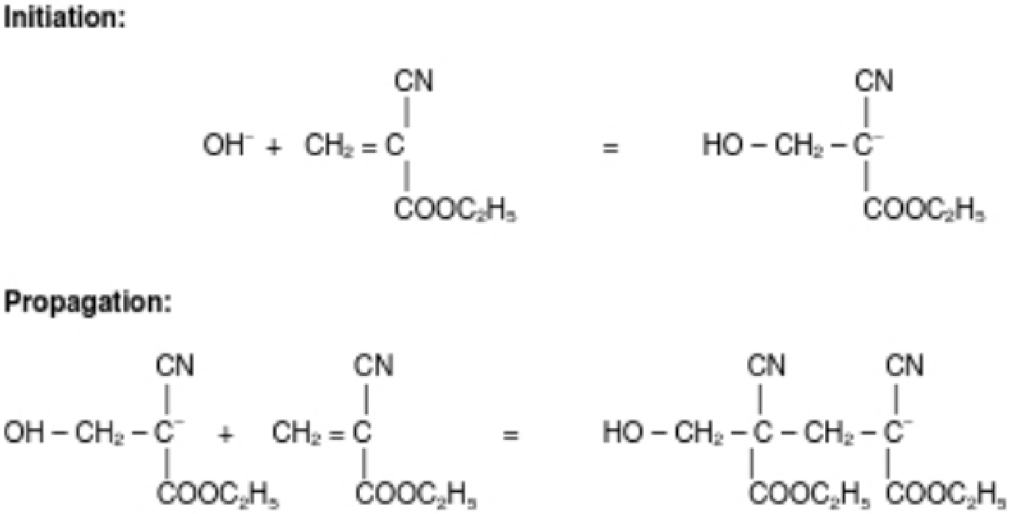

Figure 3.7 Polymerisation of cyanoacrylate adhesive [62].

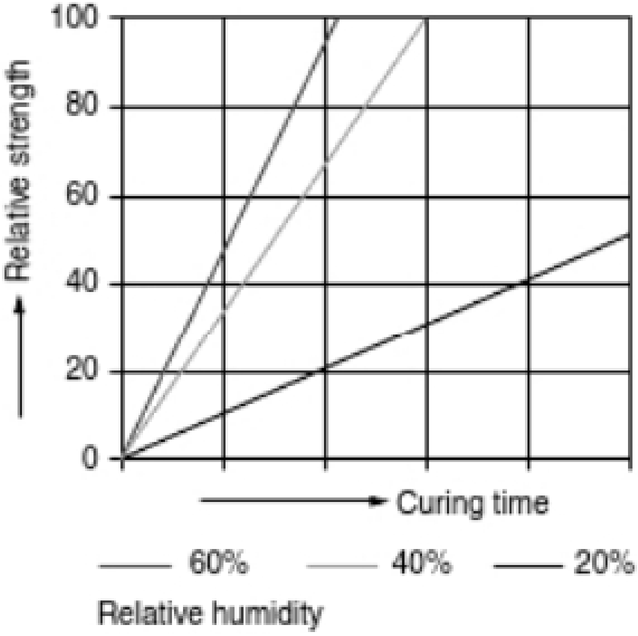

Figure 3.8 Relation between curing time of cyanoacrylate and relative humidity [62].

Low viscosity cyanoacrylate sold by Prairie Technologies Inc. was infiltrated into porous specimens using a setup that applied a low-quality vacuum on one side of the bipolar plate while the infiltrant was manually dripped onto the other side so as to ensure that the cyanoacrylate penetrated the full thickness of the part. The samples thus infiltrated were allowed to dry overnight and the sample surfaces were polished to remove excess cyanoacrylate to restore the electrical properties of the graphite matrix. Using the Washburn equation (3.3), the time taken for complete infiltration using ethyl cyanoacrylate can be estimated to be:

$$t = \frac{\left(4 \times 0.1 \frac{g}{cm.s}\right)(0.5\,cm)^2}{\left(34 \frac{g}{s^2}\right)\left(70 \times 10^{-4}\,cm\right)\cos 70}$$

$$t = 1.22\,s$$

The time observed was slightly larger than the estimated time due to the fact that the porosity of the plate is more tortuous than the simplified assumption of parallel capillary tubes and that the rapid curing of the cyanoacrylate within the matrix impedes the flow of the polymer through the plate.

3.3 FINISHING

When infiltrated with electrically insulating polymers such as epoxy resin and ethyl cyanoacrylate, the polymers coat the external surfaces of the part thereby significantly increasing the contact resistance of the part. The effect of increasing contact resistance on the ohmic losses in a fuel cell are well known and have been attributed to be a major cause for poor fuel cell performance [63]. Also, the as-produced brown parts possess inherent surface roughness that contributes to the contact resistance as well as detrimentally affecting the sealing of the cell [64]. This was prevented by grinding the surfaces of the infiltrated parts on a Struers grinding wheel with a 240 grit grinding pad using water as the grinding medium until all the polymer residue was removed and there was no visible gap when placing the anode and cathode plates together. Studies have shown that there is a direct relationship between the grit size of sandpaper used and the contact resistance between plates in a fuel cell [64].

3.4 MATERIALS PROPERTY CHARACTERIZATION

Tests were conducted throughout the process of fabricating graphite bipolar plates to verify that the values listed for the properties in Table 3.1 were attained. The following sections discuss the various tests conducted to characterize the properties of the laser sintered bipolar plates.

3.4.1 ELECTRICAL CONDUCTIVITY

One of the primary functions of bipolar plates is to collect the electrons generated in the fuel cell and guide them to the external circuit. Electrical conductivity is therefore one of the more important plate properties as it has a direct impact on the ohmic losses and thereby the performance of the fuel cell. The more electrically conductive the bipolar plates, the less the contact resistance and consequently the lower the ohmic losses during operation. The target for electrical conductivity set by the Department of Energy for bipolar plate materials is 100 S/cm.

Electrical conductivity measurements were made with green, brown and infiltrated parts using a four point probe test method. The advantage of using a four point probe test method is that unlike a two point probe, the contact resistance between the probe tips and the sample is eliminated and more accurate measurements can be easily made. Figure 3.9 shows a schematic representation of the four point probe setup that was used. The setup consists of four probes that make contact with the sample surface. The two outer probes supply a known current while the voltage drop, due to the resistivity of the sample, across a known distance is measured by the two inner probes. The testing was performed according to ASTM C611 specifications and consisted of a Keithley 224 Programmable Current Source, a Hewlett Packard 3456A Digital Voltmeter and a Cascade Microtech Alessi four point probe test mount.

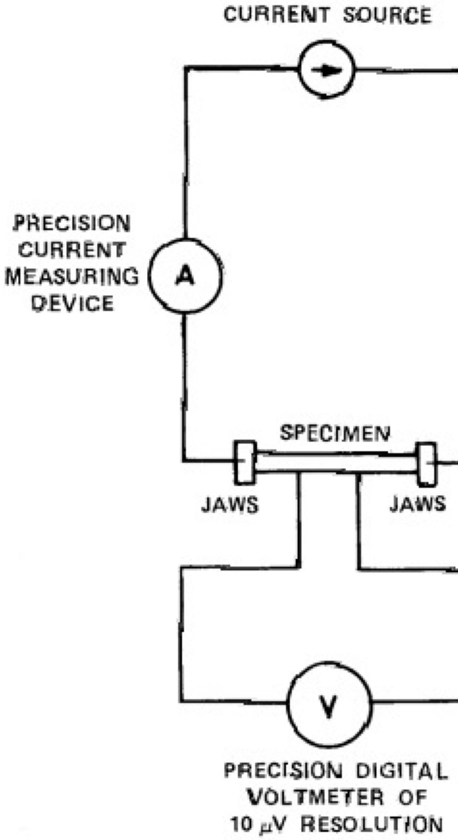

Figure 3.9 Setup to measure electrical conductivity using four point probe method [65].

Two types of samples were made for measuring the electrical conductivity. The first type was rectangular bars of 40 mm by 5 mm by 5 mm, which were used purely for conductivity measurements. The second type consisted of flexural strength test bars 125 mm long, 12.7 mm wide and 3.2 mm thick which were characterized for electrical conductivity at all process stages before they were fracture tested for flexural strength. Electrical conductivity is a measure of the materials ability to conduct charge through it and is given by equation 3.6 as:

$$\sigma(S/cm) = \frac{I(mA).L(cm)}{V(mV).A(cm^2)} \tag{3.6}$$

where σ is the electrical conductivity in S/cm, I is the constant current applied in mA, L the distance over which the voltage drop is measured (probe tip spacing) in cm, V the voltage drop measured in mV and A the cross sectional area of the sample in cm^2.

3.4.2 MECHANICAL STRENGTH

Bipolar plates in a fuel cell are subjected to compression as part of the operation environment. The performance of a fuel cell is related to the compressive loads in that, an increase in the clamping pressure increases the contact surface area thereby reducing the contact resistance [66] and consequently improving performance while also helping with the sealing of the cell to minimize leakage of fuel. However, too much pressure can also result in an obstruction of mass transport within the cell, detrimentally affecting performance. Since bipolar plates are normally stacked up by clamping forces in a fuel cell stack, their ability to resist deformation and maintain structural integrity is important.

Flexural strength is therefore used as the primary parameter by which to evaluate mechanical suitability of bipolar plates in a stack.

The flexural strength also known as the bend strength is commonly measured using a transverse bending or three point bend test as shown in Figure 3.10. It is obtained when the ultimate flexibility of the material is achieved, often before its proportional limit. ASTM D790, which is often used for composite materials was selected to test the indirect LS bipolar plates made of graphite, carbon residue and polymer infiltrant. The test involved placing a sample over two points and applying a load at the midpoint of the specimen.

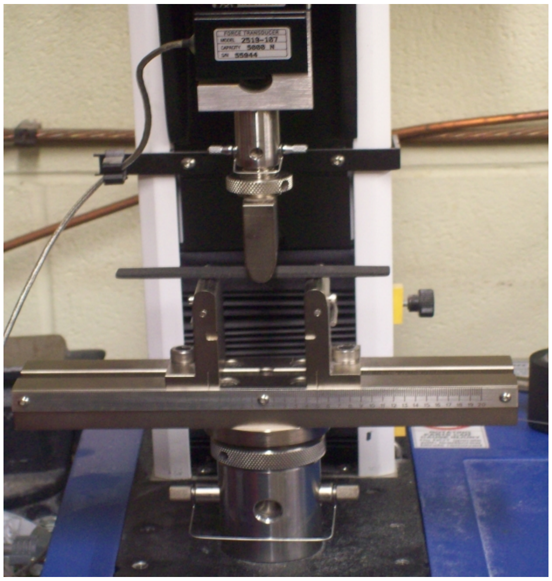

Figure 3.10 Three point bend test setup for measuring flexural strength.

An Instron 3345 MTS machine, shown in Figure 3.10, was used to perform the testing using indirect LS test specimens with dimensions of 125 mm × 12.7 mm × 3.2 mm. The average flexural strength σ_{flex} was obtained using equation 3.7:

$$\sigma_{flex} = \frac{3FL}{2bt^2} \tag{3.7}$$

where F is the applied load at yield, L is the span length between two supports, b is the width of the specimen and t is the thickness of the specimen.

3.4.3 THERMAL CONDUCTIVITY

Thermal management in a DMFC is an important issue as the effect of temperature on the performance of a fuel cell has been shown to be significant [67]. Increasing the temperature of the cell improves the electrodes' kinetics [68] which in turn improves mass transport and therefore performance. However, increasing the cell temperature also increases the amount of water permeation by electro-osmosis which then affects the transport properties of both the cathode catalyst and the diffusion layer [69]. Improper thermal management therefore increases uneven temperature distribution in a stack which can dramatically affects overall performance and life of the stack.

The thermal conductivity of the laser sintered bipolar plates was measured using a TPS 500 Thermal Constants Analyzer to determine whether the DOE target of 10 $Wm^{-1}K^{-1}$ for bipolar plate thermal conductivity was achieved.

3.5 CARBON FIBER ADDITION

Critical considerations for LS graphite bipolar plates are the strength of the parts in the green, brown and finished states as well as the final part electrical conductivity. US Department of Energy target values for bipolar plate flexural strength and conductivity are 4.1 MPa and 100 S/cm, respectively [28]. LS finished bipolar plates possess flexural strength in the range of 12-40 MPa, but green parts are particularly weak, 1-2 MPa, which complicates handling during processing [70]. Electrical conductivity of

LS bipolar plates is 200-400 S/cm [22, 71]. Carbon fiber (CF) additions are known to improve the strength and conductivity of polymer matrices [72]. The effect of CF addition on the strength and electrical resistivity of green, brown and finished bipolar plates was assessed. The following sections describe research performed in collaboration with researchers at the Center for Aerospace Manufacturing Technologies, Department of Mechanical and Aerospace Engineering, Missouri University of Science and Technology, Rolla MO, USA [73].

3.5.1 MATERIALS AND POWDER MIXING

Carbon fiber was purchased from Asbury Graphite Mills, Inc., and AGM99 from Advanced Laser Materials, Belton TX. All carbon fiber was 7-8 µm in diameter and 70-150 µm in length. Brown parts were infiltrated with liquid epoxy, EPONtm Resin 828.

For natural graphite, phenolic and carbon fiber, density varies between 1.5-2 g/cm^3 and is considered to be identical, resulting in equivalence of weight and volume fraction. For all mixtures, the fraction of phenolic was held at 30-35%, and the relative amounts of graphite and CF were varied. The composition of each mixture is reported based on the overall, global fraction of CF in the starting powder mixture. The fraction of CF varied between 0 and 26%.

3.5.2 LASER SINTERING AND POST-PROCESSING

Powder mixtures were laser sintered using a 3D Systems, Inc. Sinterstation® 2000. The fill power was 10-20 W, outline laser power was 4 W, scan speed was 1.53 m/s, scan spacing was 76.2 µm and layer thickness was 102 µm. Part and feed cylinder temperatures were held at 60-65 ºC and 40-47 ºC, respectively. Part configuration was consistent with necessary geometry for three-point bend testing, electrical conductivity measurement and bipolar plate production.

After LS, the green parts were carefully removed from the Sinterstation® part feed cylinder. Selected samples were post-processed by heating in a furnace (vacuum or argon) to convert the phenolic binder to carbon. The effect of phenolic dissociation temperature on brown part strength and electrical conductivity was assessed for dissociation temperatures between 400 ºC and 1200 ºC. The phenolic dissociation thermal cycle was: heat from room temperature to 200 ºC at 60 ºC/hr, heat to 600 ºC at 30 ºC/hr, heat to the hold temperature at 50 ºC/hr, hold one hour and furnace cool.

Finished parts were produced from green parts heated to 1000 ºC after laser sintering. They were immersed in liquid epoxy, held 20 min and removed. Following infiltration, the parts were oven cured for 1 hr at 80 ºC.

3.5.3 PART CHARACTERIZATION

Microstructure of brown parts was studied using a Hitachi S-4700 FE-SEM. Flexural strength was assessed using three-point bend testing (ASTM D790). An Instron Model 3345 tester was used for green and brown part testing, and an Instron 4468 tester was used to mechanically evaluate the finished parts. Specimen size was 125 mm long, 12.7 mm wide and 3.2 mm thick.

Electrical conductivity was measured using four-probe testing according to ASTM C611. A Cascade Microtech unit with a probe spacing of 1.016 mm was used to evaluate the brown parts, and a Keithley 2400 SourceMeter was used for finished part testing. Specimen size was 3 mm by 3 mm by 20 mm.

3.6 LASER SINTERED GRAPHITE BIPOLAR PLATES

Using the process described in the previous sections, bipolar plates were made by laser sintering and were tested to evaluate their performance against commercially purchased standard bipolar plates. The following sections discuss the various plates built for initial verification of the process and those built with the aim of improving fuel cell performance. All the laser sintered plates tested in the DMFC test station were brown parts that were with ethyl cyanoacrylate.

3.6.1 PROCESS VALIDATION

For purposes of validating the laser sintering process for making bipolar plates for prototype testing and comparison, three sets of bipolar plates (anode and cathode) with varying flow field patterns and active area of ~ 5 cm^2 were produced. Two of the sets were made with single serpentine flow fields (SSFF) of uniform width channels, making 9 passes and 11 passes, and a third single serpentine set of 11 passes with the channel width varying from 0.8 mm at the inlet to 2.1 mm at the outlet (Figures 3.11a, b and c). A fourth bipolar plate set with single serpentine, uniform width channels and active area of 5 cm^2, purchased from Fuel Cell Technologies Inc. was used for comparative studies. The three sets were tested in a Scribner Associates Inc. 850C PEM Fuel Cell Test Station with the following Membrane Electrode Assembly (MEA): Electrolyte Membrane: NaFion 117, Anode Catalyst: Pt/Ru/C, Cathode Catalyst: Pt/C, (2.5 mg/cm2 loading).

The electrochemical performances of the DMFC was evaluated with a single-cell fixture having an active area of 5 cm^2 and feeding a preheated 1 molar methanol solution into the anode at a flow rate of 2.5 mL/min by a peristaltic pump without back pressurization and humidified oxygen at 60 ºC into the cathode at a flow rate of 200 mL/min with a back pressure of 20 psi [74].

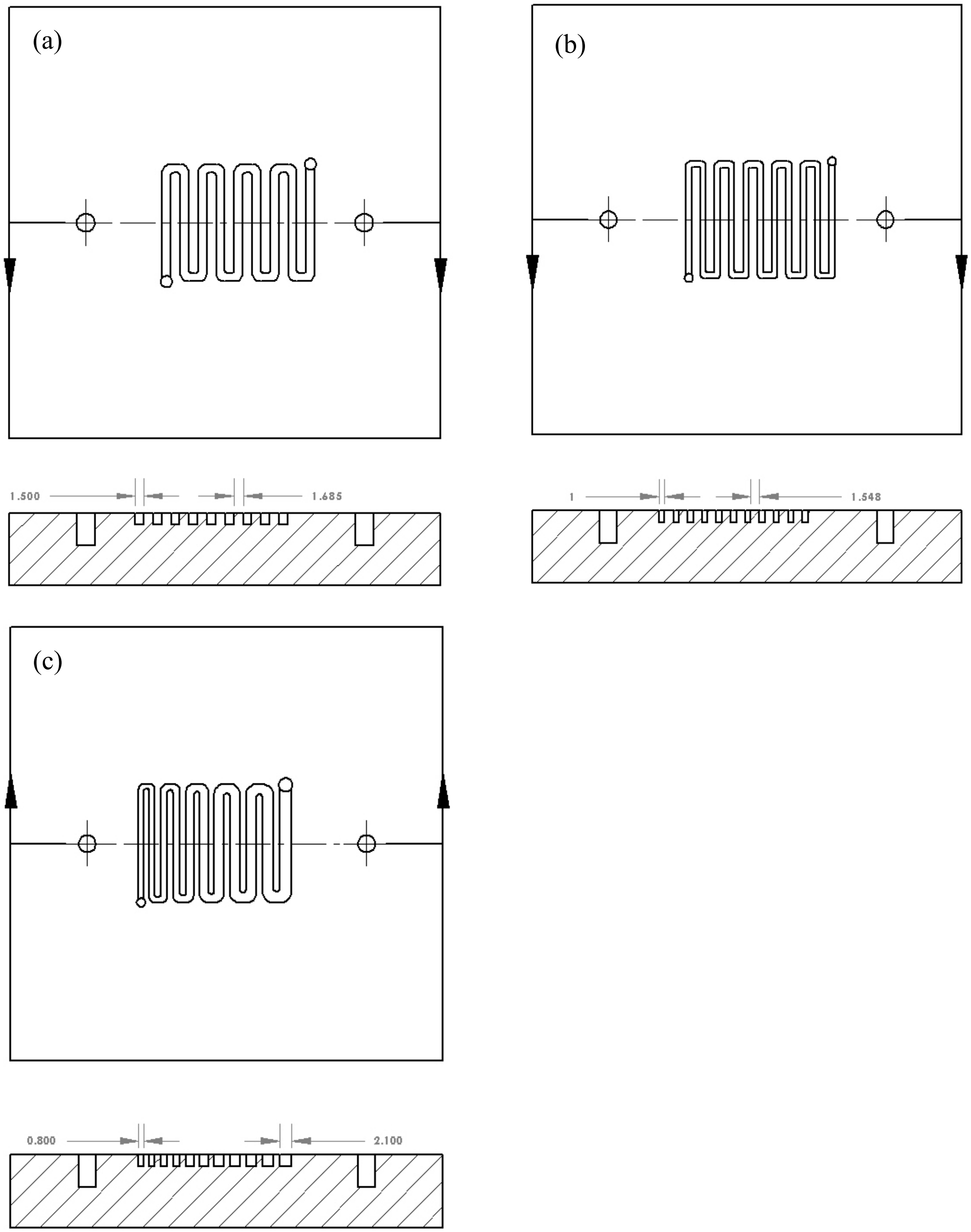

Figure 3.11 a) SSFF 9 passes uniform, b) SSFF 11 passes uniform, c) SSFF 11 passes variable

3.6.2 TESTING NOVEL BIPOLAR PLATE DESIGNS

To evaluate the ability of the laser sintering process to make bipolar plates that can be tested to yield repeatable results, a variety of plates with differing flow field designs were built and tested. The design of the bipolar plate flow field has a significant impact on the various factors that affect the performance of the DMFC such as pressure drop across the cell, fuel absorption in the catalyst layers and transport of CO_2 and water out of the cell to name a few. Studies in flow field design [75, 76, 77] have shown that the cross-sectional geometry of the channel, aspect ratio of the channels (ratio of channel width to rib width) and the flow field pattern (serpentine, corrugated, interdigitated etc) all affect the performance of the fuel cell.

The electrochemical performance of the DMFC was evaluated with a single-cell fixture having active areas of 5 cm^2 and 10 cm^{2}and feeding a preheated methanol solution into the anode at a flow rate of 2.5 mL/min by a peristaltic pump without back pressurization and humidified oxygen into the cathode at a flow rate of 200 mL/min at ambient pressure [74]. Three basic shapes, elliptical, triangular and rectangular (figure 4) were chosen as the cross-sectional geometries of the flow field channel for comparative purposes and are shown in Figure 3.12 a-i. The flow field area was chosen to be 5 cm^2 and two sets of the geometries were made differing in channel and rib widths and the number of passes (10 and 15) of the flow field channels. One additional set of plates with 10 cm^2 (13 passes) flow field area was made by scaling up the flow field area of the plates with 5 cm^2 flow field with 10 passes to validate consistency of results on scaling up. The channel and rib widths were kept constant and only the channel length and number of passes increased. All three sets of plates were subjected to post processing by heat treating at 1200 ºC, infiltrated to full density with cyanoacrylate and polished before being tested in a Scribner Associates Inc. 850e fuel cell test station with the following commercially purchased MEA: Electrolyte Membrane: NaFion 117, Anode Catalyst: Pt/Ru/C, Cathode Catalyst: Pt/C, (4 mg/cm^2 loading). The tests were performed by flowing 1 M methanol solution at a flow rate of 6 ml/min at the anode and humidified oxygen at a flow rate of 200 ml/min through the cathode of the DMFC single cell maintained at 65 ºC without backpressure at both anode and cathode. The performance of the plates made by indirect LS was compared to the performance of commercially purchased synthetic graphite plates with a rectangular cross-section and a serpentine flow field of 5 cm^2 making 15 passes with channel and rib lengths of 1 mm.

The plates with the triangular and elliptical cross section were also further evaluated by comparing their performance against the commercially purchased plates the concentration of the methanol solution, the flow rate of the methanol feed and the flow rate of the cathode side oxygen were varied.

3.6.2.1 MANIFOLDED BIPOLAR PLATES

To showcase the capability of the laser sintering process to build complex structures in a single step, a novel bipolar plate design with internal manifolding was built using indirect laser sintering and tested using the procedure and settings described in the sections 3.6.2. The plates as seen in Figure 3.13a, consists of four single serpentine flow fields that comprise the 25 cm^2 active area. As seen in the cross sectional view (Figure 3.13b), each of the four flow fields is fed by an individual inlet which drains into a common outlet at the center of the plate. The inlets and outlet could also be reversed to be a single inlet for each flow field and four separate outlets. This design would be difficult to build using conventional machining or molding methods and therefore highlights the advantages of using additive manufacturing techniques to rapidly fabricate and test prototypes.

Due to the internal structure of the manifolded plates and the asymmetry between the inlet and outlet, variation in performance was expected depending on orientation of the plates and also by swapping the inlet and outlet. Tests were performed to characterize the plates and compared against graphite plates procured from Fuel Cell Technologies Inc. with a triple serpentine flow field of 25 cm^2 active area. The plates were tested at anode flow rates differing from 3 ml/min to 14 ml/min and at vertical and horizontal orientation of the cell.

3.6.2.2 METHANOL CROSSOVER MEASUREMENTS

Methanol crossover is one of most critical issues that DMFC technology is faced with. The permeation of methanol through the polymer exchange membrane causes a significant reduction in the performance of the fuel cell because of a mixed potential at the cathode as well as poor fuel utilization. Although the phenomenon of methanol crossover is predominantly due to the fact that the membrane is permeable to methanol, consideration was given to plate designs with the aim of reducing the amount of methanol permeating through the membrane. Methanol crossover was evaluated by a voltammetric method [78] in which methanol solution was fed at a flow rate of 2.5 mL/min into the anode side of MEA while the cathode side was kept in an inert humidified N2 atmosphere. By applying a positive potential at the cathode side, the flux rate of permeating methanol was determined by measuring the steady-state limiting current density resulting from complete electro-oxidation at the membrane/Pt catalyst interface at the cathode side.

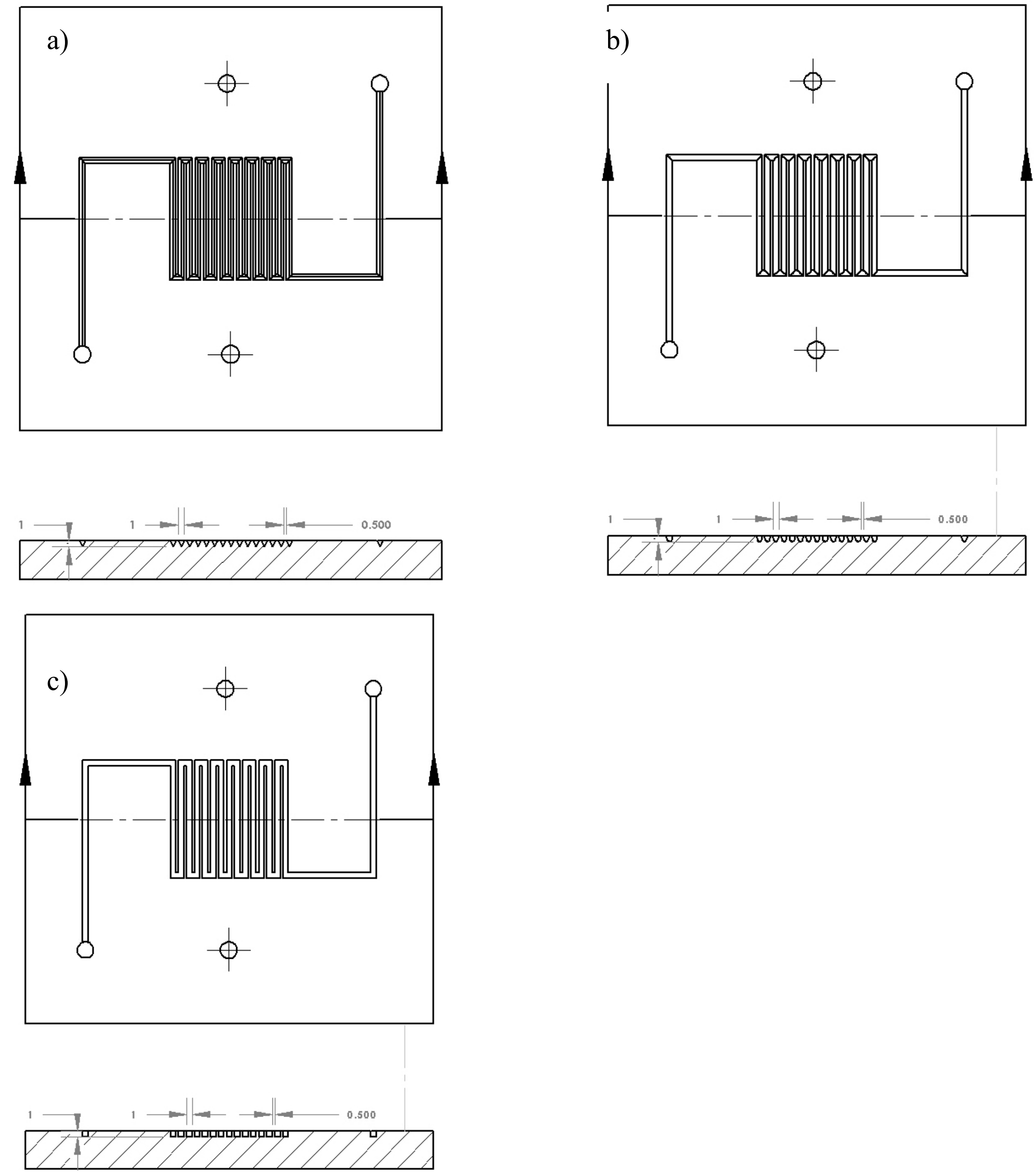

Figure 3.12 a) SSFF 5 cm^2, triangular cross section, 15 passes, b) SSFF 5 cm^2, elliptical cross section, 15 passes c) SSFF 5 cm^2, rectangular cross section, 15 passes.

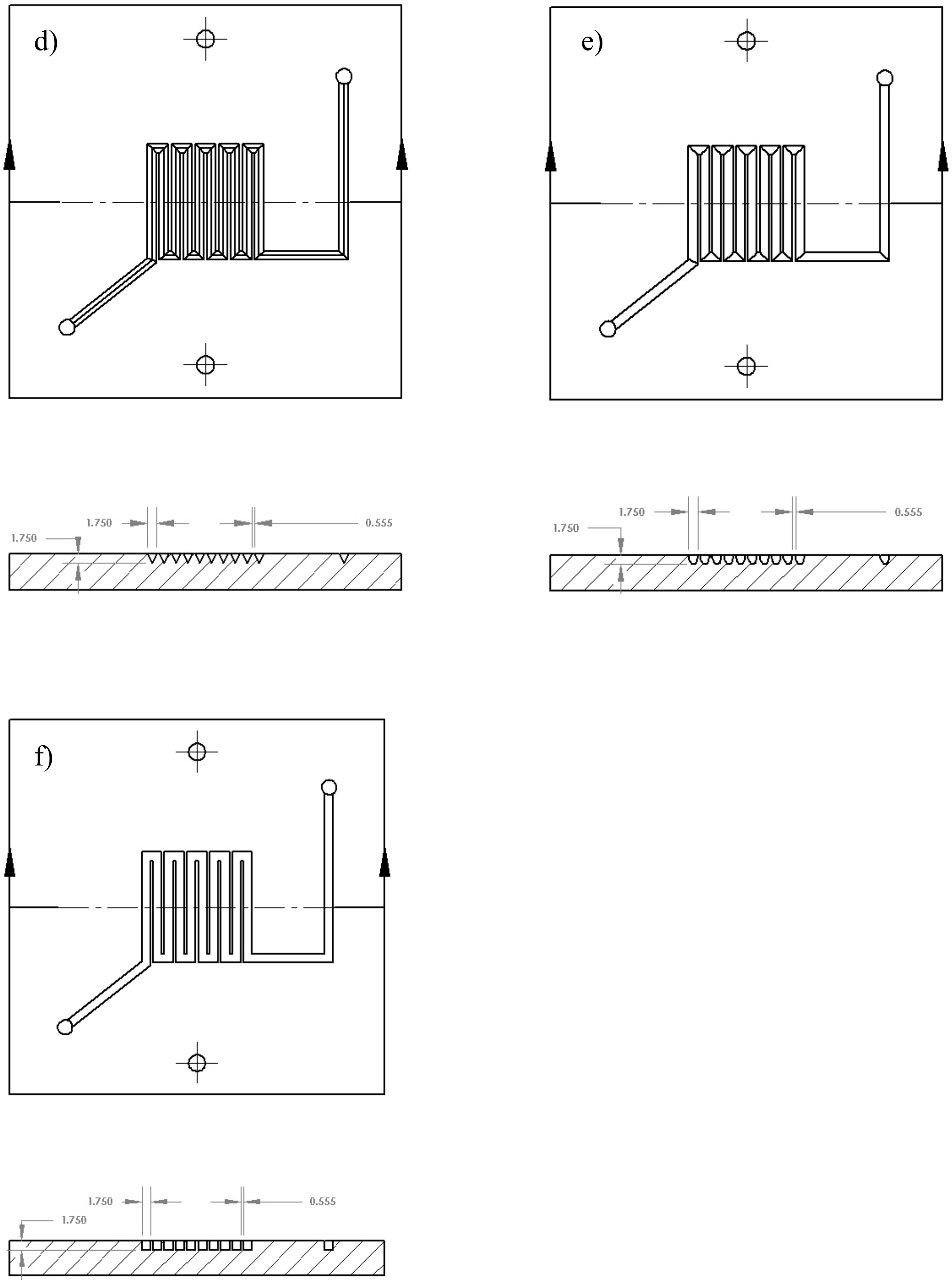

Figure 3.12 d) SSFF 5 cm^2, triangular cross section, 10 passes, e) SSFF 5 cm^2, elliptical cross section, 10 passes f) SSFF 5 cm^2, rectangular cross section, 10 passes.

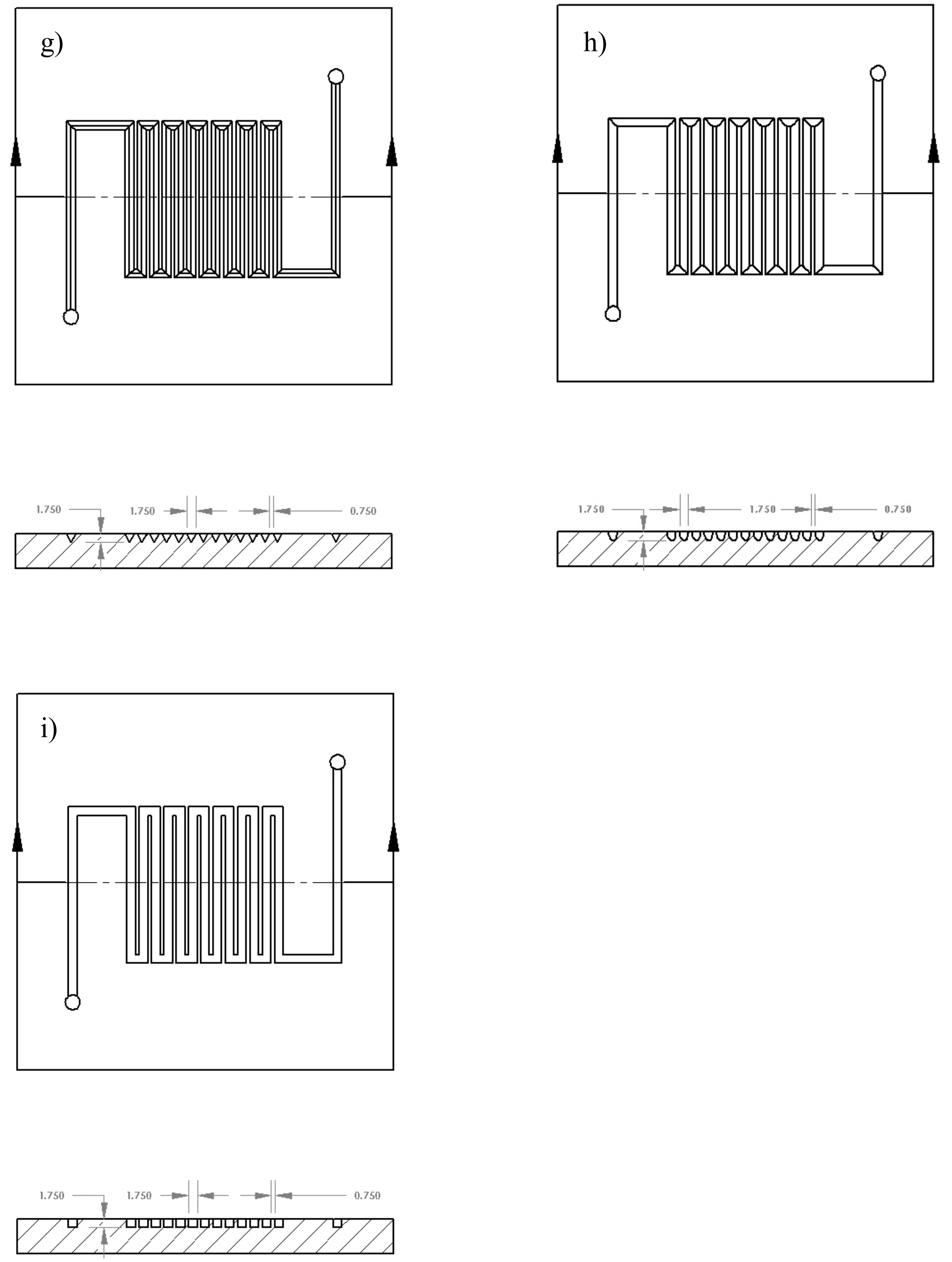

Figure 3.12 g) SSFF 10 cm^2, triangular cross section, 13 passes, h) SSFF 10 cm^2, elliptical cross section, 13 passes i) SSFF 10 cm^2, rectangular cross section, 13 passes.

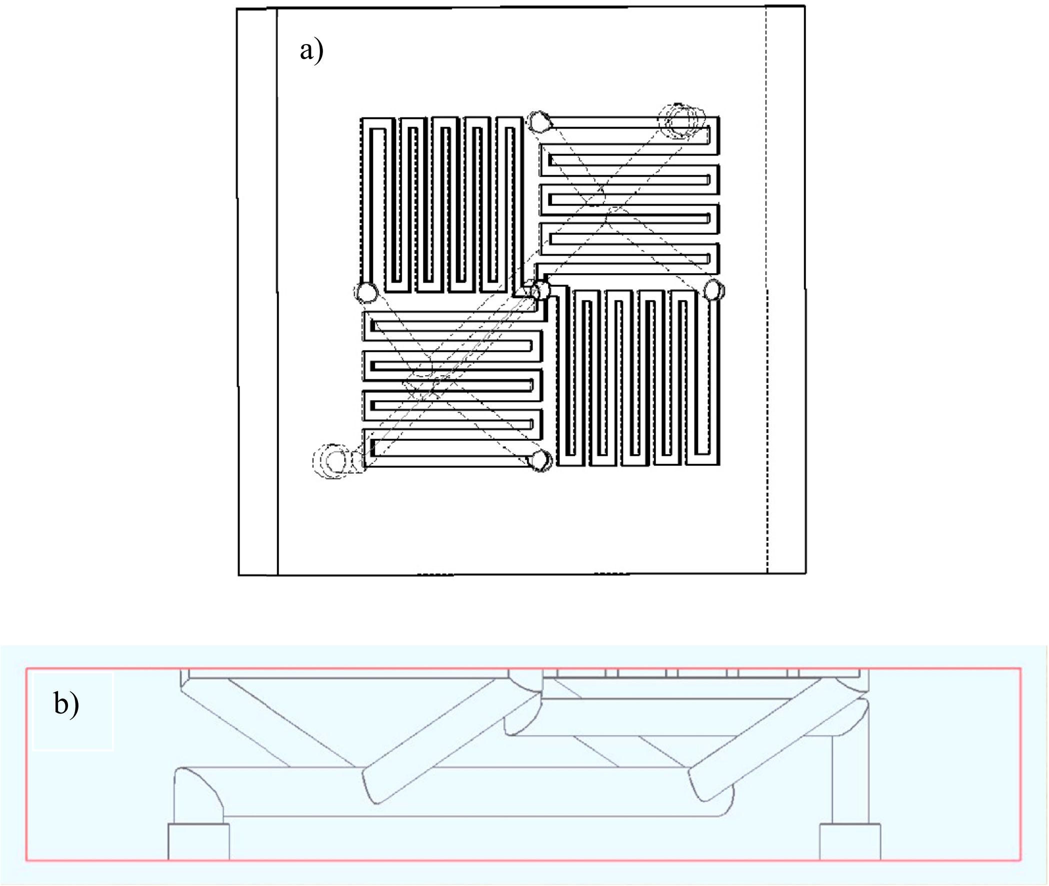

Figure 3.13 a) SSFF Manifolded plate, 25 cm^2, b) Cross sectional view of internal channels.

Chapter 4. Results

4.1 INTRODUCTION

In this chapter, the results of the experiments conducted to fabricate fully dense, electrically conductive graphite parts using indirect laser sintering described in the Chapter 3 are presented.

4.2 INFILTRATION

4.2.1 CONDUCTIVE EPOXY

Figure 4.1a shows the EDS linescan results for a graphite sample infiltrated with the silver filled epoxy resin. The plot shows the distribution of silver across the plate which indicates how far the epoxy has infiltrated into the plate. Figure 4.1b shows the SEM image of the interior of the infiltrated graphite sample with the EDS linescan superimposed.

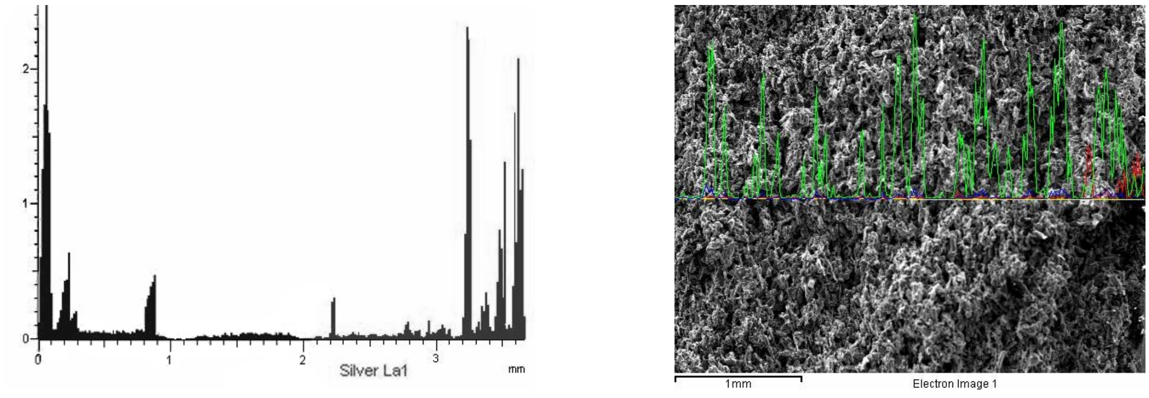

Figure 4.1 a) EDS linescan of silver epoxy infiltrated graphite sample, b) EDS linescan superimposed on graphite sample.

4.2.2 ELECTROLESS NICKEL DEPOSITION

As with the conductive epoxy experiment, the samples infiltrated with Ni metal were subjected to SEM and EDS analysis. As seen in the results shown in Figure 4.2 and Table 4.1, the amount of Ni deposited on the graphite sample (~0.05 wt %) was minimal compared to the amount of Ni required to fully coat the surface of the sample.

Table 4.1 EDS results of electroless Ni plating on external surface of graphite sample.

Element	Weight (%)	Atomic (%)
C	18.07	94.78
O	1.26	4.94
Na	0.03	0.07
Si	0.03	0.06
P	0.02	0.05
S	0.02	0.04
Ni	0.05	0.06

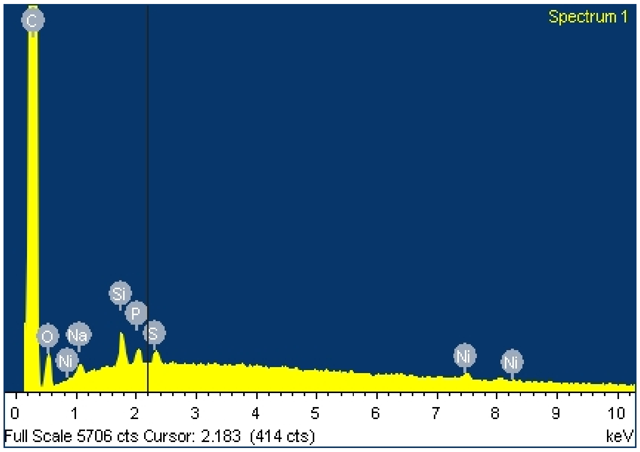

Figure 4.2 EDS spectrum of Ni plated graphite sample.

4.2.3 ELECTRICALLY CONDUCTIVE POLYMERS

Figures 4.3 a-g show the SEM images from the experiments on electropolymerization of polyaniline and polythiophene on the porous graphite samples. Figure 4.3a and b show the sample surface before and after deposition respectively and Figures 4.3 c and d shows the interior structure of the plate before and after deposition. It can be observed from Figures 4.3a and b that there is considerable deposition of polyaniline on the exterior surface of the samples. However, polymerization in the interior seems limited as seen in Figures 4.3 c and d as a result of the surface deposition which prevents access of fresh monomer to the internal pores.

Figures 4.3 e-g show the results of infiltrating the specimens with polythiophene. Figure 4.3 e and f show the exterior surface coating of polythiophene at different magnifications. Figure 4.3 g shows the interior of the graphite sample after deposition. It is apparent that the level of penetration of the polythiophene into the sample is similar to that in the polyaniline infiltrated specimen seen in Figure 4.3d.

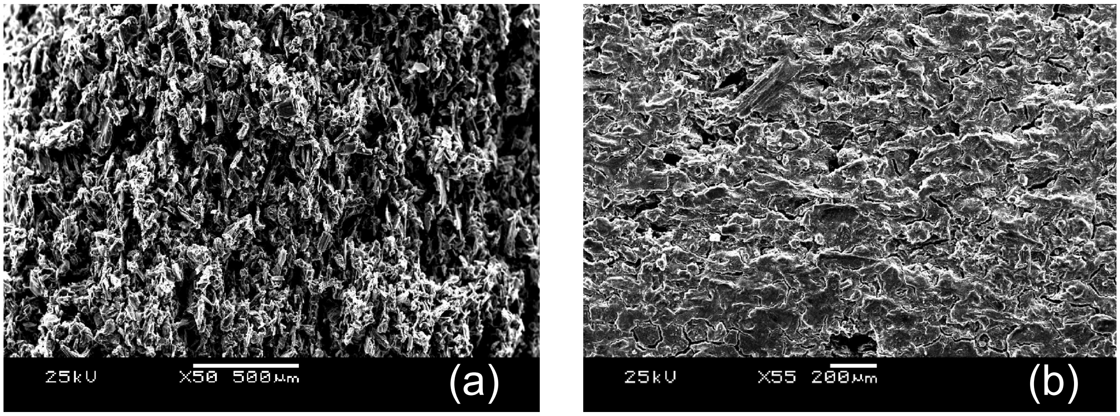

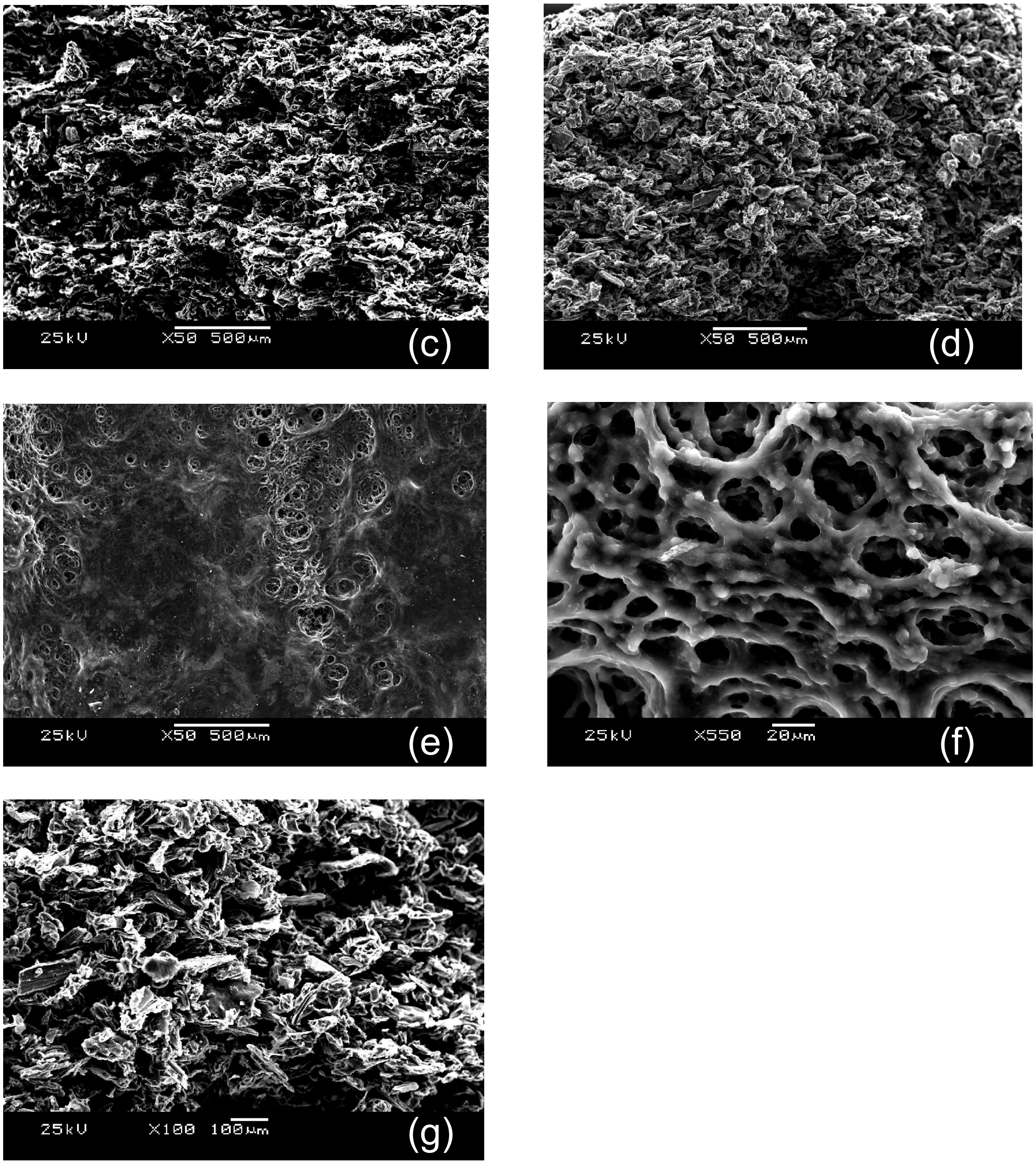

Figure 4.3 a) Uncoated exterior of graphite sample, b) Polyaniline coating on sample exterior, c) Interior of sample before deposition, d) Interior after deposition, e) Polythiophene coating on sample exterior, f) Higher magnification of polythiophene surface coating, g) Interior of sample after deposition of polythiophene.

4.2.4 ETHYL CYANOACRYLATE

From the pycnometric results shown in Table 4.2, the graphite infiltration samples made by indirect LS and described in Chapter 3.2.4 are 50% porous. Natural graphite has a theoretical density of 2.26 g/cm^3. Upon infiltrating a porous brown part with low-viscosity ethyl cyanoacrylate, the pycnometer measured volume (3.5709 cm^3) of the part was about 95 per cent of the apparent volume (3.6985 cm^3). SEM images Figure 4.4a and b show charging of the regions containing the infiltrated cyanoacrylate indicating complete penetration into the interior pore structure.

The bipolar plate before and after cyanoacrylate infiltration is shown in Figure 4.4c and d, respectively. The white discoloration seen on the plate in Figure 4.4d after infiltration is due to the blooming of the polymer and is easily removed by polishing the surface. Blooming may occur when a large amount of cyanoacrylate remains in liquid form. Some of the liquid material may vaporize and react with humidity. The result is a polymerization, which appears as a white dusty marking on the surface near the adhesive. Blooming can be reduced by improving ventilation to eliminate vapor or using an activator to polymerize at a faster rate. The negative effect when using an activator is that it slightly reduces the strength and adhesion of the adhesive bond.

Table 4.2 Pycnometer results measuring porosity of graphite infiltration samples.

Porosity Measurement												
	Green Part						Brown part					
Sample Number	Mass (g)	Apparent Volume (cm^3)	Pycnometric Volume (cm^3)	Pycnometric Density (g/ cm^3)	Open Porosity (%)	Closed Porosity (%)	Mass (g)	Apparent Volume (cm^3)	Pycnometric Volume (cm^3)	Pycnometric Density (g/ cm^3)	Open Porosity (%)	Closed Porosity (%)
1	3.101	4.190	1.850	1.677	41.432	25.819	2.570	3.347	1.165	2.206	63.661	2.372
2	3.240	4.243	1.913	1.694	41.149	25.062	2.696	3.442	1.374	1.962	52.173	13.168
3	3.206	4.241	1.818	1.763	44.568	21.982	2.677	3.379	1.198	2.235	63.836	1.115
4	3.287	4.439	2.007	1.638	39.697	27.540	2.735	3.583	1.225	2.233	65.016	1.208
5	3.310	4.416	2.020	1.638	39.328	27.509	2.753	3.340	1.265	2.177	59.859	3.673

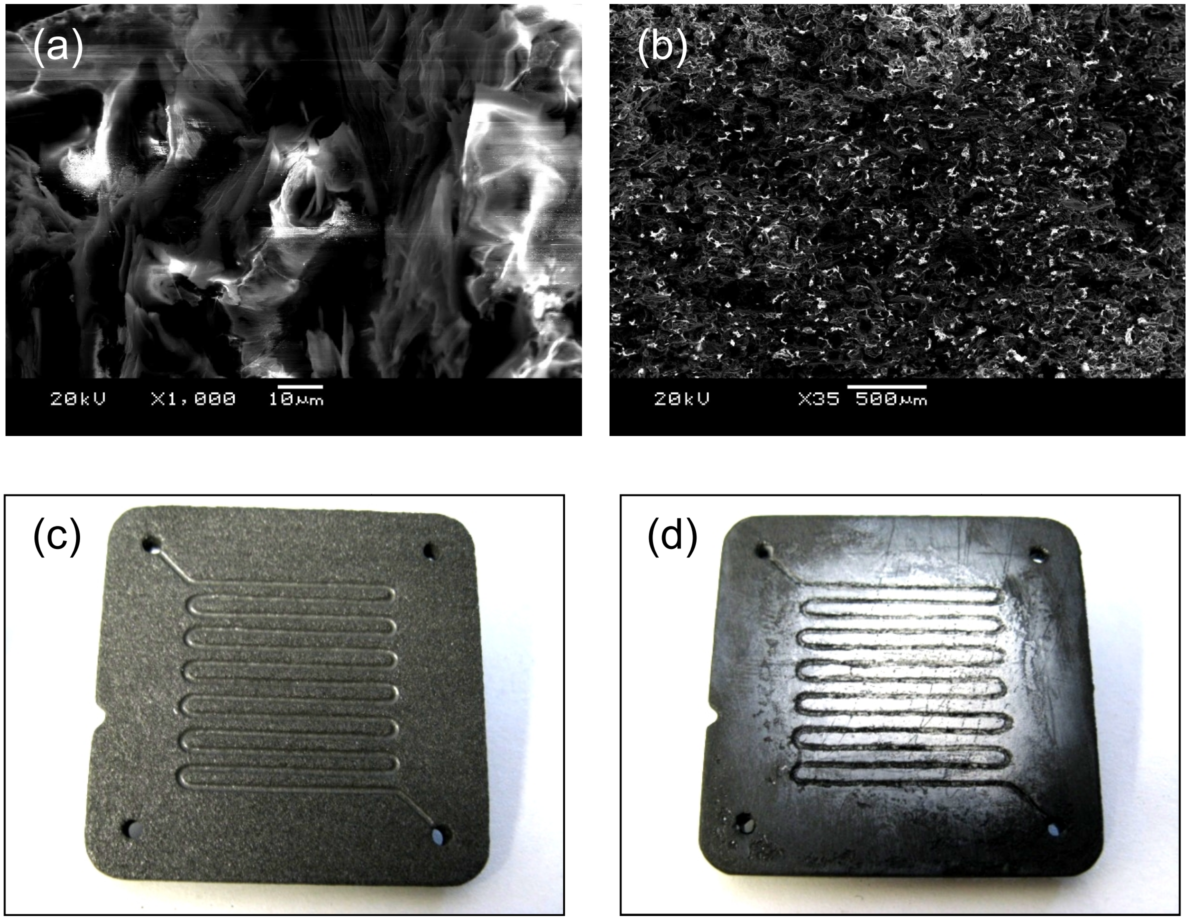

Figure 4.4 a) Charging observed under the SEM on the external surface of the cyanoacrylate infiltrated graphite samples, b) charging across the interior of cyanoacrylate infiltrated graphite plate, c) brown part before infiltration, d) cyanoacrylate infiltrated bipolar plate (with blooming).

4.3 FINISHING

The difference in the surface finish of the cyanoacrylate infiltrated bipolar plates before and polishing can be seen in Figures 4.5a and b. The rough surface texture of the brown parts along with regions of cured cyanoacrylate can be seen in Figure 4.5a. Figure

4.5b shows a polished bipolar plate which possesses a smooth finish and no cured polymer on the surface.

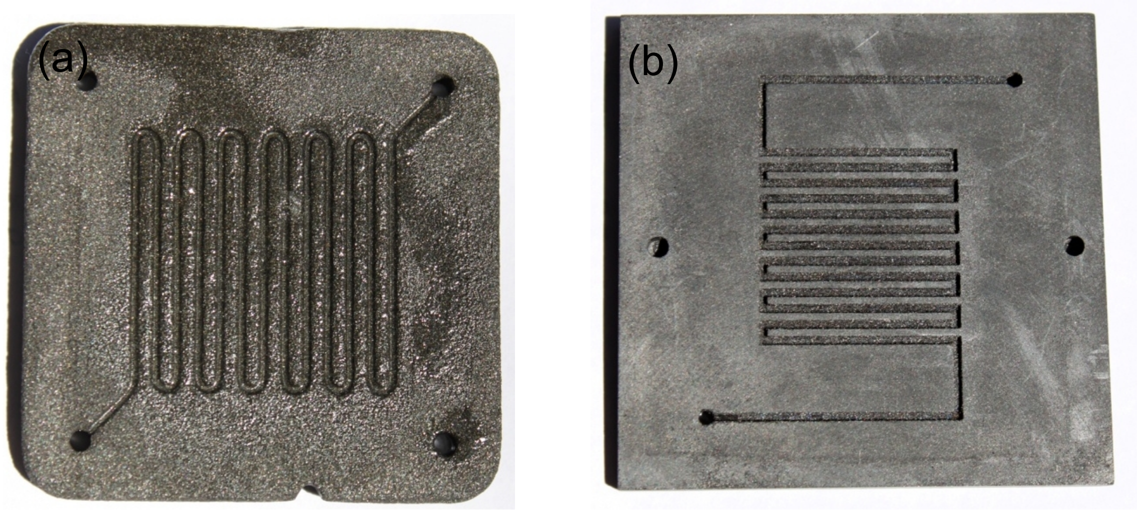

Figure 4.5 a) Infiltrated bipolar plate before polishing, b) Infiltrated graphite plate after polishing.

4.4 MATERIAL PROPERTY CHARACTERIZATION

4.4.1 ELECTRICAL CONDUCTIVITY

A set of the four point probe electrical conductivity measurements of the graphite parts is shown in Table 4.3. Figure 4.6 shows the graph plotted using the results shown in Table 4.3. It is apparent that the electrical conductivity of the graphite-phenolic brown parts is highly dependent on the temperature at which the phenolic resin binder is pyrolyzed. The target of 100 S/cm set by the D.O.E is achieved by carbonizing the green parts at temperatures greater than ~ 900 ºC.

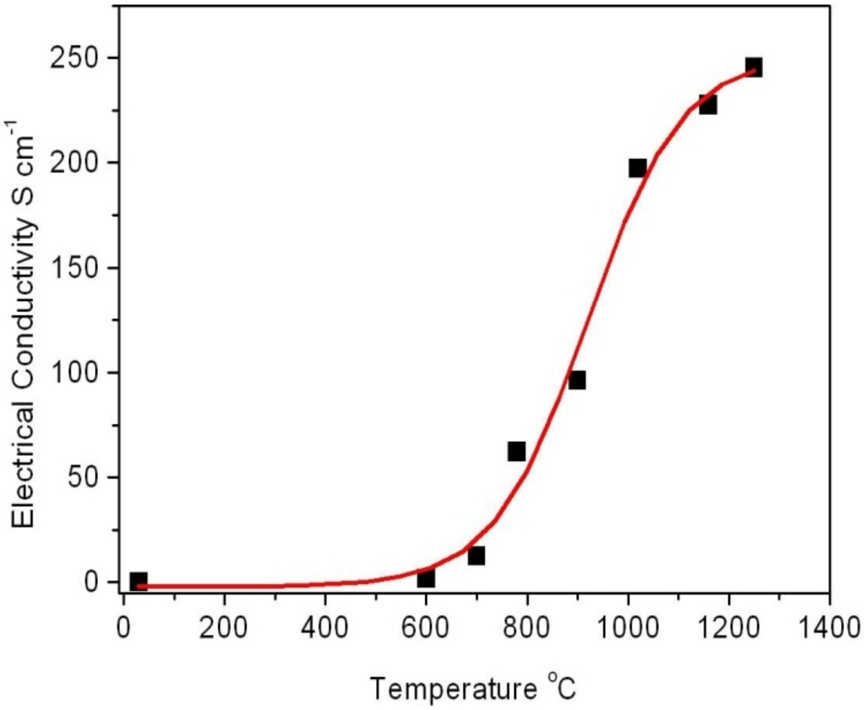

Figure 4.6 Electrical conductivity as a function of burnout temperature.

Table 4.3 Electrical conductivity of brown parts with respect to burnout temperature.

Brown Part Electrical Conductivity							
			A/L		**V/I**		
Length (mm)	**Breadth (mm)**	**Width (mm)**	**(L=0.01 m)**	**V (Volts)**	**(I = 0.1 Amperes)**	**Conductivity (S/cm)**	**Burnout Temperature °C**
40.8	5.72	5.68	0.003249	1.846	18.46	0.1667339	30
33.54	5.97	4.4	0.0026268	0.205	2.05	1.857030905	600
40.14	5.84	4.16	0.00242944	0.032491	0.32491	12.66866185	700
33.54	5.8	4.08	0.0023664	0.00679	0.0679	62.23605688	780
39.64	5.15	4.93	0.00253895	0.00409	0.0409	96.29916993	900
40.54	5.54	4.33	0.00239882	0.002113	0.021127	197.3207372	1020
39.72	5.78	4.12	0.00238136	0.001845	0.01845	227.6033107	1160
40.32	5.5	4.74	0.002607	0.00156	0.01563	245.41437	1250

The results of x-ray diffraction (XRD) performed on the phenolic resin before and after pyrolysis at temperatures varying from 600 ºC to 1000 ºC and compared with the XRD of graphite are shown in Figure 4.7. The results show that the carbon product of the phenolic burnout at 600 ºC is amorphous in nature. At temperatures above 1000 ºC, the XRD pattern indicates a morphology change that suggests that there is a certain amount of ordering of the graphitic structure tending towards semi-crystallinity. This is most apparent in the increase in sharpness of the peak at $2\theta \approx 43^\circ$ with increasing heat treatment temperature.

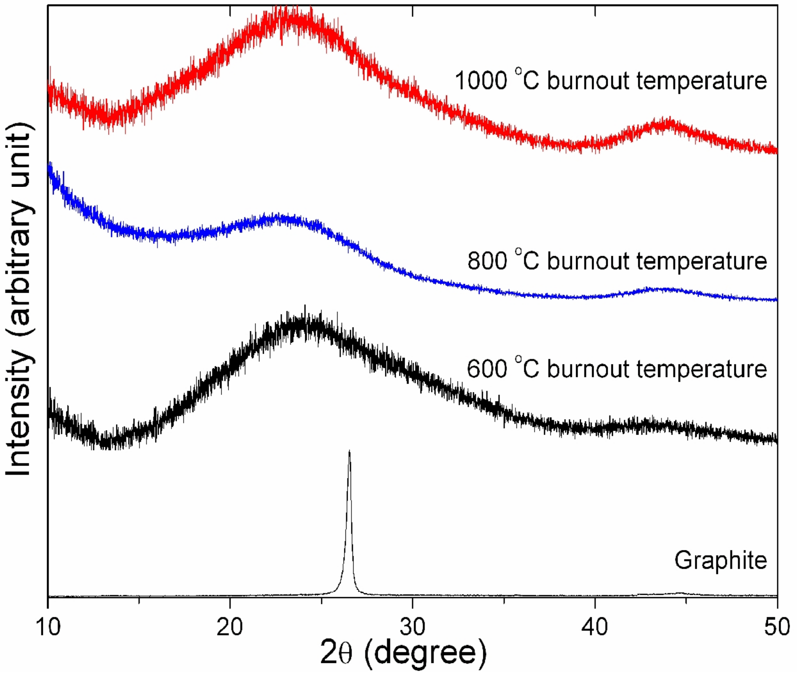

Figure 4.7 XRD patterns of phenolic resin pyrolyzed at different temperatures.

4.4.2 MECHANICAL STRENGTH

As bipolar plates are more frequently subjected to compressive and bending loads, the flexural strength is therefore a useful measure of a bipolar plate's ability to withstand mechanical loads during operation. As discussed in the previous chapter, the D.O.E target for flexural strength of bipolar plates is set at 4 MPa. Figures 4.8a and b show the results of the three point bending tests performed to evaluate the cyanoacrylate infiltrated graphite flexural samples described in Chapter 3.4.2. The flexural strength is defined as the value of stress at which the sample fractures in a three point bend test. As seen in Figure 4.8a, the flexural strength of the sample is around 40 MPa which far exceeds the D.O.E specification. Figure 4.8b represents the flexural strengths of a set of five cyanoacrylate infiltrated samples. The average flexural strength of the infiltrated samples is around 31.5 MPa.

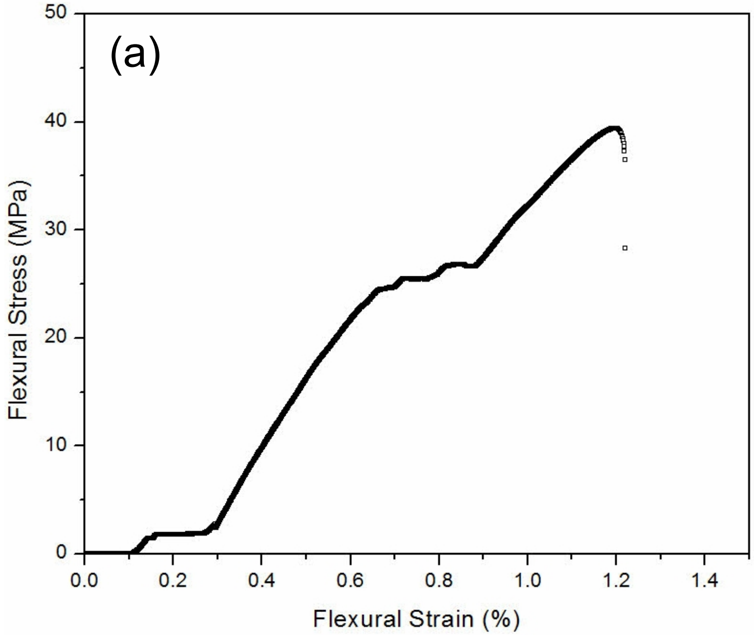

Figure 4.8a Flexural stress versus flexural strain obtained from three point bending test.

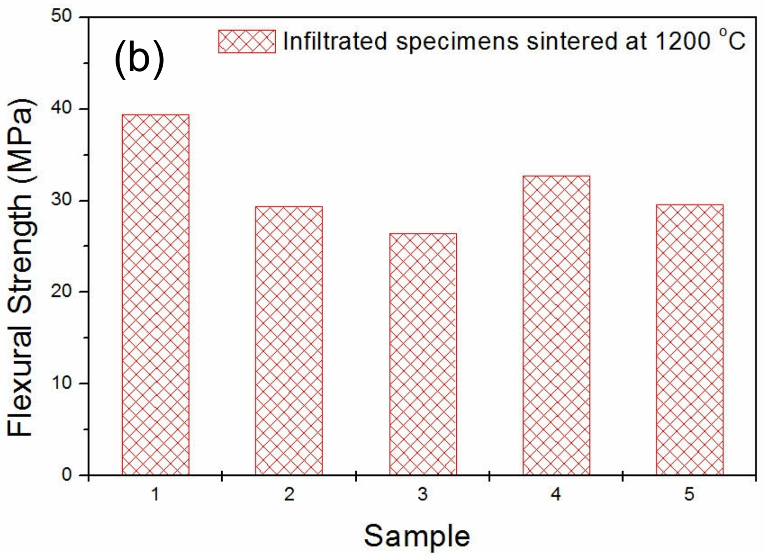

Figure 4.8b Flexural strengths of samples infiltrated with ethyl cyanoacrylate.

4.4.3 THERMAL CONDUCTIVITY

Table 4.4 presents the results of the thermal conductivity of the cyanoacrylate infiltrated graphite parts. The thermal conductivity of the plates increases from 7.3 W/m.K at room temperature to 7.9 W/m.K. This is slightly lower than the D.O.E target of 10 W/m.K for bipolar plates at room temperature.

Table 4.4 Thermal properties of cyanoacrylate infiltrated graphite parts.

Temperature ºC	Thermal Conductivity W/m.K	Thermal Diffusivity m^2/s	Volumetric Heat Capacity $J/m^3.K$
23	7.31	6.34	1.15
60	7.89	6.00	1.31

4.5 CARBON FIBER ADDITION

4.5.1 MICROSTRUCTURE

Figure 4.9 shows a representative microstructure of an indirect laser sintered (LS) brown part containing 26% carbon fiber (CF). The graphite and CF are easily distinguished. Particle binding is accomplished by residual carbon ligaments from phenolic dissociation. This is the microstructural feature most significantly affecting both strength and electrical conductivity for brown parts.

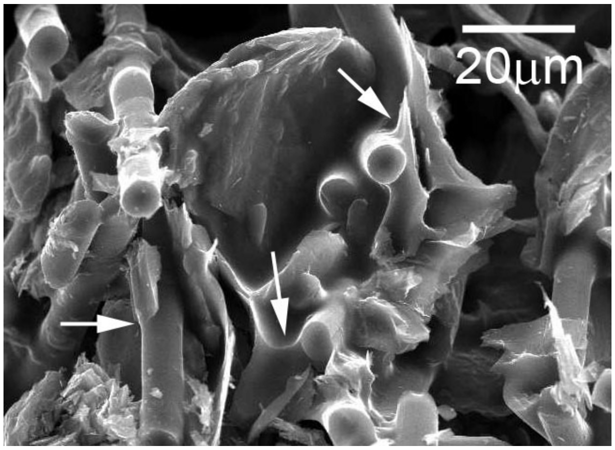

Figure 4.9 SEM micrograph of an indirect LS brown part containing 26% carbon fiber. Natural graphite and carbon fiber are morphologically distinguished. Dissociated phenolic is clearly present (arrows) and binds graphite and the carbon fiber.

4.5.2 FLEXURAL STRENGTH

The flexural strength of indirect LS graphite-CF green parts is shown in Figure 4.10. For green parts, the principal binding mechanism is largely uncured phenolic which has melted under the laser beam, flowed to wet adjacent particles and solidified on cooling. Addition of CF results in an increase in flexural strength, from about 2 MPa for straight carbon-phenolic mixtures to 4 MPa for 26% CF addition.

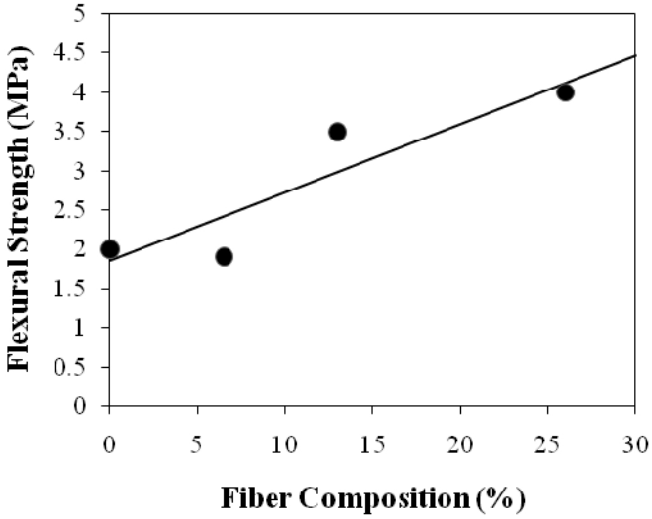

Figure 4.10 Flexural strength of green parts after laser sintering. Carbon fiber additions to 26% result in doubling of green part strength.

Figure 4.11 shows the flexural strength of LS graphite-CF brown parts as a function of CF addition and phenolic dissociation temperature. Similar to the green part effect, CF addition increases the flexural strength of the brown parts. Generally, increasing the phenolic dissociation temperature increases brown part strength, although there is a uniform decrease in strength for parts dissociated at 600°C. For 1200°C dissociation temperature, CF addition of 26% results in more than tripling of the brown part strength from 3 MPa to 10 MPa.

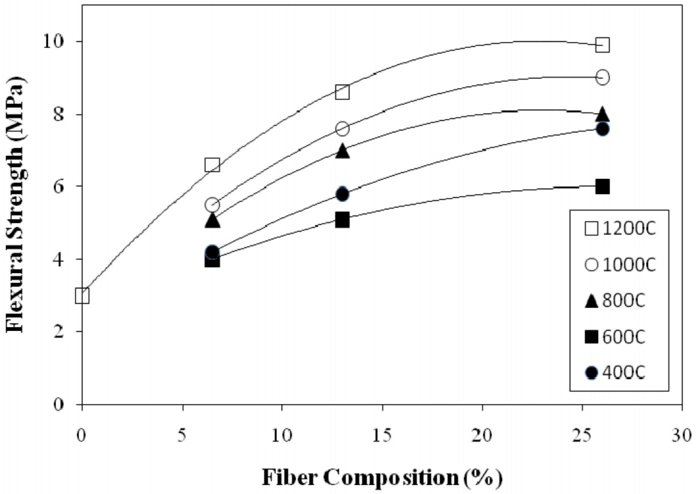

Figure 4.11 Effect of phenolic dissociation temperature and carbon fiber addition on flexural strength of indirect LS brown parts.

Increased dissociation temperature and carbon fiber addition result in increased brown part strength. Figure 4.12 illustrates the effect of CF addition on the flexural strength of final parts obtained by infiltrating brown parts with epoxy resin. CF additions increase the strength by about 40%, from 35 MPa to almost 50 MPa. The parts were laser sintered, phenolic dissociated at 1000°C, infiltrated with liquid epoxy and cured. Over the range, flexural strength increases by 40%.

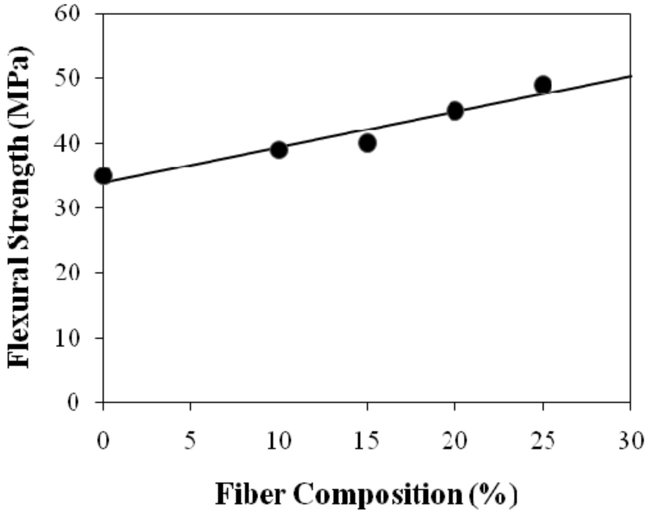

Figure 4.12 Effect of carbon fiber addition on the flexural strength of final indirect LS parts.

4.5.3 ELECTRICAL CONDUCTIVITY

The effect of phenolic dissociation temperature and CF addition on electrical conductivity of LS brown parts is shown in Figure 4.13. The electrical conductivity is uniformly low for phenolic dissociation temperatures less than 600°C. For dissociation at 800°C, the electrical conductivity rose sharply to about 70 S/cm and was independent of CF addition. Electrical conductivity increased for higher dissociation temperatures, but above 800°C, CF addition has a detrimental effect.

Epoxy infiltration of brown parts dissociated at 1000°C did not affect the electrical conductivity. This is demonstrated in Figure 4.14 where closed symbols represent LS finished parts and open symbols represent LS brown parts dissociated at 1000°C (from Figure 4.13). It is seen that carbon fiber additions as small as 5% result in a dramatic drop in electrical conductivity, from 400 S/cm to just over 100 S/cm. The electrical conductivity continues to decrease, dropping to 50 S/cm for 26% CF addition.

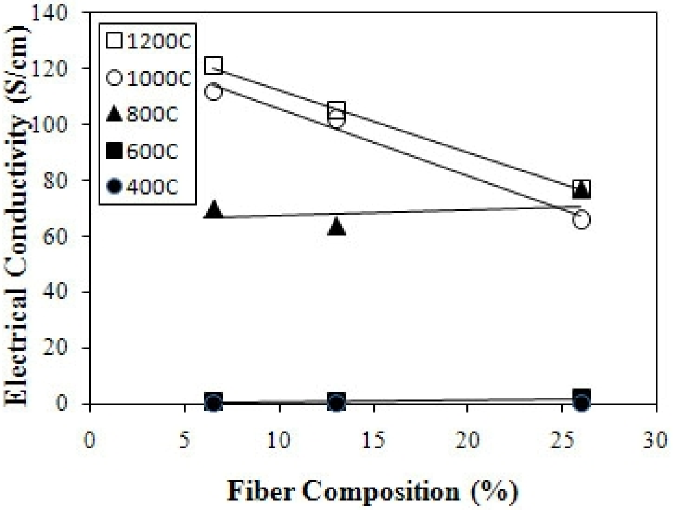

Figure 4.13 Effect of phenolic dissociation temperature and carbon fiber addition on the electrical conductivity of laser sintered brown parts.

The electrical conductivity initially is very low. It increases dramatically for dissociation temperatures equal to and greater than 800°C. Carbon fiber additions do not affect electrical conductivity for dissociation temperatures of 800°C and less. For high dissociation temperature, carbon fiber additions decrease the measured electrical conductivity.

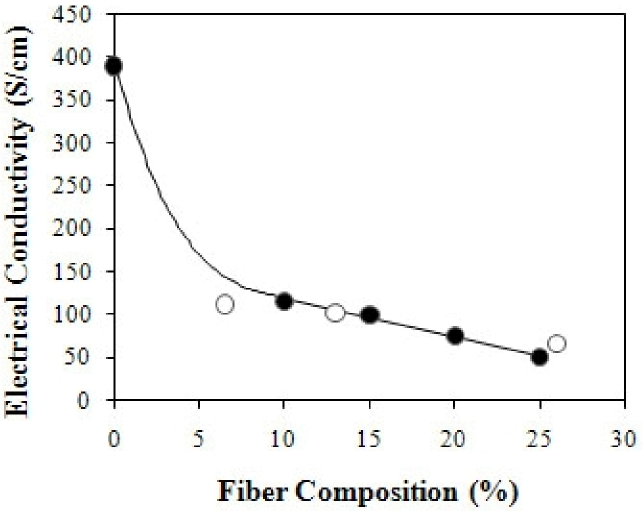

Figure 4.14 Effect of carbon fiber addition on the electrical conductivity of final LS parts (closed symbols).

The parts were laser sintered, phenolic dissociated at 1000°C, infiltrated with liquid epoxy and cured. Open symbols represent brown parts prior to infiltration with epoxy. The electrical conductivity is not affected by epoxy infiltration.

4.6 PROCESS VALIDATION

Figure 4.15 shows the polarization curves of the plates tested to validate the laser sintering process for producing bipolar plates. The plates produced by indirect laser sintering worked without fuel leakage and produced repeatable results. The plate set with uniform width channels and 11 passes exhibited performance comparable to the commercially manufactured plate set. The plates with the flow field possessing varying width channels performed comparable to the commercial plates at low current densities but shows higher losses at a current density of ~70 mA/cm^2, which then increase as the mass transport limitations set in. As expected, the plate set with 9 passes of uniform width shows the poorest performance of the four plates tested with the highest ohmic and mass transport losses. The second y-axis plots the power density of the fuel cell tested in mW/cm^2. The curves show the variation of the power output with increasing load on the fuel cell.

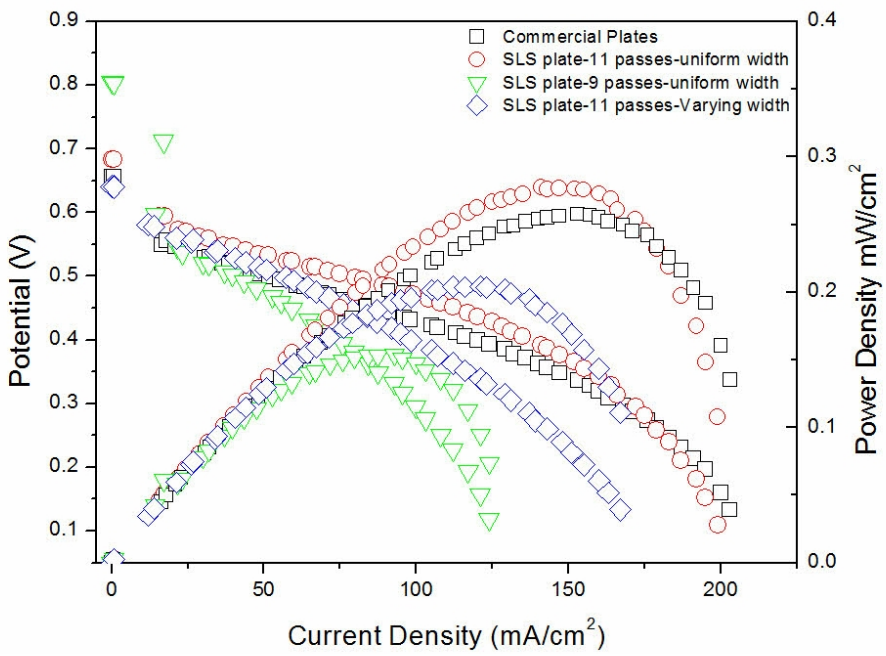

Figure 4.15 Polarization curves of initial plates tested for process validation.

4.6.1 TESTING NOVEL BIPOLAR PLATE DESIGNS

The performance of the three sets of laser sintered plates with 5 cm^2 flow field of 10 channel passes is compared with the commercial plates in Figure 4.16. At high current density, it can be seen that the plates with triangular and elliptical channel cross sections perform comparably to the commercial plates with the cell voltage being equal. At current densities lower than ~ 325 mA/cm^2, the ohmic losses are slightly more for the laser sintered plates. The laser sintered plates with a rectangular cross section showed significantly poorer performance than the other plates with much higher ohmic and mass transport losses.

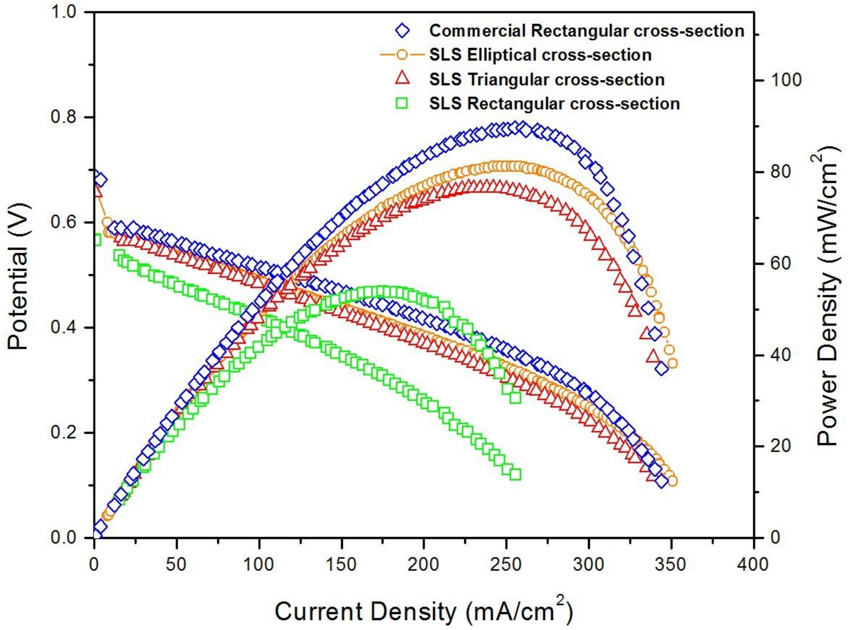

Figure 4.16 Polarization curves of plates with 5cm^2 flow field of 10 channel passes.

The results of scaling up the size of the 5 cm^2, 10 pass plates to a 10 cm^2 flow field area is shown in Figure 4.17. As there were no commercial plates with the same flow field area, the plot compares only the polarization curves of the laser sintered plates. It can be seen that the performance of the plates with 10 cm^2 flow area is very similar to the results of the 5 cm^2 flow field plates shown in Figure 4.16, verifying that the indirect laser sintering process of producing graphite bipolar plates is capable of producing repeatable results that are also scalable.

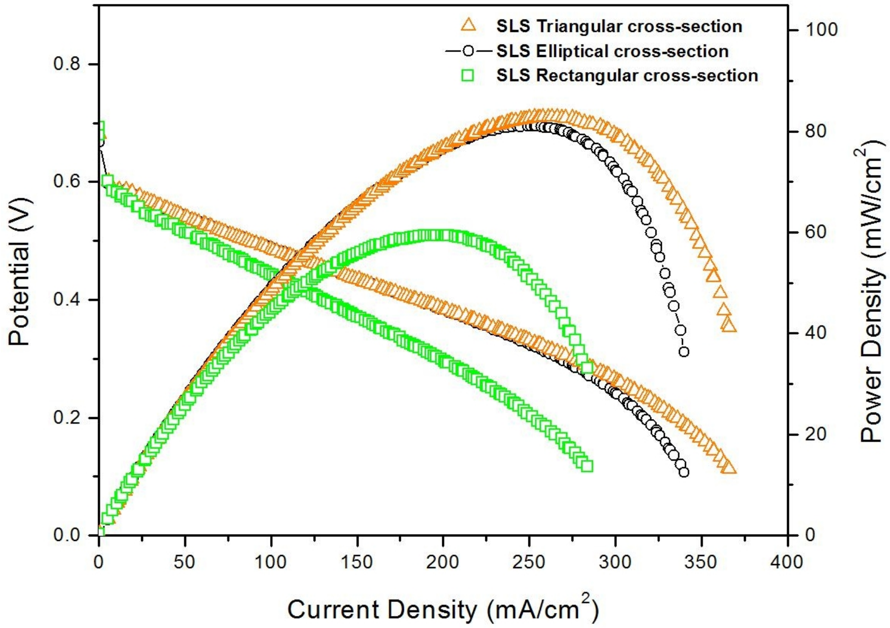

Figure 4.17 Polarization curves of plates with 10 cm^2 flow field of 13 channel passes with the same aspect ratio and channel/rib width as the 5 cm^2, 10 pass plates.

The polarization curves for the plates with 5 cm^2 flow field area and 15 channel passes are shown in Figure 4.18. The plates with the triangular and elliptical channel cross-sections show similar performance in the ohmic region (up to ~ 200 mA/cm^2) compared to the commercial plates, while the laser sintered plates with the rectangular channel cross-section has higher ohmic losses than the other plates.

At current densities around 325 mA/cm^2, the laser sintered rectangular channel cross section plates perform the same as the commercial plates. At current densities greater than ~225 mA/cm^2, the polarization curve for the commercial plates shows mass transport limitations, whereas the triangular and elliptical channel cross section plates maintain the ohmic region up to ~375 mA/cm^2 beyond which the mass transport limitation sets in.

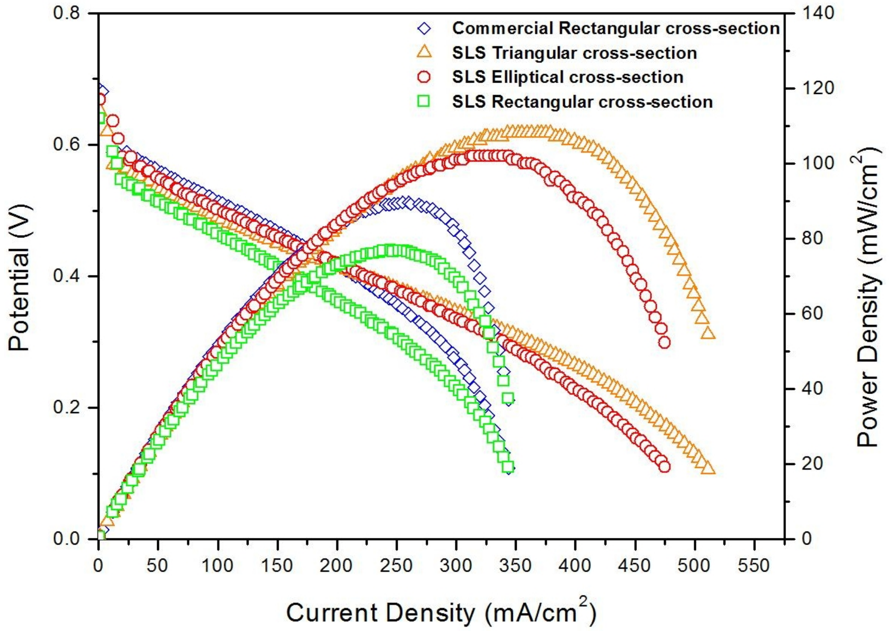

Figure 4.18 Polarization curves of plates with 5 cm^2 flow field of 15 channel passes with the same aspect ratio and channel/rib width as the commercial plates.

Figure 4.19 shows the comparison of the laser sintered plates when tested with H_2 as the anode fuel instead of methanol. The results show that the plates with the triangular and elliptical channel cross sections outperform the rectangular cross section plates in terms of ohmic and mass transport losses, mirroring the results when tested using methanol.

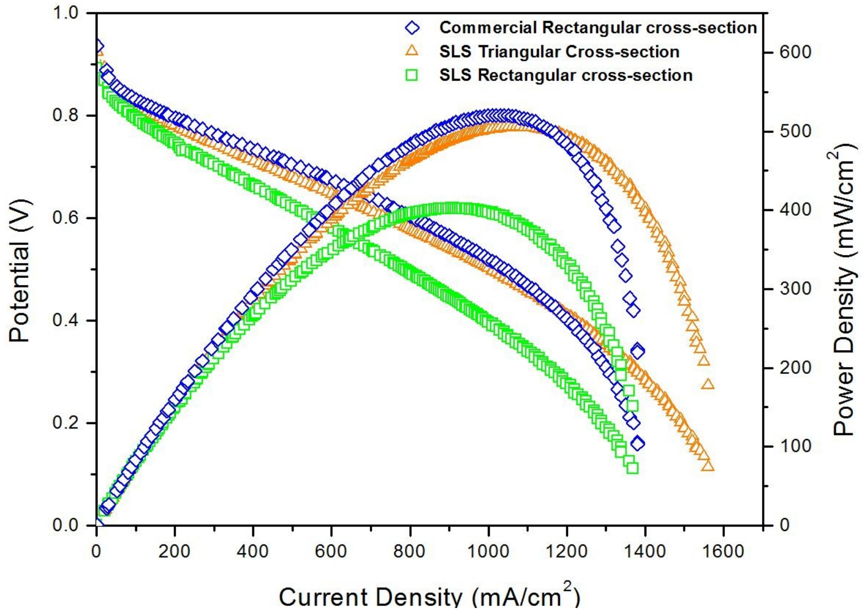

Figure 4.19 Polarization curves of plates with 5 cm^2 flow field of 15 channel passes tested with H_2 and O_2 as the anode and cathode fuels, respectively.

4.6.2 COMPARING TRIANGULAR VERSUS RECTANGULAR CHANNEL CROSS SECTIONS

Comparison of the polarization curves obtained by testing the laser sintered plates with the triangular channel cross section and the commercial plates with the rectangular channel cross section at different anode flow rates and methanol solution concentrations is shown in Figures 4.20 a and b. The results shown in Figure 4.20a compare the performance at the anode and cathode flow rates of 6 ml/min and 200 ml/min, respectively. The triangular channel cross section plates repeat the same superior mass transport performance seen in the previous results. Figure 4.20b presents the results of increasing the methanol solution concentration to 2M and reducing the anode flow rate to 3 ml/min while keeping the cathode flow rate constant at 200 ml/min. It can be seen that the performance of the fuel cell doubles in both cases with the laser sintered plates maintaining better mass transport characteristics.

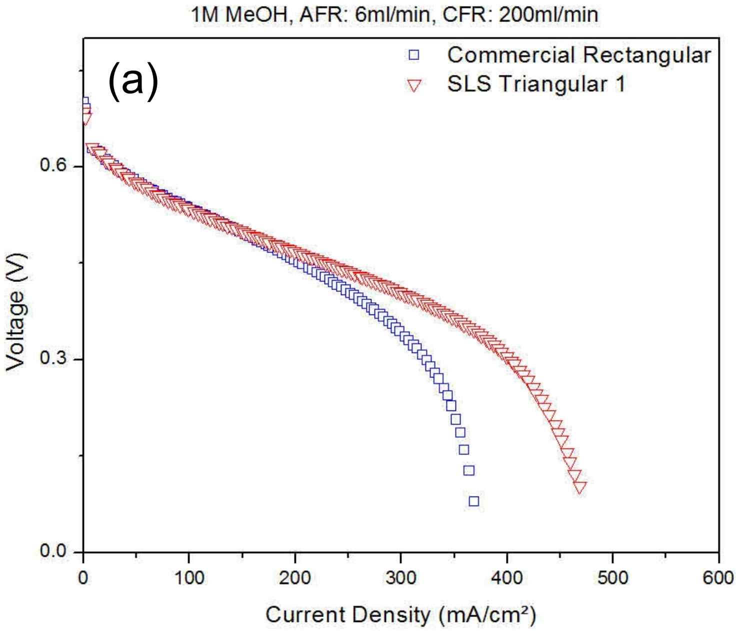

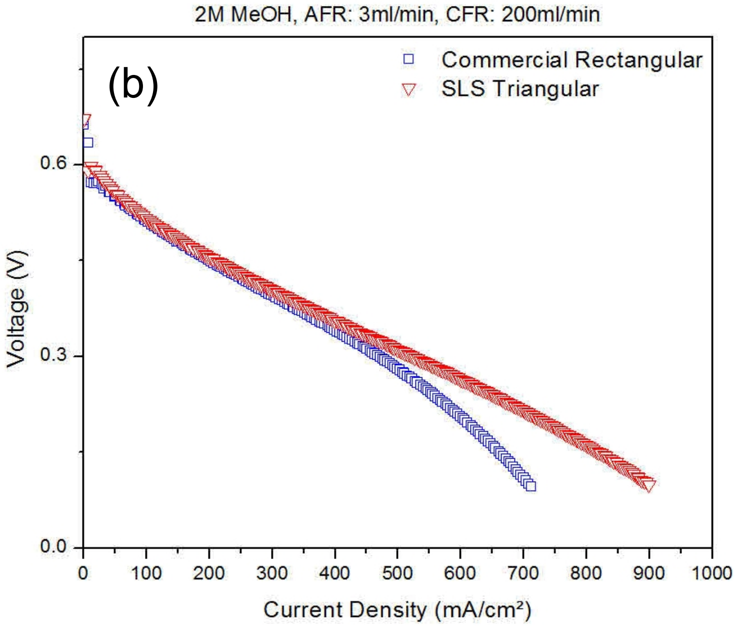

Figure 4.20 Polarization curves using a) 1M methanol solution and anode flow rate 6 ml/min, b) 2M methanol solution and anode flow rate of 3 ml/min.

Figures 4.21a, b and c show the results of the constant current experiments at 1.5 A, 1.75 A and 1.875 A, respectively. At a constant current of 1.5 A, there is not much of a difference between the two plate sets. Figure 4.21b shows a marked drop in the cell voltage of the commercial plates at a constant current of 1.75 A when compared to that of the laser sintered plates. At a constant current of 1.875 A, the commercial plates show a instantaneous drop in the cell voltage at the beginning of the test while the laser sintered plates maintain a steady low gradient drop in cell voltage.

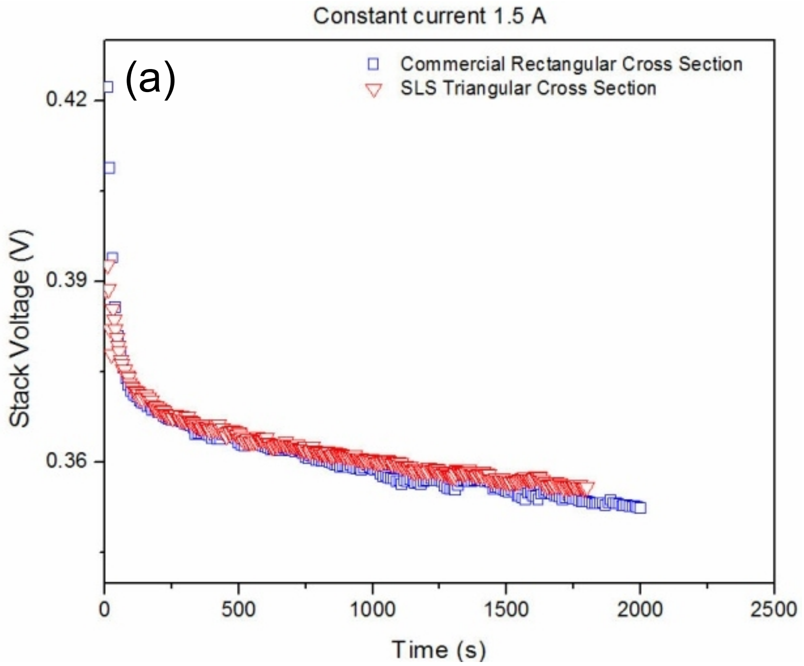

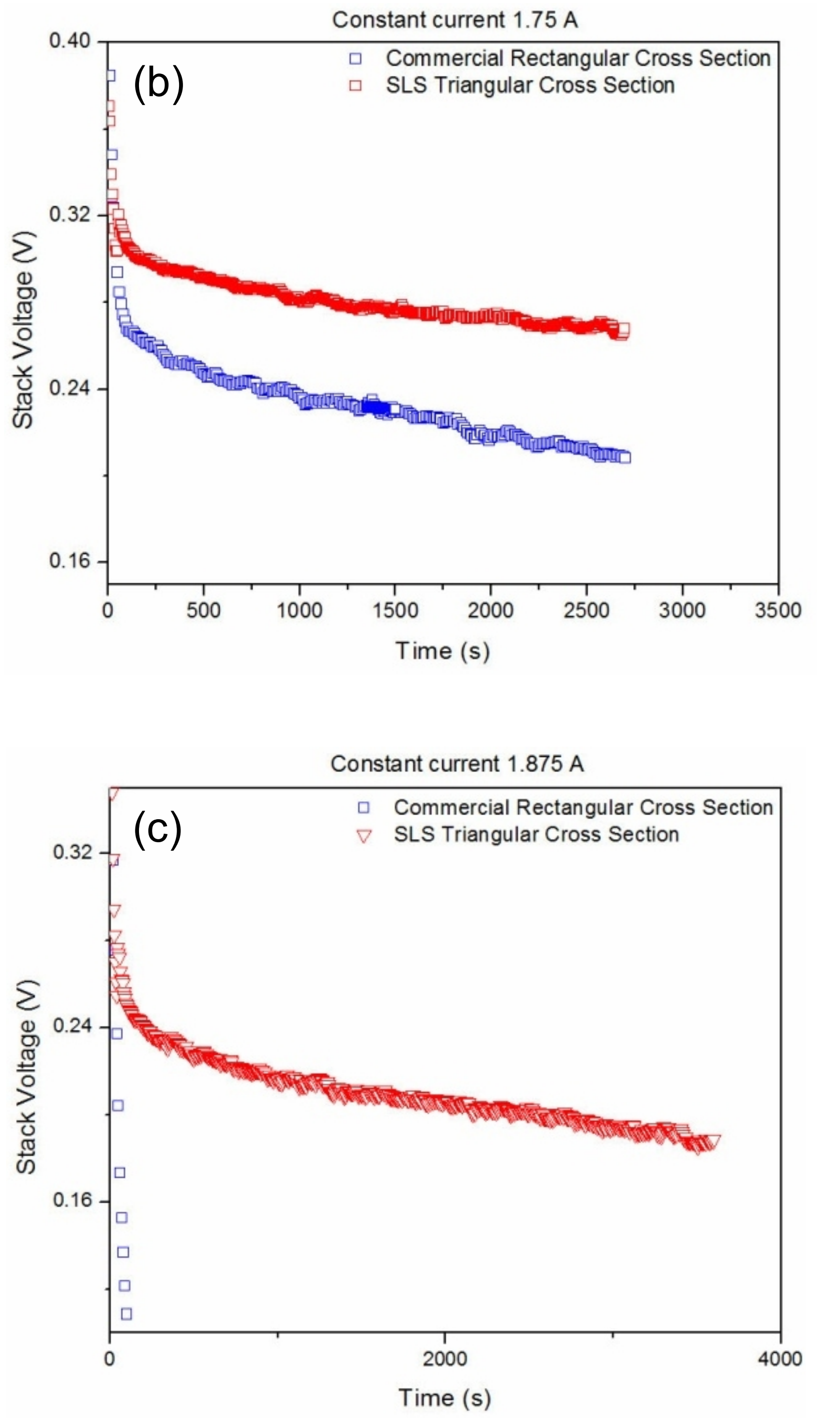

Figure 4.21 Constant current curves at a) 1.5 A, b) 1.75 A, c) 1.875 A

Figure 4.22 shows the results of varying the cathode flow rate while maintaining the anode flow rate and methanol solution concentration constant at 6 ml/min and 1M, respectively. It can be seen that the there is no change in the performance of the commercial plates on changing the cathode flow rate from 200 ml/min to 100 ml/min. The laser sintered plates has better performance than the commercial plates at a cathode flow rate of 200 ml/min but at a flow rate of 100 ml/min, there is a significant change in the polarization curve. The triangular plates show a very erratic ohmic region and a marked reduction in mass transport performance.

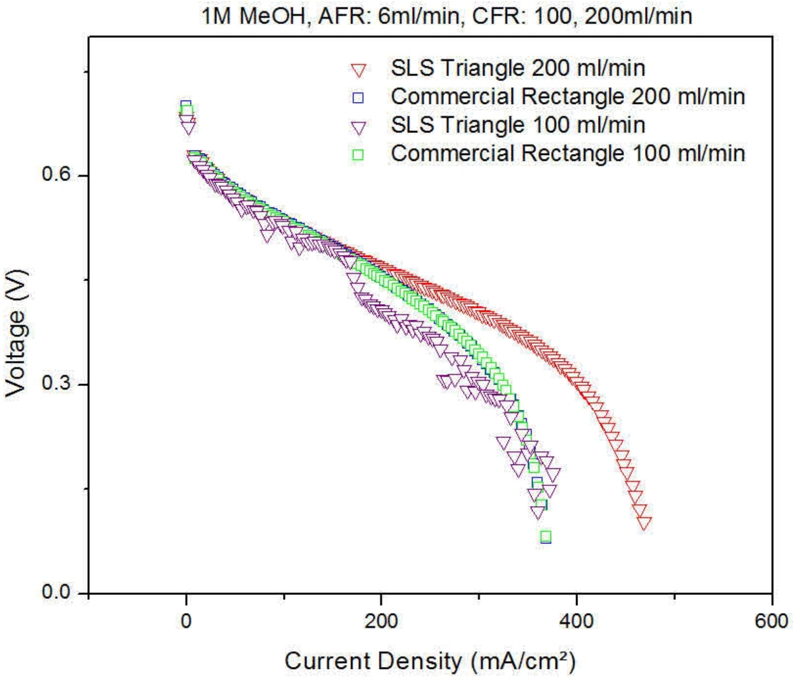

Figure 4.22 Polarization curves obtained by varying cathode flow rates.

4.6.3 MANIFOLDED BIPOLAR PLATES

The plot in Figure 4.23 compares the performance of the manifolded plates when being tested with varying flow rates and different fuel inlet configurations with a set of commercially procured plates with 25 cm^2 triple serpentine flow field area. From Figure 4.23 it is apparent that the manifolded plates had significantly poorer performance than the commercial plates. Increasing the anode flow rate improved the performance, as did changing the fuel supply configuration from four individual inlets to a single inlet with four outlets.

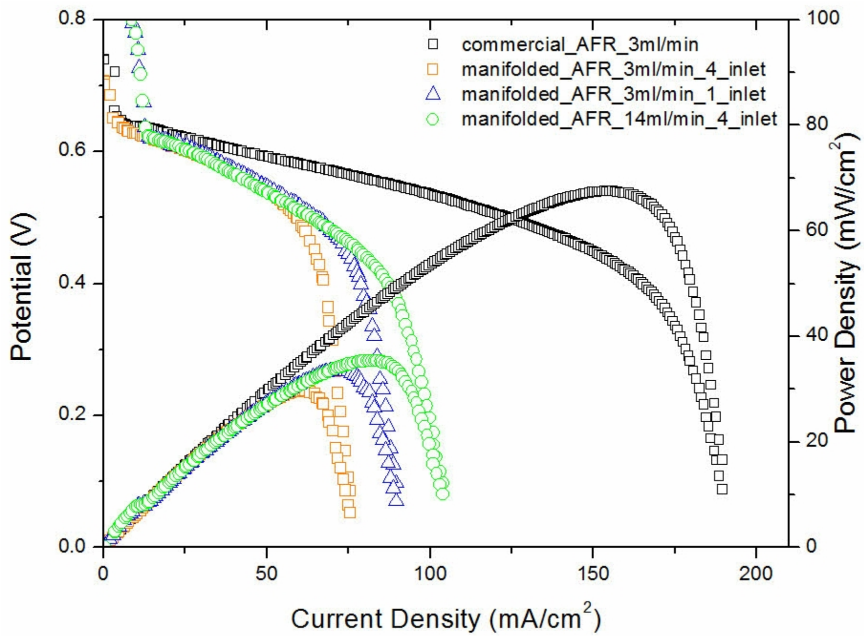

Figure 4.23 Polarization curves of manifolded plates at varying anode flow rates and fuel inlet configurations.

4.7 METHANOL CROSSOVER

Figures 4.24a-d compare the results of the experiments to quantify methanol crossover in a fuel cell when operated using plates fabricated by the laser sintering process. Figure 4.24a shows the methanol crossover comparisons for the plates made for validation of the indirect LS process. Figures 4.24 b-d compare the crossover currents for the three plate sets of rectangular, triangular and elliptical plates with active flow field areas and number of passes of 5 cm^2 and 10 passes, 10 cm^2 and 13 passes and 5 cm^2 and 15 passes respectively. The results of the crossover current measurement for each of the laser sintered plate sets were compared with that of the commercial plates with 5 cm^2 active area and rectangular cross section channels making 15 passes. The amount of methanol crossing over to the cathode side is quantified by the current generated due to methanol oxidation, represented by the flat portion of the curve.

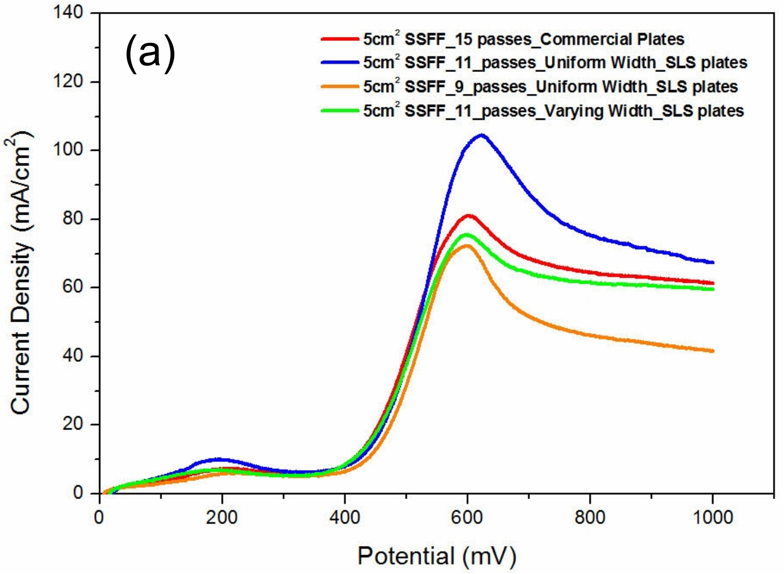
(a)
5cm^2 SSFF_15 passes_Commercial Plates
5cm^2 SSFF_11_passes_Uniform Width_SLS plates
5cm^2 SSFF_9_passes_Uniform Width_SLS plates
5cm^2 SSFF_11_passes_Varying Width_SLS plates
Current Density (mA/cm^2)
0
20
40
60
80
100
120
140
Potential (mV)
0
200
400
600
800
1000

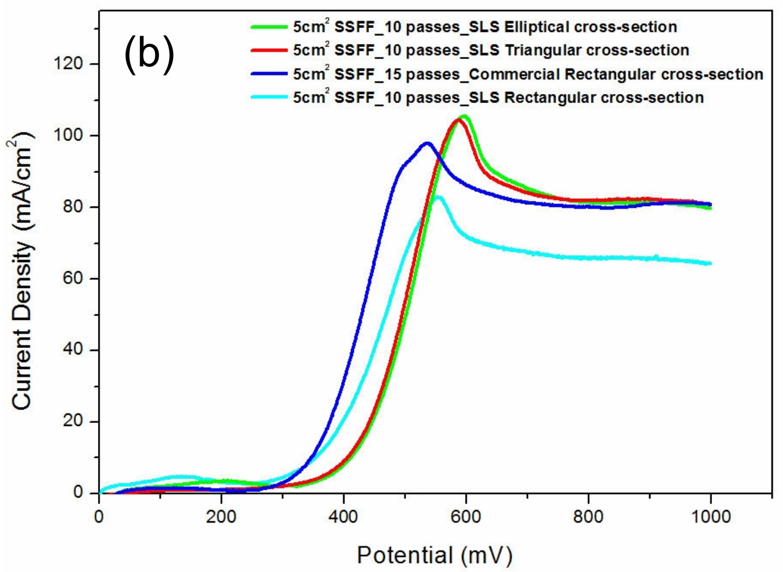
(b)
5cm^2 SSFF_10 passes_SLS Elliptical cross-section
5cm^2 SSFF_10 passes_SLS Triangular cross-section
5cm^2 SSFF_15 passes_Commercial Rectangular cross-section
5cm^2 SSFF_10 passes_SLS Rectangular cross-section
Current Density (mA/cm^2)
0
20
40
60
80
100
120
Potential (mV)
0
200
400
600
800
1000

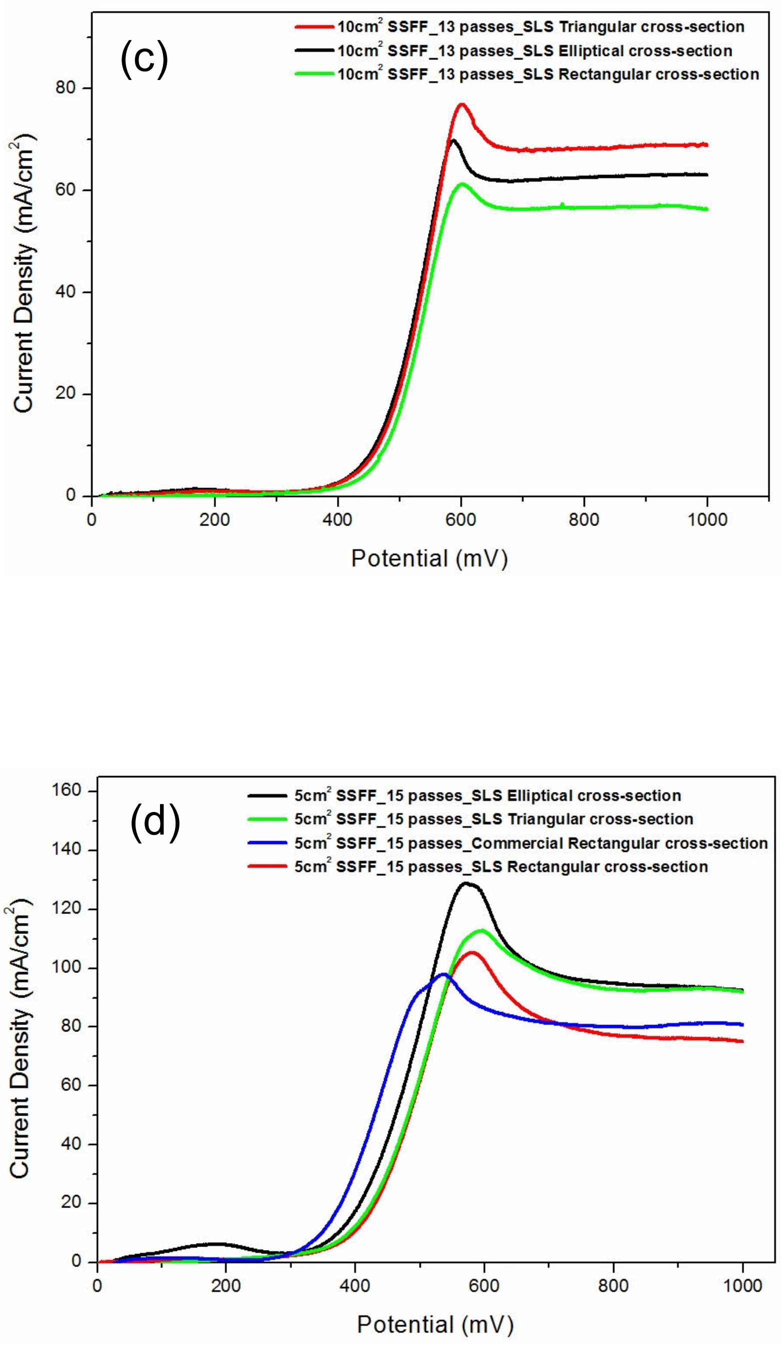

Figure 4.24 Methanol crossover comparisons of a) plates made for process validation, b) SSFF 5 cm^2, 10 passes, c) SSFF 10 cm^2, 13 passes, d) SSFF 5 cm^2, 15 passes

Chapter 5. Discussion

5.1 INTRODUCTION

In this chapter are discussed, the results of the infiltration, conductivity and fuel cell tests presented in Chapter 4.

5.2 INFILTRATION

5.2.1 METAL BASED INFILTRANTS

From the results of experiments on infiltrating the graphite parts with conductive epoxy and electroless nickel deposition, it is clear that full densification of the porous substructure is difficult to achieve. From Figure 4.1a it can be seen that there is insufficient penetration of the epoxy in the interior of the plate, as is evidenced by the lack of silver in the interior of the plate. Diluting the epoxy with thinners, such as xylene and methoxy propanol acetate, to reduce the viscosity, resulted in the thinners evaporating once the parts were cured, leaving behind porosity which acted as sources of leaks when the bipolar plates were tested using pressurized fluids.

The experiments conducted to improve conductivity and full densification of the graphite parts using electroless nickel deposition did not yield expected results as is evident from Table 4.2. The experiments were discontinued due to the fact that nickel and silver are electrochemically unstable in the environment of the fuel cell. Figures 5.1a and b show the Pourbaix diagrams for silver and nickel, respectively. The diagrams represent the stability of a given element at different pH and potentials. At a pH of 2-3 and potential of ~ 1 V and temperatures of 60 ºC – 80 ºC , which is an approximation of the environment of a DMFC, it can be seen that the silver and nickel would be oxidized to

Ag^+ and Ni^{2+} respectively. The electrochemical stability of nickel and other metals including stainless steel and titanium have been reported by different authors to be prone to corrosion and dissolution, with nickel being particularly susceptible [79, 80].

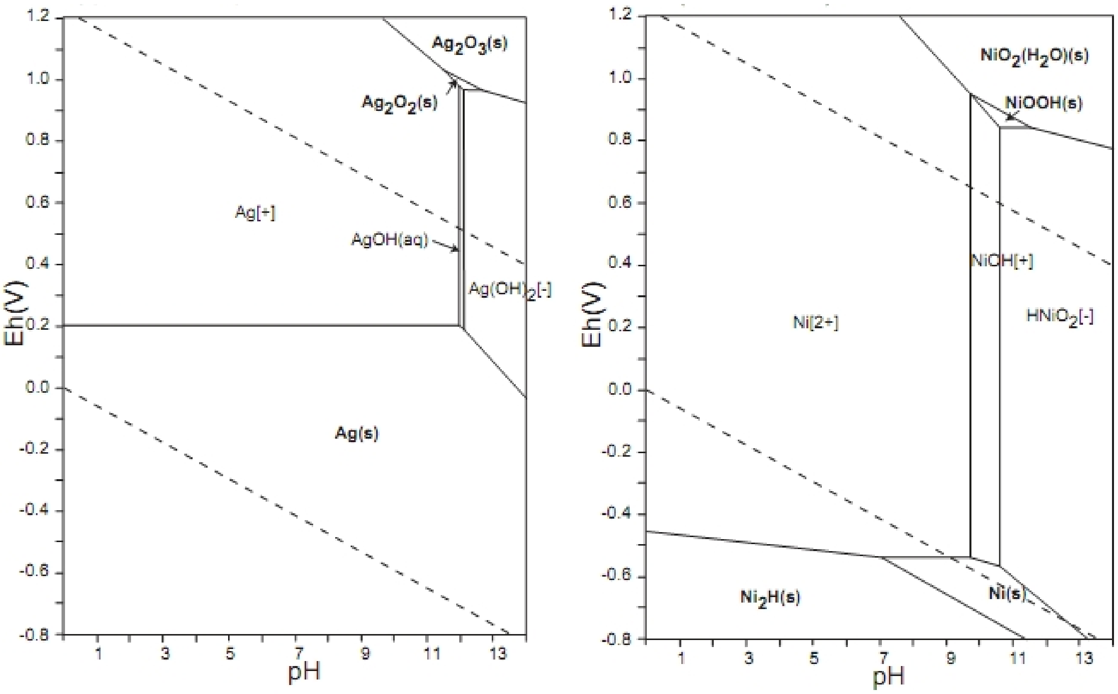

Figure 5.1 Electrochemical stability Pourbaix diagrams for a) Silver, b) Nickel

5.2.2 ELECTRICALLY CONDUCTIVE POLYMERS

Figures 4.3b-d show SEM images of the graphite parts after being subjected to electropolymerization. Due to the small pore size (~ 60 μm) of the part, clogging of the surface occurred during deposition of the polymer which prevented fresh monomer from accessing the interior structure of the part. This can be seen in the SEM images in Figure 4.3b-g. Both the polythiophene and polyaniline form significant coats on the surface of the part while the interior shows no change in structure from an uninfiltrated part (Figure 4.3a). Furthermore, the deposition process was time consuming and did not produce a uniform surface coating which necessitates further post processing.

5.2.3 ETHYL CYANOACRYLATE

The primary reasons for choosing ethyl cyanoacrylate as an infiltrant for laser sintered graphite bipolar plates are that it is available in a range of low viscosities (as low as 5 cps) which provides flexibility for complete infiltration. Additionally, it is non-degradable in methanol with a service temperature range of -54 ºC to 121 ºC that covers the operating range of a DMFC. Rapid room temperature curing of ethyl cyanoacrylate is enhanced by the presence of moisture, and it is easily procurable commercially. If not careful, infiltration by flowing cyanoacrylate through the LS plates can cause clogging of the flow field channels and therefore alter the geometry and performance of the parts. Due to the high electrical resistivity of the cyanoacrylate ($\sim 1\times10^{16}$ Ω.cm), surface polishing was necessary to expose the graphite matrix to maintain the electrical conductivity required for efficient DMFC operation.

5.3 ELECTRICAL CONDUCTIVITY

The Department of Energy has set target parameters for the material properties of bipolar plates for which electrical conductivity is set to be 100 S/cm [81]. It is known that thermal and electrical conductivities of materials are affected by both porosity and non-conducting inclusions. Porosity has been derived by Koh et al. [82] to affect thermal and electrical conductivity per the equation:

$$J / Jo = (1-\varepsilon) / (1+n\varepsilon^2) \tag{5.1}$$

where J/Jo is the ratio of porous conductivity to fully densified conductivity, ε is the fractional porosity and n is the sensitivity to the presence of pores.

Research by Bhatia et al. [83] has shown that the open porosity in phenol formaldehyde resins increases with temperature up to 800 ºC. As seen in Curve C of Figure 5.2a, above 800 ºC, the porosity of the carbonized resin drops in a linear fashion with increasing temperature. This in conjunction with porosity vs. conductivity studies by Koh et al. suggests that the conductivity of the graphite parts is affected by reducing the open porosity of phenol formaldehyde resin by carbonizing at high temperatures.

Studies of phenol formaldehyde resin have shown that the electrical resistivity is highly dependent on the pyrolyzation temperature and that there is a change on the order of about 10^2 between treating at 800 ºC and 1250 ºC [83]. This was verified by measuring the electrical conductivities of selected brown parts and plotting them as a function of the pyrolyzation temperature (Figure 4.6). The relationship between the carbonization of phenolic resin and electrical conductivity of the graphite parts is apparent on comparison of Figure 4.6 to Figure 5.2b which shows the electrical resistivity of pyrolyzed phenolic resin reducing as heat treatment temperature increases.

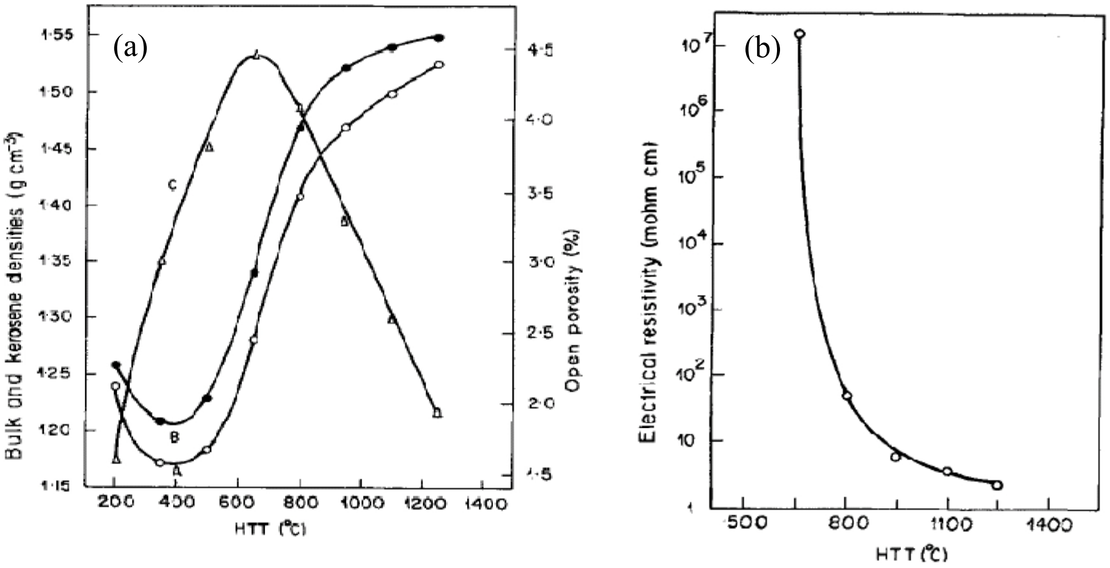

Variation of (A) bulk density, (B) kerosene density, and (C) open porosity of phenol formaldehyde resin based plates with increasing temperature of heat treatment.

Figure 5.2 a) Variation of bulk density, kerosene density and open porosity as a function of pyrolysis temperature, b) Electrical resistivity of phenolic resin as a function of pyrolysis temperature [83].

The distinct sharpening of the peak at 2θ ≈ 43° with increasing heat treatment temperature in the XRD patterns plotted in Figure 4.7 suggests graphitization of the carbon product of phenolic pyrolysis. The graphitization is made more apparent at higher pyrolysis temperatures (Figure 5.3) as is evident from the work of Tzeng et al. [84] on the properties of pyrolyzed carbon/carbon composites. The increase in electrical conductivity of the laser sintered graphite parts may therefore be attributed in part to the conversion of amorphous carbon into a semi-crystalline phase and also a reduction in porosity of the phenolic carbonization residue.

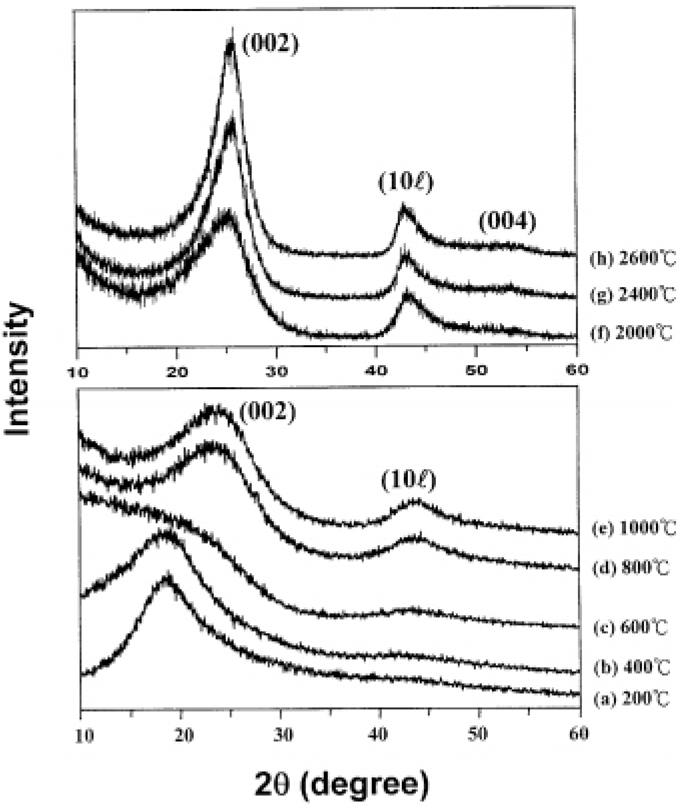

Figure 5.3 XRD patterns of phenolic resin after pyrolysis at different temperatures [84].

5.4 CARBON FIBER ADDITION

5.4.1 STRENGTH AND CONDUCTIVITY OF GRAPHITE AND CARBON FIBERS

The intrinsic flexural strength of graphite and CF has been reported to be on the order of 5 MPa and 2000 MPa, respectively. Electrical conductivity of these materials is on the order of 1000 S/cm and 300 S/cm, respectively [85].

5.4.2 LS GREEN PARTS

The LS green part flexural strength increased from 2 MPa to 4 MPa with up to 26% CF addition. Improvement in the ability to handle parts without fracture was apparent, although care still must be taken to successfully remove parts from the powder bed and to remove loose powder from the parts.

The flexural strength of cured phenolic is estimated to be on the order of 7 MPa [85]. The flexural strength of LS green parts is estimated based on a modified rule of mixtures approach with a power-law relative density effect [86]:

$$\sigma_{green} = \Delta^{m}[V_{ph}\sigma_{ph} + V_{cf}\sigma_{cf} + \left(1 - V_{ph} - V_{cf}\right)\sigma_{gr}] \qquad (5.2)$$

where σ_{green} = calculated flexural strength of the LS green part, Δ = relative density of the LS green part $\approx$ 0.4, m = exponential dependency of porosity $\approx$ 3-6, V_{ph} = volume fraction of phenolic in mixture $\approx$ 0.3, V_{cf} = volume fraction of CF in mixture = 0.26 (max), σ_{ph} = flexural strength of phenolic $\approx$ 7 MPa, σ_{cf} = flexural strength of CF $\approx$ 5 MPa, and σ_{gr} = flexural strength of graphite $\approx$ 2000 MPa. The estimated flexural strength of the LS green part containing 26% CF is approximately 4 MPa if a reasonable value of the exponent m of 5.3 is used. However, this results in an underestimation of the flexural strength of the LS green part containing no CF.

5.4.3 LS BROWN PARTS

Flexural strength for brown parts depends on the amount of CF addition and the phenolic dissociation temperature. Similar to green part strength, the effect of CF addition is sensible and consistent qualitatively with reinforcement additions in composites. Adding strong fiber increases the strength.

The effect of phenolic dissociation temperature on brown part flexural strength is complex (Figure 4.11). Brown part strength is increased relative to green part strength up to ~ 400 ºC. Dissociation between 400 ºC and 600 ºC reduces the strength. Above 800 ºC, the strength increases. The only component in the part that is affected by temperature is the phenolic phase. Heating from room temperature, a series of mechanisms act on phenolic which affect its strength. First, by ~200 ºC, the thermoset phenolic completely cures. Above 400 ºC, it dissociates in the solid state, leaving behind approximately 50% carbon in a porous structure. Continued heating results in a combination of densification and phase change, typically from an amorphous to a crystalline morphology. It is feasible that the strength of the phenolic is increased by cross linking (up to 400 ºC). When it dissociates between 400 ºC and 600 ºC, there is a net loss of load carrying capability. Increased temperature partially sinters the residual carbon, resulting in increased strength.

Brown part electrical conductivity is also affected by the amount of CF addition and the phenolic dissociation temperature (Figure 4.13). Since CF has a lower electrical conductivity than graphite, it is understandable that increasing the amount of CF has a detrimental effect on the composite electrical conductivity.

The brown part electrical conductivity is extremely low for dissociation temperatures up to 600 ºC. By 800 ºC, the electrical conductivity increases to about 70 S/cm and is not dependent on the fraction of CF. Above 800 ºC, the brown part electrical conductivity increases, more pronounced for small CF additions. Phenolic has a very low electrical conductivity, 10^{-13} to 10^{-11} S/cm [85]. Once the phenolic dissociates, the ligaments convert to porous amorphous graphite with orders of magnitude higher electrical conductivity [83]. With increased temperature to 1200 ºC, the porosity is reduced, and the structure becomes more crystalline. Both effects increase the electrical conductivity.

The brown part electrical conductivity is dependent on CF composition only above dissociation temperatures of 800 ºC. This is considered to be associated with a transition in electron conduction restriction. When the electrical conductivity of the carbon ligaments created by phenolic dissociation is low compared to the value for CF (300 S/cm), electron flow is limited by the ligaments and there is no effect from CFs. Once carbon ligament electrical conductivity increases (by increasing the dissociation temperature) beyond the electrical conductivity of the CF, the main impediment to electron flow transfers to the CFs. For dissociation temperatures above 800 ºC, the brown part electrical conductivity decreases as CF content is increased.

5.4.4 LS FINISHED PARTS

The flexural strength of finished parts dissociated to 1000 ºC increased from 35 MPa to 50 MPa with increasing CF addition (Figure 4.12). The improvement in strength is associated with epoxy infiltration which provides an additional strong phase. The broad range of flexural strength for neat epoxy falls between 100-150 MPa [85].

The electrical conductivity of epoxy is extremely low, on the order of 10^{-15} S/cm [85], so epoxy infiltration would not be expected change the brown part electrical conductivity. This is confirmed in Figure 4.14 which shows that brown part and finished part electrical conductivities are equivalent.

5.5 LS GRAPHITE BIPOLAR PLATES

Table 5.1 lists the dimensions of the flow fields of the laser sintered plates tested. The results of the tests shown in Chapter 4 validate the capability of the laser sintering process to produce bipolar plates that can be used for testing. The results of the tests also conform to results reported in open literature on the effect of varying channel/rib dimensions and channel cross sectional geometry. The table also lists the hydraulic diameter for the different channel cross sections calculated using the formula:

$$Hydraulic\ Diameter, D_H = \frac{4 \times Cross\ sectional\ Area}{Wetted\ Perimeter} \tag{5.3}$$

Table 5.1 Flow field parameters of laser sintered bipolar plates.

Flow Field Type/Active Area (cm^2)	Channel Cross section	Number of Passes	Channel Length (mm)	Channel Width (mm)	Channel Depth (mm)	Rib Width (mm)	Hydraulic Diameter (mm)
SSFF / 5	Rectangular	9	22.4	1.50	2	1.685	1.71
SSFF / 5	Rectangular	11	22.4	1.00	2	1.548	1.33
SSFF / 5	Rectangular	11	22.4	-	2	-	-
SSFF / 5	Rectangular	10	22.4	1.75	1.75	0.555	1.75
SSFF / 5	Triangular	10	22.4	1.75	1.75	0.555	1.08
SSFF / 5	Elliptical	10	22.4	1.75	1.75	0.555	1.08
SSFF / 10	Rectangular	13	31.5	1.75	1.75	0.75	1.75
SSFF/ 10	Triangular	13	31.5	1.75	1.75	0.75	1.08
SSFF / 10	Elliptical	13	31.5	1.75	1.75	0.75	1.08
SSFF / 5	Rectangular	15	22.4	1.00	1.00	0.50	1.00
SSFF / 5	Triangular	15	22.4	1.00	1.00	0.50	0.618
SSFF / 5	Elliptical	15	22.4	1.00	1.00	0.50	0.618
SSFF / 25	Rectangular	36	24.1	1.50	1.00	1.00	1.2

5.5.1 EFFECT OF CHANNEL/RIB LENGTH, WIDTH AND FLOW FIELD AREA

The channel length of the flow field has been shown by others to have an effect on the overall performance of the fuel cell. Shimpalee et al. [76] have demonstrated that shorter channel lengths on the cathode side improve cell performance due to lower pressure drops and more uniform current density distribution and consequently better water removal within the channels. On the anode side, longer channels have been shown to improve cell performance while possessing larger pressure drops [49]. Overall, single serpentine flow fields have been shown to produce better performance when compared to parallel, grid, mixed or interdigitated flow fields in direct methanol fuel cells due to more efficient removal of water formed within the channel resulting from the higher pressure within the channel as well as more uniform distribution of the reactants [87].

From the results graphed in Figure 4.15, the effect of varying the number of passes shows higher performance for the plates with 11 passes compared to 9 passes. Even though the open channel area of the flow field with 9 passes is higher at 2.9 cm^2 than the flow field with 11 passes at 2.4 cm^2, the larger rib widths cause a non-uniform distribution of methanol in the diffusion layer, weakening methanol mass transfer and thereby causing degradation in cell performance. The higher ohmic losses of the plate with 9 passes can be attributed to the use of thicker Teflon gaskets which increase the internal resistance of the cell.

When the channel and rib widths are 1.75 mm and 0.555 mm, respectively, the performance of the plates with 10 passes is still poor when compared to the commercial plates with channel and rib widths of 1 mm and 0.5 mm, respectively. Research by others has shown that to obtain low contact resistance, adequate rib fraction about 50% of the channel width is needed. Therefore, the use of narrow ribs to improve performance also requires narrow channels to provide the sufficient rib fraction. Consequently, having channel widths larger than about 1.0 mm, especially at lower rib fractions, is undesirable as this causes an increase in high frequency resistance (HFR) [88]. This corresponds to the results observed in Figures 4.16 and 4.17 for the plot of the plates with the rectangular channel cross section.

The plates with the flow field of varying channel and rib widths were fabricated with the aim of constricting the fluid flow at the inlet side, thereby increasing the pressure drop in the channels and hence improving the uniformity of the reactant distribution across the flow field. Similar flow field designs have been reported in [89] and [90] where restrictions were artificially placed at the inlet and the exit of parallel flow channels to achieve higher pressure drops in PEMFCs. The performance of the laser sintered plates as shown in Figure 4.15 is better than the flow field with 9 uniform passes but not as good as the one with 11 uniform passes. Although the results show higher mass transfer losses than the commercial plates, the ability to manufacture such designs and rapidly test them highlights the ability of indirect LS as a useful tool for fuel cell design and testing.

5.5.2 COMPARING TRIANGULAR VERSUS RECTANGULAR CHANNEL CROSS SECTIONS

The influence of flow field channel cross section geometry on the performance of PEMFCs has been discussed in [75, 91] and [92] where the effect of channel shapes such as trapezoidal, triangular and hemispherical were analyzed using numerical techniques. Due to the cost and limitations with machining/milling of these flow field channels, experimental results have been lacking in these studies. The results reported in Chapter 4 provide a comparison of different cross sectional shapes with rectangular channels.

The polarization curves for the triangular and elliptical cross sections with channel and rib widths of 1.75 mm and 0.555 mm, respectively, shown in Figure 4.16 show performance that is similar to that of the commercial plates with a rectangular cross section, contrary to expectations. The improved performance may be attributed to the triangular and elliptical cross sectional shape of the channel when considering the degraded performance of the laser sintered plates with rectangular channels. The same performance comparison is observed (Figure 4.17) upon scaling up to 10 cm^2 channels, where the triangular/elliptical channels outperform the rectangular channels.

Reddy et al. [75] have reported increased hydrogen consumption at the anode in PEMFC simulations when using triangular channel bipolar plates. As seen in Figure 5.4, triangular and hemispherical channels have a much higher pressure drop than rectangular channels which increases with flow rate thereby performing better. In a DMFC, this performance improvement can be attributed to the oxygen kinetics at the cathode side.

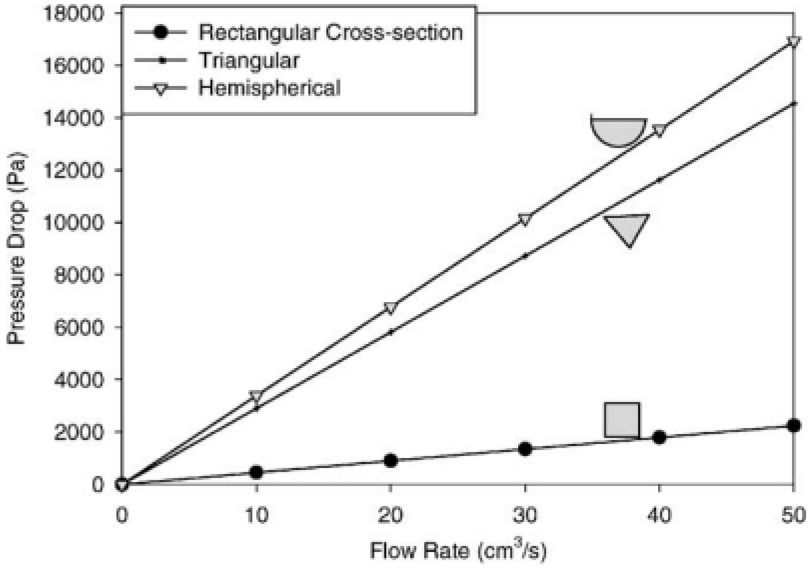

Figure 5.4 Effect of channel shape on the pressure drop in the channels [75].

When the number of channel passes is increased to 15 and the channel and rib widths are reduced to 1 mm and 0.5 mm, respectively, the performance of the triangular and elliptical channel plates at high current density is seen (Figure 4.18) to increase drastically. While the performance of the rectangular channel commercial and laser sintered plates are seen to be similar in performance at high current densities, there is a higher ohmic loss for the laser sintered plates that can be assigned to the increased internal resistance from using thicker Teflon gaskets.

The improvement in the mass transport characteristics of the triangular/elliptical channels was verified by doubling the methanol solution concentration and halving the flow rate (2M, 3 ml/min) while keeping the cathode oxygen flow rate constant. Figure 4.20b shows that the performance of the triangular channels replicates the superior mass transport behavior seen in Figure 4.20a with 1M methanol solution and 6 ml/min flow rate. This indicates that the gains in performance are not primarily due to improvements in the anode side kinetics. The results of the constant current discharge tests shown in Figure 4.21a-c confirm the performance improvement of the triangular channels.

It is well known that the design of the cathode flow field affects the air mass transfer and the drainage. If the water formed at the cathode is not removed at a sufficient rate, flooding may occur, and transport of oxygen to the catalyst sites is hindered [93]. Researchers have attributed cathode flooding as a primary determinant of overall PEMFC performance [94]. In DMFCs, the flooding water is producing by electrochemistry at the cathode and crossover from the anode [95, 96]. From Figure 4.22 which shows the results of reducing the cathode oxygen flow rate from 200 ml/min to 100 ml/min, it can be seen that the laser sintered triangular channel plates suffer from flooding and therefore produce an unsteady polarization curve while there is no change in the performance of the commercial rectangular channel plates.

Owejan et al. [97] have shown that triangular cross section channels retain less water than rectangular cross sectioned channels (Figure 5.5). In their comparison of the differences in slug shape observed in rectangular and triangular channel geometries, they show that as a result of the surface tension acting to force water to the corners encompassed by small angles, smaller water slugs were retained in triangular channels than in rectangular channels. Results published on the phase distributions in air-water flow through small triangular channels show that water tends to be transported in the corners with the air flowing in the high-velocity core [98].

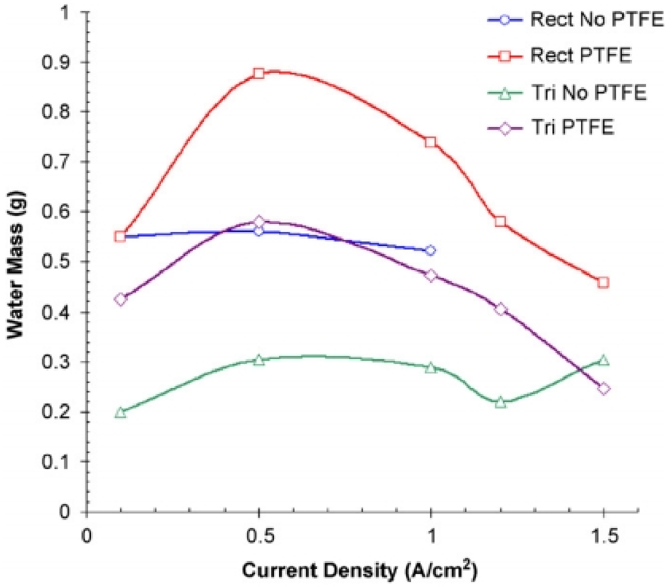

Figure 5.5 Measured water mass profiles for channel property study [97].

From Figure 5.6, it appears that in the rectangular case, large water slugs with many smaller droplets fill most of the channel cross-section and are affected by gravity, as many of these large slugs are retained at the lower channel edge. In the triangular channels, the slugs do not seem to be influenced by gravity to as great a degree, but are retained in the sidewalls adjacent to the GDL.

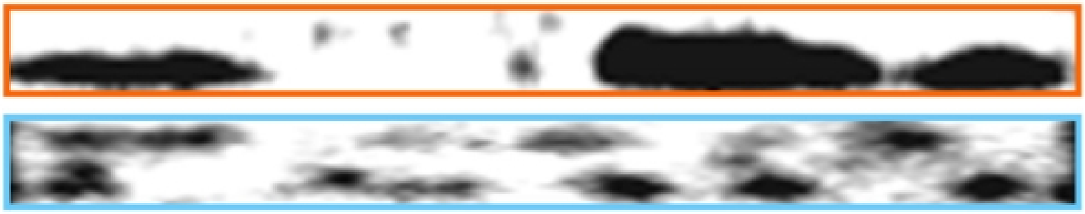

Figure 5.6 Enlarged view of slug formation in rectangular (top) and triangular (bottom) channels [97].

Figure 4.19 shows polarization curves obtained by running the cell with hydrogen during the break-in procedure of the MEA. The consistency in the performance of the laser sintered triangular channel plates is evident from these results as the difference between the curves for the rectangular and triangular channels mirror those obtained by running the cell with methanol. This performance with hydrogen as the fuel also indicates that leakage in the laser sintered plates is minimal and comparable to that in the commercially machined plates.

5.5.3 MANIFOLDED BIPOLAR PLATES

The manifolded plates built by laser sintering represent the distinct advantage of the 3D manufacturing process which is the capability to produce incredibly complex structures. The flow field design was inspired by research by Hsieh et al. [99] describe a novel flow field design that is similar to the laser sintered manifolded plate in that it possesses a single inlet and four outlets (Figure 5.7). Reportedly, the design improves water and CO_2 removal from the cell, consequently improving the overall performance of the DMFC. From the polarization curves plotted in Figure 4.23, it is apparent there is a considerable reduction in performance when compared to a 25 cm^2 single serpentine flow field. This is possibly due to a loss in pressure at the internal manifolding which requires higher inlet pressures to pump the reactants through the cell which is beyond the flow rates achievable with the peristaltic pump used for supplying the methanol solution to the anode. It is apparent that the performance of the manifolded plates improves as the anode flow rate is increased to 14 ml/min.

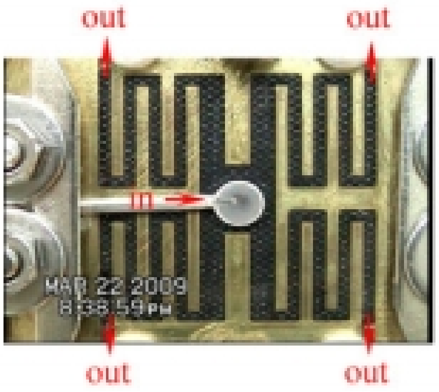

Figure 5.7 Novel flow field design with single inlet and four outlets [99].

5.6 DISTRIBUTION OF METHANOL TO THE CATALYST LAYER AS ASSESSED BY METHANOL CROSSOVER

Methanol crossover associated with the use of Nafion membranes poses two issues. First, oxidation of the methanol in the cathode side results in a mixed potential and consequently lowers cell efficiency. Second, loss of fuel through crossover reduces the fuel efficiency. Various studies have been conducted on the effects of anode flow field geometry on methanol and CO_2 transport in DMFCs [100, 101, 102]. In general, increasing methanol solution concentration contributes to an increase in the anode reactivity and generates high levels of methanol crossover which in turn tends to lower performance. Methanol crossover is first and foremost a membrane related phenomenon which is affected by flow field design in that improved fuel distribution to the diffusion media results in improved performance while consequently resulting in higher crossover.

The results of methanol crossover measured while testing the laser sintered bipolar plates show that with increasing performance there is a corresponding increase in the crossover current. Figures 4.24b–d represent the results for single cells operating with a 5 cm^2 MEA with 4 mg/cm^2 catalyst loading. Figure 4.24a shows the results for an MEA with 2.5 mg/cm^2 loading. Due to the lower catalyst loading, stabilization of the methanol diffusion takes longer and hence a steady crossover current is not measured. By comparison, the crossover current measured for the triangular channels is comparable to that of the commercial rectangular channel plates. It is seen that as the channel and rib size decrease, the performance of the triangular/elliptical plates increases as does the methanol crossover. Studies have shown that when the channel width decreases from 3 mm to 1 mm both through and in-plane mass transport of methanol was enhanced as a result of the faster gas bubble removal and increased under-rib convection in a SSFF, thereby leading to better cell performance [49].

It has also been reported that improving reactant distribution across the anode flow field improves performance at low methanol concentrations (~ 1 M). With an increase in concentration (~2 M), higher levels of methanol crossover are induced, decreasing cell performance [87]. Due to limitations in the measurement range of the galvanostat, crossover currents for higher methanol concentrations could not be measured. Though improvements in anode flow field design are capable of increasing DMFC performance while maintaining low level of methanol crossover, methanol crossover is a phenomenon which is highly associated with the electrolyte membrane used and will therefore benefit most from advances in membrane technologies.

Chapter 6. Conclusions and Future work

6.1 CONCLUSIONS

The process of indirect Laser Sintering (LS) offers flexibility for bipolar plate development and manufacturing. This additive process provides the ability to manufacture complex geometries that are otherwise difficult to obtain, among which are the complex flow fields on both sides of the bipolar plates. Graphite bipolar plates were successfully fabricated using indirect laser sintering and tested for performance in a fuel cell test station. Further, various flow field designs were fabricated and the effects of varying flow field channel dimensions were observed and compared to results observed in the literature. Based on the experimental results obtained in this research work, the following conclusions can be drawn:

1) An existing process for fabricating graphite bipolar plates using a mixture of 70 wt% graphite as the host material and 30 wt% of phenolic resin as the binder was modified to produce fully dense, electrically conductive parts that were tested in a fuel cell test station successfully.
2) The electrical conductivity of the LS graphite brown parts was found to be limited by the resistivity of the amorphous carbon residue produced during the pyrolysis of the phenolic resin binder. By increasing the heat treatment temperature to 1200 ºC, electrical conductivities of ~200 S/cm were obtained. XRD results of carbonized phenolic resins suggest semi-graphitization of the pyrolyzed carbon product which explains the increase in conductivity. This increase in conductivity resulted in a reduction of the contact resistance and

overall resistance of the DMFC, thus reducing ohmic losses and consequently improving cell performance.

3) To successfully produce a testable bipolar plate, full densification of the brown parts, measured to be approximately 50% porous, was critical. Infiltration experiments were carried out using different methods including electro-polymerization, electroless nickel deposition and gravity infiltration of low viscosity polymers, which yielded varying degrees of success. Full densification of the brown parts was achieved using low viscosity ethyl cyanoacrylate polymer that rendered the brown parts impermeable to fluids. Due to the insulating nature of the cured polymer, grinding of the external surfaces of the parts was required to restore the electrically conductive graphite matrix.
4) Due to the fragile nature of the green parts, fracture of parts during breakout from the build is foreseeable. Additives such as carbon fiber were mixed with the graphite and phenolic in order to improve handling strength as well as electrical conductivity. It was found that with increasing carbon fiber conrtent, while there was an increase in the flexural strength of the green parts, but the electrical conductivity decreased due to the reduction in interconnectivity of the graphite and carbon fiber matrix.
5) Bipolar plates made by laser sintering were tested in a DMFC test station using commercially purchased hardware and MEA. The results were compared with the performance of commercial POCO graphite machined plates. The plates made by LS produced consistent, repeatable results and in some cases outperformed the commercial plates.

6) It was found that an optimum channel width, rib width and channel depth exists at which performance of a given flow field is maximized. In the case of single serpentine flow fields with rectangular cross sections, the optimum channel and rib widths were around 1 mm and 1 mm, respectively. Varying the channel cross-section was also found to have a significant impact on the performance of the DMFC. LS bipolar plates with triangular and elliptical shaped channels with channel and rib widths of 1 mm and 0.5 mm, respectively, were found to consistently outperform commercial plates with equivalently sized rectangular machined channels.
7) Varying the flow rates of the anode and cathode reactants helped in understanding the reasons behind the performance improvements seen when using triangular/elliptical channel plates. By increasing the concentration of the methanol solution from 1 M to 2 M and halving the flow rate to 3 ml/min, it was seen that the performance difference between the triangular channel and rectangular channel plates was unchanged. Whereas, reducing the cathode flow rate from 200 ml/min to 100 ml/min increased the water flooding on the cathode side, reducing the performance of the LS triangular channel plates. This verified that, at sufficiently high cathode gas flow rates (~200 ml/min), triangular channels are more effective in the removal of water from within the cell.
8) The benefits of additive manufacturing were highlighted by the fabrication of bipolar plates with internal manifolding without any additional tooling. These plates would be impossible to build using conventional machining/molding techniques and therefore, though there were no performance gains from the

testing of these plates, the advantages of using indirect laser sintering as a tool for fuel cell designers was emphasized.

6.2 FUTURE WORK

This research work has conclusively shown a process to fabricate and test graphite bipolar plates by indirect laser sintering. Further, it was shown that improvements in the performance of a DMFC could be achieved by optimizing flow field channel dimensions and also varying the channel cross-section geometry. However, due to the limitations of the rapid prototyping machine (Sinterstation 2000) used in the experiments, build times are time consuming and therefore a build with 8 sets of plates takes over a day to complete. Improving the instrument technology can reduce build times by half and enable even quicker prototype testing.

Infiltration of the LS performs with cyanoacrylate has the drawback that excess cyanoacrylate can clog the flow field and other fine features and thereby degrade cell performance. Work is in progress to introduce more control in this process thereby preventing curing of the cyanoacrylate in unwanted regions. The process will also benefit from research into conductive infiltrants that can reduce contact resistance and ohmic losses.

Research at The University of Texas at Austin has developed innovative designs such as corrugated bipolar plates that increase the contact area between the flow field and the MEA with the aim of improving cell performance (Figure 6.1). Work is also underway in testing the effect of various additives such as wax and nylon on the green part strength.

Figure 6.1 Corrugated bipolar plates made by indirect laser sintering.

In conclusion, the contributions of the present work can be summarized as:

- The development of a process to create fuel cell bipolar plates that meet the DOE requirements of electrical conductivity, permeability and flexural strength.
- Identifying ways of improving DMFC performance by varying flow field channel dimensions and geometry.

Bibliography

[1] W. Vielstich, A. Lamm, and H. A. Gasteiger, *Handbook of Fuel Cells - Volume 1: Fundamentals Technology and Applications*. Wiley, 2003.

[2] L. G. Kemeny, “A review of the global environmental impact of fossil and nuclear fuels,” *Mathematics and Computers in Simulation*, vol. 24, no. 2-3, pp. 194-203, Apr. 1982.

[3] E. I. A. (US), *International Energy Outlook, 2006*. Energy Information Administration, 2006.

[4] EG&G Technical Services, Inc., *Fuel Cell Handbook (Seventh Edition)*. U.S. Department of Energy Office of Fossil Energy National Energy Technology Laboratory P.O. Box 880 Morgantown, West Virginia 26507-0880, 2004.

[5] D. L. Bourell, J. J. Beaman Jr, Leu, Ming C., and D. W. Rosen, “A Brief History of Additive Manufacturing and the 2009 Roadmap for AdditiveManufacturing: Looking Back and Looking Ahead,” in *Proceedings of Symposium on Rapid Prototyping of Materials*, 2002, pp. 3–17.

[6] A. Casalegno and R. Marchesi, “DMFC performance and methanol cross-over: Experimental analysis and model validation,” *Journal of Power Sources*, vol. 185, no. 1, pp. 318-330, Oct. 2008.

[7] H. Liu, C. Song, L. Zhang, J. Zhang, H. Wang, and D. P. Wilkinson, “A review of anode catalysis in the direct methanol fuel cell,” *Journal of Power Sources*, vol. 155, no. 2, pp. 95-110, Apr. 2006.

[8] H. Dohle, J. Divisek, J. Mergel, H. F. Oetjen, C. Zingler, and D. Stolten, “Recent developments of the measurement of the methanol permeation in a direct methanol fuel cell,” *Journal of Power Sources*, vol. 105, no. 2, pp. 274-282, Mar. 2002.

[9] I. Bar-On, R. Kirchain, and R. Roth, “Technical cost analysis for PEM fuel cells,” *Journal of power sources*, vol. 109, no. 1, pp. 71–75, 2002.

[10] A. S. Woodman, “Lightweight and corrosionresistant metal bipolar platesfor PEM fuel cells,” *Society of Automotive Engineers*, vol. 01-2614, pp. 1-8, 1999.

[11] D. Ma, F. Lin, and C.K. Chua, “Rapid Prototyping Applications in Medicine. Part 1: NURBS-Based Volume Modelling,” *The International Journal of Advanced Manufacturing Technology*, vol. 18, no. 2, pp. 103-117, 2001.

[12] S. Satyapal, "Overview of DOE Hydrogen and Fuel Cell Activities," 2010.

[13] W. M. Steen and J. Mazumder, *Laser Material Processing: Fourth Edition*. Springer-Verlag London Limited, 2010.

[14] K. G. Cooper, *Rapid prototyping technology: selection and application*. 2001.

[15] A. Mazzoli, G. Moriconi, and M. G. Pauri, "Characterization of an aluminum-filled polyamide powder for applications in selective laser sintering," *Materials & Design*, vol. 28, no. 3, pp. 993-1000, 2007.

[16] R. D. Goodridge, C. J. Tuck, and R. J. M. Hague, "Laser sintering of polyamides and other polymers," *Progress in Materials Science*, vol. In Press, Corrected Proof.

[17] R. D. Goodridge et al., "Processing of a Polyamide-12/carbon nanofibre composite by laser sintering," *Polymer Testing*, vol. 30, no. 1, pp. 94-100, Feb. 2011.

[18] B. Van Hooreweder, F. De Coninck, D. Moens, R. Boonen, and P. Sas, "Microstructural characterization of SLS-PA12 specimens under dynamic tension/compression excitation," *Polymer Testing*, vol. 29, no. 3, pp. 319-326, May. 2010.

[19] J. A. Manriquez-Frayre and D. L. Bourell, "Selective Laser Sintering of Cu-Pb/Sn Solder Powders," in *Solid Freeform Fabrication Symposium Proceedings*, The University of Texas at Austin, Austin, Texas, 1991, pp. 236-244.

[20] M. K. Agarwala, D. L. Bourell, B. Wu, and J. J. Beaman, "An Evaluation of the Mechanical Behavior of Bronze-Ni Composites Produced by Selective Laser Sintering," in *Solid Freeform Fabrication Symposium Proceedings*, The University of Texas at Austin, Austin, Texas, 1993, pp. 193- 203.

[21] M. K. Agarwala, D. L. Bourell, and J. J. Beaman, "Densification of Selective Laser Sintered Metal Parts by Hot Isostativ Pressing," in *Solid Freeform Fabrication Symposium Proceedings*, The University of Texas at Austin, Austin, Texas, 1994, pp. 65-73.

[22] S. Chen, "Fabrication of PEM Fuel Cell Bipolar Plate by Indirect Selective Laser Sintering," University of Texas at Austin, 2006.

[23] R. S. Evans, "Indirect Rapid Manufacturing of Silicon Carbide Composites," The University of Texas at Austin, 2005.

[24] J.-K. Kuo and C.-K. Chen, “A novel Nylon-6-S316L fiber compound material for injection molded PEM fuel cell bipolar plates,” *Journal of Power Sources*, vol. 162, no. 1, pp. 207-214, Nov. 2006.

[25] R. Hornung and G. Kappelt, “Bipolar plate materials development using Fe-based alloys for solid polymer fuel cells,” *Journal of Power Sources*, vol. 72, no. 1, pp. 20-21, Mar. 1998.

[26] A. Kumar and R. G. Reddy, “Materials and design development for bipolar/end plates in fuel cells,” *Journal of Power Sources*, vol. 129, no. 1, pp. 62-67, Apr. 2004.

[27] D. P. Davies, P. L. Adcock, M. Turpin, and S. J. Rowen, “Stainless steel as a bipolar plate material for solid polymer fuel cells,” *Journal of Power Sources*, vol. 86, no. 1-2, pp. 237-242, Mar. 2000.

[28] “Hydrogen, Fuel Cells & Infrastructure Technologies Program Multi-Year Research, Development and Demonstration Plan - Planned Program Activities for 2005-2015.” Department of Energy, 2009.

[29] P. L. Hentall, J. B. Lakeman, G. O. Mepsted, P. L. Adcock, and J. M. Moore, “New materials for polymer electrolyte membrane fuel cell current collectors,” *Journal of Power Sources*, vol. 80, no. 1-2, pp. 235-241, Jul. 1999.

[30] J. Barranco et al., “Cr and Zr/Cr nitride CAE-PVD coated aluminum bipolar plates for polymer electrolyte membrane fuel cells,” *International Journal of Hydrogen Energy*, vol. 35, no. 20, pp. 11489-11498, Oct. 2010.

[31] L. Guo, D. Zhang, L. Duan, Z. Wang, and W.-H. Tuan, “Formation of nano-contacts on Fe-Ni-Cr alloy for bipolar plate of proton exchange membrane fuel cell,” *International Journal of Hydrogen Energy*, vol. 36, no. 11, pp. 6832-6839, Jun. 2011.

[32] S.-H. Wang, J. Peng, W.-B. Lui, and J.-S. Zhang, “Performance of the gold-plated titanium bipolar plates for the light weight PEM fuel cells,” *Journal of Power Sources*, vol. 162, no. 1, pp. 486-491, Nov. 2006.

[33] H. Wang and J. A. Turner, “Ferritic stainless steels as bipolar plate material for polymer electrolyte membrane fuel cells,” *Journal of Power Sources*, vol. 128, no. 2, pp. 193-200, Apr. 2004.

[34] S.-J. Lee, C.-H. Huang, J.-J. Lai, and Y.-P. Chen, “Corrosion-resistant component for PEM fuel cells,” *Journal of Power Sources*, vol. 131, no. 1-2, pp. 162-168, May. 2004.

[35] S. A. A. El-Enin, O. E. Abdel-Salam, H. El-Abd, and A. M. Amin, “New electroplated aluminum bipolar plate for PEM fuel cell,” *Journal of Power Sources*, vol. 177, no. 1, pp. 131-136, Feb. 2008.

[36] J. Scholta, B. Rohland, V. Trapp, and U. Focken, “Investigations on novel low-cost graphite composite bipolar plates,” *Journal of Power Sources*, vol. 84, no. 2, pp. 231-234, Dec. 1999.

[37] V. Mehta and J. S. Cooper, “Review and analysis of PEM fuel cell design and manufacturing,” *Journal of Power Sources*, vol. 114, no. 1, pp. 32–53, 2003.

[38] R. Meissner, M. Irgang, K. Eger, P. Weidlich, and H. Dreyer, “Graphite moldings,” U.S. Patent 573607607-Apr-1998.

[39] M. S. Wilson and D. N. Busick, “Composite bipolar plate for electrochemical cells,” U.S. Patent 6248467.

[40] A. Heinzel, F. Mahlendorf, O. Niemzig, and C. Kreuz, “Injection moulded low cost bipolar plates for PEM fuel cells,” *Journal of Power Sources*, vol. 131, no. 1-2, pp. 35-40, May. 2004.

[41] J. Banhart, “Manufacture, characterisation and application of cellular metals and metal foams,” *Progress in Materials Science*, vol. 46, no. 6, pp. 559-632, 2001.

[42] J. Scholta, N. Berg, P. Wilde, L. Jörissen, and J. Garche, “Development and performance of a 10kW PEMFC stack,” *Journal of Power Sources*, vol. 127, no. 1-2, pp. 206-212, Mar. 2004.

[43] “About Fuel Cells - New & Renewable Energy Systems Group - TKK AES.” [Online]. Available: http://www.tkk.fi/Units/AES/projects/renew/fuelcell/fc_4.html. [Accessed: 06-Jul-2011].

[44] C. S. Spiegel, *Designing and Building Fuel Cells*, 1st ed. McGraw Hill, 2007.

[45] E. Hontaňon, M. J. Escudero, C. Bautista, P. L. Garcia-Ybarra, and L. Daza, “Optimisation of flow-field in polymer electrolyte membrane fuel cells using computational fluid dynamics techniques,” *Journal of Power Sources*, vol. 86, no. 1-2, pp. 363-368, Mar. 2000.

[46] Y.-G. Yoon, W.-Y. Lee, G.-G. Park, T.-H. Yang, and C.-S. Kim, “Effects of channel and rib widths of flow field plates on the performance of a PEMFC,” *International Journal of Hydrogen Energy*, vol. 30, no. 12, pp. 1363-1366, Sep. 2005.

[47] J. Scholta, G. Escher, W. Zhang, L. Küppers, L. Jörissen, and W. Lehnert, “Investigation on the influence of channel geometries on PEMFC performance,” *Journal of Power Sources*, vol. 155, no. 1, pp. 66-71, Apr. 2006.

[48] G. Catlin, S. G. Advani, and A. K. Prasad, “Optimization of PEMFC flow channels using a genetic algorithm,” *Journal of Power Sources*, vol. In Press, Accepted Manuscript.

[49] H. Yang and T. S. Zhao, “Effect of anode flow field design on the performance of liquid feed direct methanol fuel cells,” *Electrochimica Acta*, vol. 50, no. 16-17, pp. 3243-3252, May. 2005.

[50] C. W. Wong, T. S. Zhao, Q. Ye, and J. G. Liu, “Experimental investigations of the anode flow field of a micro direct methanol fuel cell,” *Journal of Power Sources*, vol. 155, no. 2, pp. 291-296, Apr. 2006.

[51] S. Chen, J. Murphy, J. Herlehy, D. L. Bourell, and K. L. Wood, “Development of SLS fuel cell current collectors,” *Rapid Prototyping Journal*, vol. 12, no. 5, pp. 275-282, 2006.

[52] L. M. Manocha, H. Bhatt, and S. M. Manocha, “Development of carbon/carbon composites by co-carbonization of phenolic resin and oxidised pan fibers,” *Carbon*, vol. 34, no. 7, pp. 841–849, 1996.

[53] Z. Laušević and S. Marinković, “Mechanical properties and chemistry of carbonization of Phenol formaldehyde resin,” *Carbon*, vol. 24, no. 5, pp. 575-580, 1986.

[54] C. R. Choe, K. H. Lee, and B. Il Yoon, “Effect of processing parameters on the mechanical properties of carbonized phenolic resin,” *Carbon*, vol. 30, no. 2, pp. 247-249, 1992.

[55] “Pycnometer Principles, Operating Manual, Quantachrome Ultrapycnometer 1000.” Quantachrome Corporation, 1996.

[56] T. Young, “An essay on the cohesion of fluids,” *Phil. Trans R. Soc.*, vol. 95, pp. 65-87, 1805.

[57] M. Palaniappa, G. V. Babu, and K. Balasubramanian, “Electroless nickel-phosphorus plating on graphite powder,” *Materials Science and Engineering: A*, vol. 471, no. 1-2, pp. 165-168, Dec. 2007.

[58] S. E. Bourdo and T. Viswanathan, "Graphite/Polyaniline (GP) composites: Synthesis and characterization," *Carbon*, vol. 43, no. 14, pp. 2983-2988, Nov. 2005.

[59] X. S. Du, M. Xiao, and Y. Z. Meng, "Facile synthesis of highly conductive polyaniline/graphite nanocomposites," *European Polymer Journal*, vol. 40, no. 7, pp. 1489-1493, Jul. 2004.

[60] A. Pron et al., "Metallic polyaniline processed from 1,1,1,3,3,3-hexafluoro-2-propanol," *Synthetic Metals*, vol. 101, no. 1-3, pp. 729-730, May. 1999.

[61] S. Joseph, J. C. McClure, R. Chianelli, P. Pich, and P. J. Sebastian, "Conducting polymer-coated stainless steel bipolar plates for proton exchange membrane fuel cells (PEMFC)," *International Journal of Hydrogen Energy*, vol. 30, no. 12, pp. 1339-1344, Sep. 2005.

[62] E. M. Petrie, *Handbook of Adhesives and Sealants*. McGraw Hill, 2000.

[63] A. Kraytsberg, M. Auinat, and Y. Ein-Eli, "Reduced contact resistance of PEM fuel cell's bipolar plates via surface texturing," *Journal of Power Sources*, vol. 164, no. 2, pp. 697-703, Feb. 2007.

[64] B. Avasarala and P. Haldar, "Effect of surface roughness of composite bipolar plates on the contact resistance of a proton exchange membrane fuel cell," *Journal of Power Sources*, vol. 188, no. 1, pp. 225-229, Mar. 2009.

[65] "ASTM C611 Standard Test Method for Electrical Resistivity of Manufactured Carbon and Graphite Articles at Room Temperature." ASTM.

[66] W. Lee, C. H. Ho, J. W. Van Zee, and M. Murthy, "The effects of compression and gas diffusion layers on the performance of a PEM fuel cell," *Journal of power sources*, vol. 84, no. 1, pp. 45–51, 1999.

[67] H. Dohle, J. Mergel, and D. Stolten, "Heat and power management of a direct-methanol-fuel-cell (DMFC) system," *Journal of Power Sources*, vol. 111, no. 2, pp. 268–282, 2002.

[68] P. S. Kauranen, E. Skou, and J. Munk, "Kinetics of methanol oxidation on carbon-supported Pt and Pt+ Ru catalysts," *Journal of Electroanalytical Chemistry*, vol. 404, no. 1, pp. 1–13, 1996.

[69] X. Ren, W. Henderson, and S. Gottesfeld, "Electro-osmotic Drag of Water in Ionomeric Membranes," *J. Electrochem. Soc.*, vol. 144, p. L267, 1997.

[70] K. Alayavalli and D. L. Bourell, “Fabrication of modified graphite bipolar plates by indirect selective laser sintering (SLS)for direct methanol fuel cells,” *Rapid Prototyping Journal*, vol. 16, no. 4, pp. 268-274, 2010.

[71] N. Guo and M. C. Leu, “Effect of Different Graphite Materials on the Electrical Conductivity and Flexural Strength of Bipolar Plates Fabricated by Selective Laser Sintering,” presented at the SFF Symposium, Austin, TX, 2010, pp. 482-492.

[72] *Engineered Materials Handbook, Engineering Plasctics*, vol. 2. Materials Park, OH: ASM International.

[73] D. L. Bourell, M. C. Leu, K. Chakravarthy, N. Guo, and K. Alayavalli, “Graphite-based indirect laser sintered fuel cell bipolar plates containing carbon fiber additions,” *CIRP Annals-Manufacturing Technology*, 2011.

[74] W. Li, Y. Z. Fu, A. Manthiram, and M. D. Guiver, “Blend Membranes Consisting of Sulfonated Poly(ether ether ketone) and Polysulfone Bearing 4-Nitrobenzimidazole for Direct Methanol Fuel Cells,” *J. Electrochem. Soc.*, vol. 156, p. B258, 2009.

[75] A. Kumar and R. G. Reddy, “Effect of channel dimensions and shape in the flow-field distributor on the performance of polymer electrolyte membrane fuel cells,” *Journal of Power Sources*, vol. 113, no. 1, pp. 11–18, 2003.

[76] S. Shimpalee, S. Greenway, and J. W. Van Zee, “The impact of channel path length on PEMFC flow-field design,” *Journal of power sources*, vol. 160, no. 1, pp. 398–406, 2006.

[77] A. BIyIkoglu, “Review of proton exchange membrane fuel cell models,” *International Journal of Hydrogen Energy*, vol. 30, no. 11, pp. 1181-1212, Sep. 2005.

[78] X. Ren, T. E. Springer, and S. Gottesfeld, “Water and Methanol Uptakes in Nafion Membranes and Membrane Effects on Direct Methanol Cell Performance,” *J. Electrochem. Soc.*, vol. 147, p. 92, 2000.

[79] R. A. Antunes, M. C. L. Oliveira, G. Ett, and V. Ett, “Corrosion of metal bipolar plates for PEM fuel cells: A review,” *International Journal of Hydrogen Energy*, vol. 35, no. 8, pp. 3632-3647, Apr. 2010.

[80] J. Wind, R. Späh, W. Kaiser, and G. Böhm, “Metallic bipolar plates for PEM fuel cells,” *Journal of Power Sources*, vol. 105, no. 2, pp. 256-260, Mar. 2002.

[81] *Hydrogen, Fuel Cells & Infrastructure Technologies Program Multi-Year Research, Development and Demonstration Plan - Planned Program Activities for 2005-2015*. DoE Technical Report.

[82] J. C. Y. Koh and A. Fortini, "Prediction of thermal conductivity and electrical resistivity of porous metallic materials," *International Journal of Heat and Mass Transfer*, vol. 16, no. 11, pp. 2013-2022, Nov. 1973.

[83] G. Bhatia, R. K. Aggarwal, M. Malik, and O. P. Bahl, "Conversion of phenol formaldehyde resin to glass-like carbon," *Journal of materials science*, vol. 19, no. 3, pp. 1022–1028, 1984.

[84] S.-S. Tzeng and Y.-G. Chr, "Evolution of microstructure and properties of phenolic resin-based carbon/carbon composites during pyrolysis," *Materials Chemistry and Physics*, vol. 73, no. 2-3, pp. 162-169, Jan. 2002.

[85] *Edupack Software*. Granta Design, Ltd., 2010.

[86] R. M. German, *Powder metallurgy and particulate materials processing*. Princeton, NJ: MPIF, 2005.

[87] V. B. Oliveira, C. M. Rangel, and A. M. F. R. Pinto, "Effect of anode and cathode flow field design on the performance of a direct methanol fuel cell," *Chemical Engineering Journal*, vol. 157, no. 1, pp. 174-180, Feb. 2010.

[88] S. G. Goebel, "Impact of land width and channel span on fuel cell performance," *Journal of Power Sources*, vol. 196, no. 18, pp. 7550-7554, Sep. 2011.

[89] M. Johnson, D. Wilkinson, J. Kenna, O. Vanderleeden, J. Zimmerman, and M. Tabatabaian, "Differential pressure fluid flow fields for fuel cells," U.S. Patent 6586128.

[90] X. Li and I. Sabir, "Review of bipolar plates in PEM fuel cells: Flow-field designs," *International journal of hydrogen energy*, vol. 30, no. 4, pp. 359–371, 2005.

[91] D. H. Ahmed and H. J. Sung, "Effects of channel geometrical configuration and shoulder width on PEMFC performance at high current density," *Journal of Power Sources*, vol. 162, no. 1, pp. 327-339, Nov. 2006.

[92] J. E. Steinbrenner, E. S. Lee, C. H. Hidrovo, J. K. Eaton, and K. E. Goodson, "Impact of channel geometry on two-phase flow in fuel cell microchannels," *Journal of Power Sources*, 2011.

[93] J. J. Baschuk and X. Li, “Modelling of polymer electrolyte membrane fuel cells with variable degrees of water flooding,” *Journal of Power Sources*, vol. 86, no. 1-2, pp. 181-196, Mar. 2000.

[94] F.-B. Weng, A. Su, C.-Y. Hsu, and C.-Y. Lee, “Study of water-flooding behaviour in cathode channel of a transparent proton-exchange membrane fuel cell,” *Journal of Power Sources*, vol. 157, no. 2, pp. 674-680, Jul. 2006.

[95] M. M. Mench and C. Y. Wang, “An In Situ Method for Determination of Current Distribution in PEM Fuel Cells Applied to a Direct Methanol Fuel Cell,” *J. Electrochem. Soc.*, vol. 150, no. 79, 2003.

[96] X. Ren and J. Gottesfeld, “Electro-osmotic Drag of Water in Poly(perfluorosulfonic acid) Membranes,” *J. Electrochem. Soc.*, vol. 148, p. A87, 2001.

[97] J. P. Owejan, T. A. Trabold, D. L. Jacobson, M. Arif, and S. G. Kandlikar, “Effects of flow field and diffusion layer properties on water accumulation in a PEM fuel cell,” *International Journal of Hydrogen Energy*, vol. 32, no. 17, pp. 4489-4502, Dec. 2007.

[98] T. S. Zhao and Q. C. Bi, “Co-current air-water two-phase flow patterns in vertical triangular microchannels,” *International Journal of Multiphase Flow*, vol. 27, no. 5, pp. 765-782, May. 2001.

[99] S. S. Hsieh, H. C. Wu, and B. S. Her, “A novel design for a flow field configuration, of a direct methanol fuel cell,” *Journal of Power Sources*, vol. 195, no. 10, pp. 3224–3230, 2010.

[100] W. M. Yang, S. K. Chou, and C. Shu, “Effect of current-collector structure on performance of passive micro direct methanol fuel cell,” *Journal of Power Sources*, vol. 164, no. 2, pp. 549-554, Feb. 2007.

[101] B. Gurau and E. S. Smotkin, “Methanol crossover in direct methanol fuel cells: a link between power and energy density,” *Journal of Power Sources*, vol. 112, no. 2, pp. 339-352, Nov. 2002.

[102] C. Xu, Y. L. He, T. S. Zhao, R. Chen, and Q. Ye, “Analysis of Mass Transport of Methanol at the Anode of aDirect Methanol Fuel Cell,” *Journal of The Electrochemical Society*, vol. 153, no. 7, p. A1358-A1364, 2006.

Vita

Kaushik Alayavalli was born in Mysore, India in 1978 to Ravi Alayavalli and Revathi Ravi. He graduated in 2001 from the National Institute of Engineering, Mysore, with a Bachelors degree in Mechanical Engineering. After earning a Masters in Computer Aided Engineering Design in 2004 from the University of Strathclyde, he joined the University of Texas at Austin in 2005 to pursue a Ph.D. in Materials Science and Engineering. While pursuing his Ph.D. he also worked as a Teaching Assistant for both the undergraduate Materials Engineering Lab and the graduate SEM Lab courses.

Permanent Address: 5214, Joe Sayer's Avenue, Apt 1, Austin, Texas 78756

This dissertation was typed by the author